UNIVERSIDADE DO PORTO

FACULDADE DE ENGENHARIA

Master's Thesis

Prediction of free edge delamination in inspection holes of a composite wing-box for civil transport aircraft via global-local analysis

Pedro Ferreira

Supervisor: Volnei Tita, PhD.

Co-Supervisor: Federico Danzi, PhD.

Thesis submitted to Universidade do Porto – Faculdade de Engenharia
in partial fulfillment of the requirements for the degree of
Master in Mechanical Engineering - Aeronautical and Vehicles Structures

MEM

U.PORTO
FEUP FACULDADE DE ENGENHARIA
UNIVERSIDADE DO PORTO

DEPARTAMENTO DE ENGENHARIA MECÂNICA
Faculdade de Engenharia

October, 2023

Candidate: Pedro Ferreira, No. 201806093, `up201806093@up.pt`

Scientific Guidance: Volnei Tita, `voltita@sc.usp.br`

Scientific Co-Guidance: Federico Danzi, `fdanzi@inegi.up.pt`

U.PORTO
FEUP FACULDADE DE ENGENHARIA
UNIVERSIDADE DO PORTO
Departamento de Engenharia Mecânica
Faculdade de Engenharia
Rua Dr. Roberto Frias, Porto

October, 2023

"Learn from yesterday, live for today, hope for tomorrow.
The important thing is not to stop questioning."

Albert Einstein

Acknowledgements

Five years ago, I began the most demanding and at the same time fulfilling personal endeavour of my life. It is a pleasure to be graduating as mechanical engineer from the Faculty o Engineering of the University of Porto. During the past years I had an incredible time, met incredible people, incredible friends and also incredible professors. The culmination of this journey is not only due to my hard work but also to the one support and help provided by many people that without a doubt played an important role in my success.

Starting with Professor Volnei Tita and Professor Federico Danzi I would like to express my deepest thanks for introducing me to the amazing world of aeronautical structures, by providing valuable insights either during the classes or the development of the present work. The knowledge, experience, and steady confidence that demonstrated by them in my abilities have played a significant role in shaping my academic path with the culmination in this thesis. Their support and motivation throughout this quest have been incredibly valuable, and I feel privileged to have worked alongside such esteemed scholars.

I would also like to extend my gratitude to all the professors that cross my journey as an engineer, they sure did their fair part in transmitting knowledge and unravelling the curiosity and passion to pursue the mechanical engineer career. I cannot forget all my friends that were always present for the good and tough moments, from the crazy parties to the countless intensive study sessions that will forever live in my memory.

Last but no least, I extended the deepest of gratitudes to my beloved mum Ana, father Paulo and sister Margarida. These are the individuals that every single day stand by my side and push me to be better. Even though this thesis was outside their scope of knowledge they were the most important source of support I had.

Abstract

Composite structures are increasingly becoming more important in the construction of aeronautical and aerospace structures. However designing and studying the behaviour of such structures for aircraft applications is not a trivial task. The introduction of composite structures affects directly the design and certification processes of aircrafts, and implies testing many coupons and sub-assemblies which are very time demanding and expensive tasks. Thus, the development of computational tools that output reliable results are an important step towards optimizing the design capabilities of composites as well as the certification process, ultimately paving way to virtual certification procedures.

The highly anisotropic nature of composites has presented as a serial difficulty in developing analytical methods to characterize mechanical properties and behaviour of these materials. There are analytical tools available within the literature, that allow to characterize a composite to certain extent, but they don't come without their flaws. So engineers started developing numerical tools that could more easily implemented, maintaining reliability at the same time. Currently, the most acknowledge and established numerical tool within the aeronautical industry is the Finite Element Method (FEM). The problem with the application of this method to composite aircraft structures is that they tend to be of complex geometry and also present nonlinear behaviour which translates to difficult modelling and expensive computational costs. This issue, may be tackle in different ways, such as adaptative mesh refinement, shell-to-solid coupling, use of reduced integration elements, etc.

The current document focused on a one-way global-local analysis in a shell-to-solid configuration to predict delamination in laminated composite materials. Two different cases were analysed, one being an open-hole tensile test of laminated composite specimen and the other an wing-box structure. The results from the presented work show the that global-local finite element approaches are a powerful tool in modelling complex structures with evident computational cost reductions. As for delamination initiation and propagation it was seen that it is possible within this modelling approach, but the accuracy of the results is highly limited by the damage models, either intra or interlaminar, for composite laminates.

Keywords: Global-Local; Delamination; Composite materials; Damage; Aircraft structures.

Contents

List of Figures vii

List of Tables xi

List of Acronyms xiii

I Introduction 1

1 Introduction 3
- 1.1 Problem Statement 3
- 1.2 Background 3
- 1.3 Objectives 4
- 1.4 Thesis Layout 5

II State of the art and literature review 7

2 State of the Art 9
- 2.1 Composite Structures in Aircraft 9
- 2.2 Aircraft Materials Certification 11
  - 2.2.1 Aircraft design approach 11
  - 2.2.2 Regulations 13
- 2.3 Composite Failure Mechanisms 16
  - 2.3.1 Fibre Failure 17
  - 2.3.2 Matrix Failure 18
  - 2.3.3 Delamination 21
  - 2.3.4 Interface elements 24
- 2.4 Global-Local FEM 25
  - 2.4.1 Submodeling in Abaqus 26
    - Shell-to-solid submodeling 27
  - 2.4.2 Applications of global-local technique in the literature 28

III Numerical Finite Element Model 31

3 Cohesive Zone Model 33

Maximum and Quadratic Nominal Stress Criteria 37
Maximum and Quadratic Nominal Strain Criteria 38

4 Open-hole tensile test model 43
4.1 Scope of the model 43
4.2 Specimen Configuration 43
4.2.1 Material Properties 44

5 OHT reference model 47
5.1 Open-Hole Tension (OHT) with Hashin Damage Model 47
5.1.1 Geometry and Material definition 47
5.1.2 Boundary Conditions 48
5.1.3 Load 49
5.1.4 Mesh 49
5.1.5 Step 50
5.1.6 Results 51
5.2 OHT with Intra and Interlaminar damage via VUMAT 57
5.2.1 Interlaminar damage model 57
5.2.2 Geometry and material definition 58
5.2.3 Boundary Conditions 59
5.2.4 Load 59
5.2.5 Mesh 59
5.2.6 Step 59
5.2.7 Results 60

6 OHT global-Local model 65
6.1 Global Model 65
6.1.1 Results 66
6.2 Local model 66
6.2.1 Results 67
Hashin model 67
VUMAT model 69

IV Wing-Box Finite Element Model 71

7 Global Model 73
7.1 Generation of the model 73
7.1.1 Model description 73
7.1.2 CAD model and Mesh 75
7.1.3 Materials 76
7.1.4 Boundary Conditions 77

7.1.5 Loads 78
7.2 Simulation setup 81
7.3 Results 82

8 Local Model **85**
8.1 Generation of the model 85
8.1.1 CAD model and Mesh 85
8.1.2 Materials 88
8.1.3 Boundary Conditions 88
8.2 Simulation setup 89
8.3 Results 89
8.4 Other models 90
8.5 Curved thin shells 91

V Conclusions and Future Work **93**

9 Conclusions and Future Work **95**
9.1 Conclusion 95
9.2 Future Work 97

Appendix A Wing-Box Global Model Results **109**
A.1 Displacement Field, U 109

List of Figures

2.1 Amount of composite materials used in aircraft [3]. 10
2.2 Frequency of failure mechanisms [15], data retrieved from Findlay and Harison [18]; Gorelik [19]. 12
2.3 Fatigue design philosophies [15], adapted from Boller and Buderath[22]. . . 13
2.4 Building block approach for certification of aircraft materials and structures [3]. 14
2.5 Types of damage in laminated composites [36]. 16
2.6 Delamination sources [54]. 23
2.7 Fractures modes [54]. 23
2.8 Criteria for Mode-I and Mode-II delamination [54]. 23
2.9 Centre zone definition for shell-to-solid submodeling. [78]. 27
2.10 Typical two-way loose coupling procedure [72]. 28

3.1 Cohesive zone model of a damaged fibre-reinforced polymer. 34
3.2 Quasi-brittle bar with a cohesive interface. 35
3.3 Tri-linear cohesive law obtained by combining two bilinear laws [36]. 36
3.4 Graphical representation of a three-dimensional cohesive element [78]. . . 36
3.5 Traction separation response [78]. 37
3.6 Illustration of mixed-mode response in cohesive elements [78]. 39

4.1 Open-hole specimen dimensions 44

5.1 Open-hole reference model boundary conditions. 48
5.2 Open-hole reference model interaction and prescribed displacement. 49
5.3 Open-hole reference model mesh. 50
5.4 Energies for the open-hole reference model with Hashin damage. 51
5.5 Typical load-displacement curve for specimens failing by delamination [91]. 52
5.6 Stress-Strain curve for Open-Hole Tension (OHT) with Hashin damage. . . . 53
5.7 Stiffness degradation of the cohesive interfaces for the open-hole with Hashin damage model 54
5.8 Out-of-plane stresses for the interface 45°/90° at the assumed point of failure. 55
5.9 Out-of-plane stresses for the interface $90°/-45°$ at the assumed point of failure. 56

5.10 Out-of-plane stresses for the interface $-45^\circ/0^\circ$ at the assumed point of failure. 57
5.11 Open-hole reference model with VUMAT mesh. 59
5.12 Energies for the open-hole reference models with VUMAT. 60
5.13 Stress-Strain curves for full 3D OHT model with intra and interlaminar damage VUMAT. 61
5.14 Stiffness degradation of the cohesive interfaces for the open-hole with VUMAT and element deletion activated. 62
5.15 Stiffness degradation of the cohesive interfaces for the open-hole with VUMAT and NLGEOM on. 63
5.16 Typical delamination and splitting progress from FEM [99]. 63
5.17 Delamination evolution for the OHT with VUMAT and NLGEOM. 64

6.1 Open-hole global model mesh. 65
6.2 Open-hole global model displacement field in [mm], scale factor of 1. 66
6.3 Open-hole local model geometry. 67
6.4 Open-hole local model mesh. 67
6.5 Open-hole local model boundary conditions 67
6.6 Open-hole global-local model displacement magnitude overlay plot, [mm]. 68
6.7 Stiffness degradation of the cohesive interfaces for the open-hole local model with Hashin damage. 68
6.8 Open-hole global model displacement in coherence with the local model, [mm]. 69
6.9 Open-hole local VUMAT model displacement before abortion, [mm]. 69
6.10 Stiffness degradation of the cohesive interfaces for the open-hole local model with VUMAT. 70

7.1 Wingbox planform dimensions [mm]. 73
7.2 Spars geometry [mm]. 74
7.3 Ribs geometry [mm]. 74
7.4 Flanges geometry. 75
7.5 Wing-box CAD model coloured by material definition –red for composite, green for Al 2024-T3, and white for Al7475-T6. 76
7.6 Win-box lower skin with the inspection hole. 76
7.7 Wing-box mesh 77
7.8 Beam approximation. 77
7.9 Beam approximation equivalent boundary conditions. 78
7.10 Wing-box boundary conditions. 78
7.11 Wing regions for loads estimation. 80
7.12 Wing tip loads. 81
7.13 Wing-box FEM model with applied loads and boundary conditions. 82

7.14 Smooth amplitude curve. 82
7.15 Wing-box displacement magnitude [mm], scale factor of 1. 83

8.1 Schematic of the wing-box chunk to be used as a local part. 86
8.2 Sketch approach for the wing-box local part loft sections. 86
8.3 Second bay lower skin obtained from the lofts. The zoomed pictures highlight the different plies and in-between cohesive layers. 87
8.4 Wing-box local part final geometry. 87
8.5 Wing-box local part mesh. 87
8.6 Wing-box local model cohesive buffer zone. 88
8.7 Wing-box local model boundary conditions. 89
8.8 Wing-box displacement overlay plot with the global model and local model displacement , [mm]. 89
8.9 Wing-box local model most critical ply results, interface 0°/45°. 90
8.10 Wing-box local model with inter and intralaminar damage model via UMAT displacement field. 91

A.1 Wing-box displacement magnitude in [mm], scale factor of 1. 110
A.2 Wing-box displacement in the x direction in [mm], scale factor of 1. 111
A.3 Wing-box displacement in the y direction in [mm], scale factor of 1. 112
A.4 Wing-box displacement in the z direction in [mm], scale factor of 1. 113

List of Tables

2.1 Summary of regulations evolution history. 15
2.2 Failure criteria for fibres under tension [39]. 17
2.3 Failure criteria for fibres under compression [39]. 18
2.4 Failure criteria for fibres under tension and compression [39]. 18
2.5 Matrix failure under tension criteria [39]. 19
2.6 Matrix failure under compression criteria [39]. 20
2.7 Failure criteria for matrix in tension and compression [39]. 21
2.8 Failure criteria for delamination initiation [39]. 24
2.9 Failure criteria for delamination propagation [39]. 24

3.1 Damage Evolution in Abaqus [78]. 40
3.2 Parameter definition for Damage Evolution [78]. 41

4.1 Failure stresses [MPa], (variation, %), for open hole tension of $[45_m/90_m/-45_m/0_m]_{ns}$ laminates failed by delamination [91]. 44
4.2 IM7/8552 properties [92]. 45
4.3 Cohesive properties. 45

5.1 Simulation times for the open-hole model with the VUMAT. 60

7.2 Al 2024-T3 properties. 76
7.1 IM7/8552 properties [100]. 77
7.3 Al 7475-T6 properties. 77
7.4 Critical gust load case. 79
7.5 Shear force values. 80
7.6 Resulting bending moments acting on the wing tip. 81

8.1 Bay 2 vertices and arc radius [mm]. 85
8.2 Local part mesh element sizes. 88
8.3 Cohesive properties for the wing-box local model. 88

List of Acronyms

AC	Advisory Circular
ASTM	American Society for Testing and Materials
CAR	Civil Aeronautic Regulation
CFRP	Carbon Fibre Reinforced Polymer
CZM	Cohesive Zone Model
DCB	Double Cantilver Beam
EASA	European Union Aviation Safety Agency
ENF	End Notch Flexure
FAA	Federal Aviation Administration
FEM	Finite Element Method
FPF	First Ply Failure
FPZ	Fracture Process Zone
GFRP	Glass Fibre Reinforced Polymer
JAR	Joint Airworthiness Requirements
LPF	Last Ply Failure
MMB	Mixed Mode Beding
OHT	Open-Hole Tension
PMC	Polymer Matrix Composite
SLB	Single Leg Beding
VCCT	Virtual Crack Closure Technique

Part I

Introduction

Chapter 1

Introduction

1.1 Problem Statement

Composite materials may be briefly described as a combination of different materials that when put together, instead of compromising each other's quality or integrity, enhance one another providing structural advantages improving durability and performance of aircrafts.

Composite structures are increasingly becoming more important in the construction of aeronautical and aerospace structures. However designing and studying the behaviour of such structures for aircraft applications is not a trivial task. Unlike the conventional isotropic materials widely used in the past for aircraft construction, composite materials are in general anisotropic, meaning that its properties vary with the direction.

The introduction of composite structures affects directly the design and certification processes of aircrafts, and implies testing many coupons and sub-assemblies which are very time demanding and expensive tasks. Thus, the development of computational tools that output reliable results are an important step towards optimizing the design capabilities of composites as well as the certification process, ultimately paving the way to virtual certification procedures.

1.2 Background

The use of composites materials, especially carbon fibre reinforced ones, has been changing the paradigm of aircraft construction since the 20th century. Nonetheless, research is still being conducted to this day to better characterize these class of materials, that was the first to pose as feasible replacement for the well established aluminium alloys.

The highly anisotropic nature of composites has presented as a serial difficulty in developing analytical methods to characterize mechanical properties and behaviour of these materials. There are analytical tools available within the literature, that allow to characterize a composite to certain extent, but they don't come without their flaws. So engineers started developing numerical tools that could be more easily implemented, maintaining reliability at the same time.

The most widely used numerical computational tool for performing stress analysis in structures is the Finite Element Method (FEM). Throughout the years, multiple types of element have been developed and regarding composite materials several advancements were introduced with the emergence of cohesive zone modelling. The problem with finite element models of composite aircraft structures is that they tend to be of complex geometry and also present nonlinear behaviour which requires highly discretized meshes and elaborate elements, translating to expensive computational costs.

To tackle this issue, different techniques can be employed within the finite element models, such as adaptative mesh refinement, shell-to-solid coupling, use of reduced integration elements, etc.. For the present work a global-local analysis, consisting in combining different levels of detail and resolution for different regions of a structure, will be employed. In general, the global model is characterized by a coarse mesh and may only include linear elastic behaviour, while the local model has a finer mesh and may account for nonlinear behaviour. This approach can also facilitate the integration of experimental data into the model and can be implemented in one finite element model making use of shell-to-solid coupling for instance, or may be performed in completely separate models that are only connected through boundary conditions extracted from the global one.

1.3 Objectives

Noting the industry shift from the conventional design path, to a more computational focused one, supported by numerical tools, along with the search for virtual certification procedures, the improvement of existing tools such as the FEM are at the vanguard of this change.

From this perspective, and from the arduous modeling of laminated composite materials, the purpose of this work is to develop a global-local finite element model analysis methodology to predict delamination initiation and propagation in laminated composites.

The global-local model will be developed in a one-way configuration, meaning that only information will flow from the global to the local model. Two models will be created, one being an open-hole tensile test, to assess a first implementation of the global-local technique and get a deeper understanding of delamination simulation using cohesive zone modelling, and a second one of a civil aircraft wing-box structure with a laminated composite skin containing an inspection hole on the lower skin that will be the area of interest for the evaluation of delamination behaviour.

1.4 Thesis Layout

Part II exposes the state of the art and a literature review regarding composite structures, aircraft certification, composite failure mechanisms and global-local finite element modeling.

In Part III a review on Cohesive Zone Model (CZM) is conducted and a finite element model of a laminated composite open-hole specimen is developed to validate the global-local approach with experimental and analytical data from the literature, outlining the assumptions made and the cohesive zone modeling settings.

Part IV comprises the main model to be investigated, namely, the civil aircraft wing-box, with the global-local formulation used previously for the validation model, to observe the free-edge delamination effect on the inspection hole.

Part V states the conclusions from the studies performed on this thesis and proposes further works and/or recommendations to improve the methodology developed and continue the research for a better understanding and modeling of laminated composites including damage phenomena.

Part II

State of the art and literature review

Chapter 2

State of the Art

2.1 Composite Structures in Aircraft

The aeronautical industry is a fast paced environment that everyday strives in a quest for superior technologies. Selecting materials for aeronautical or aerospace applications is still a challenge for engineers, since there are multiple considerations and tradeoffs to be taken into account, from temperature requirements, corrosion, durability, damage tolerance, stiffness to costs and environmental aspects [1].

The most used materials for aircraft structural components have been aluminium alloys, dating back to the 1930s. The explanation for the use of aluminium alloys is the well established knowledge either about design, performance or manufacturing processes or even costs [2]. Steel was also adopted in components that required higher stiffness and strength, like landing gear and engine supports [1]. Other metals have also been used in aircraft structural components such as magnesium, mainly in airframes due to its low weight, although it is more expensive and presents inferior structural properties when compared to aluminium. Titanium was introduced by military and commercial aircraft in the 50s, in the development of supersonic aircrafts. In comparison with aluminium, titanium presents better mechanical properties but the higher cost of this metal and its manufacturing processes limit its usage [3].

The first introduction of composites in aircrafts dates back to the 1940s [3], and the driver for their usage was the high strength-to-weight ratio and corrosion resistance. Glass fibres impregnated in polymer matrix, known as Glass Fibre Reinforced Polymer

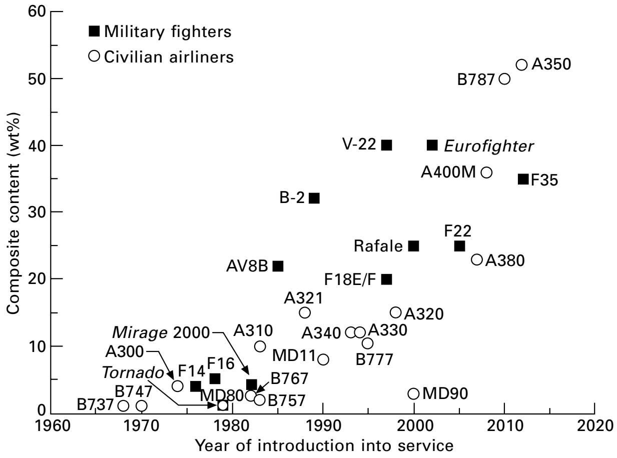

Figure 2.1: Amount of composite materials used in aircraft [3].

(GFRP), were the first set of composite materials used [3]–[5]. Also sandwich-type honeycomb structures were introduced in this decade [6].

In the 1960s, composite materials with boron-based fibres were introduced to the aerospace structures field, and soon evolve to carbon fibre composites, referred to as Carbon Fibre Reinforced Polymer (CFRP) or Polymer Matrix Composite (PMC), empowered by the unfold of commercial production of carbon fibres. [3], [5]. Despite presenting higher strength than carbon, boron fibres were expensive to produce and mainly found its place in military applications were cost was no concern [5]. The remaining aviation community shifted completely to CFRP with the first applications being limited to non-structural components or secondary structures that accounted for less than 5% of the airframe weight [3], [7], [8].

The major milestones in primary structures made out of carbon-fibre composites were firstly observed in military fighter aircraft, like the McDonnell Douglas AV-8B Harrier II and the McDonnell Douglas F/A-18 Hornet. With the development of the knowledge behind composite structures design and manufacturing processes, their application has substantially increased over the years, particularly since the 1990s, with modern airliners like the Airbus A380, A350 and Boeing 787 using composites in their fuselage and wings, as illustrated in Figure 2.1 [3]. It is interesting to note that the A350 and the B787 already crossed the 50% mark.

In summary, the key drivers of using composite materials to substitute the metallic counterparts are [9]:

- less weight
- higher strength
- higher stiffness-to-weight ratio
- improved fatigue performance
- improved corrosion performance
- design flexibility
- ability to tailor properties
- dimensional stability

However, there are several critical issues that emerge from the complexity of composite material systems, such as fibre-matrix selection, adhesion, effects on mechanical properties, inspection, etc. [9]. Therefore, designing and certifying these materials remains a challenge to engineers till today.

2.2 Aircraft Materials Certification

Aircraft material certification is a crucial and meticulous process that has to be carried out in order to ensure safety and reliability. The materials used under go rigorous testing and certification procedures to meet stringent standards set by regulatory authorities, such as the Federal Aviation Administration (FAA) in the United States or the European Union Aviation Safety Agency (EASA) in Europe.

The certification procedures for metal components are well established, due to the extensive knowledge available. However, composite materials present anisotropic behaviour, i.e. mechanical properties differ for each direction, in contrast to metals isotropic behaviour, where the mechanical properties are independent of the direction. Thus, to introduce such materials into aeronautical structures, the certification procedures had to be reworked to accommodate this novel class of materials [10].

A safe design is one that is sufficiently robust to withstand all likely dangers, including the ones explicitly defined in Certifications Specifications. For metallic structures, the two frame bay crack and cracked frame criterion explained by Swift [11] have become a common approach to define robust structures by many Type Certificate Holders, and it works due to fatigue in metallic structures allowing to realistically find progressive crack growth within acceptable timescales and regulatory load thresholds. On the other hand, to obtain the same level of robustness for composite structures design, additional damage modes must be introduced, including ones that are not easily visible, such has weak bonds, disbonds and delaminations [12].

2.2.1 Aircraft design approach

Comprehensive regulations regarding airworthiness that are employed in commercial aircraft designing, manufacturing, operations and maintenance pose as the main pillar to ensure their safety [13]–[16].

Airworthiness can be explained, as sated in an Italian RAI-ENAC Technical Regulations document, as: “For an aircraft, or aircraft part, (airworthiness) is the possession of the necessary requirements for flying in safe conditions, within allowable limits” [17]. This statement highlights the foundations of airworthiness being them:

1. **Safe conditions** –regarding the course and conclusion of the flight [17].

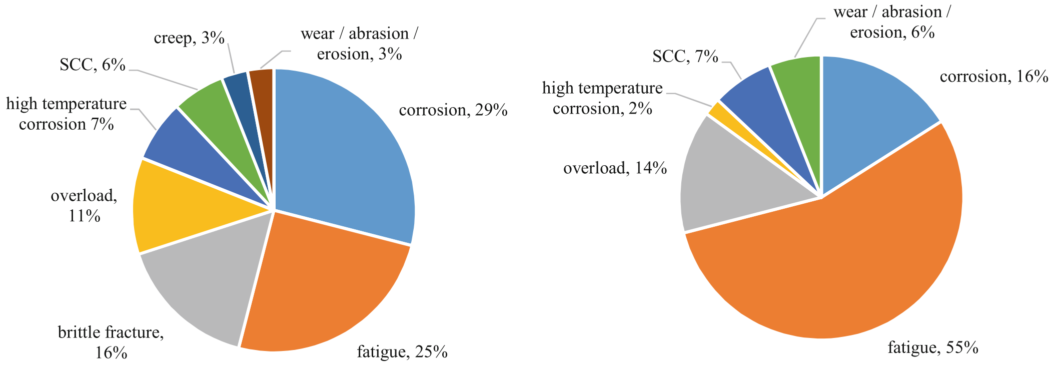

(a) Engineering Components (b) Aircraft Components

Figure 2.2: Frequency of failure mechanisms [15], data retrieved from Findlay and Harison [18]; Gorelik [19].

2. **Possession of necessary requirements** –this refers to the process where an aircraft, including its components, is constructed and engineered in accordance with thoroughly examined and verified standards to ensure safe flight conditions. This is where regulations play their most important role, enhancing safety by removing or minimizing factors that could lead to fatalities, injuries, or damages [17].

3. **Allowable limits** –aircraft are specifically created to function within a defined flight envelope, primarily determined by factors like speed and structural load capabilities. Moreover, the aircraft's maximum weight may vary depending on the type of mission it is intended for. Various operational circumstances are also established, such as day-visual flight rules, night flights, instrumented flights, and operations in icing conditions. It is crucial not to surpass these predetermined conditions and limitations, as doing so can lead to accidents [17].

Aircrafts are prone to many sources of failure. Figure 2.2 summarises the different percentages of such failures and fatigue is clearly the main one.

With fatigue, corrosion and other failure modes in mind, the design philosophy of aircraft structures was shaped to what is referred as Damage Tolerant Design. This design methodology is based on the principle that a structure or structural component operates safely in the presence of damage, that can grow during service until a certain limiting value [15].

One interesting detail when mentioning Damage Tolerance is to understand the different point of view between civil aviation and the military one:

- `FAR 25.571(a)(3)` states "*Based on the evaluations required by this section, inspections or other procedures must be established, as necessary, to prevent catastrophic failure...*" [20].

- `MIL-STD-1530C(3.8)` says that "*Damage tolerance is the attribute of a structure that permits it to retain its required residual strength for a period of unrepaired usage after the structure has sustained specific levels of fatigue, corrosion, accidental, and/or discrete source damage...*" [21].

The civil aviation perspective emphasizes on assuring regular inspections of the aircraft while the military see damage tolerance as a mean to achieve a certain design goal.

Figure 2.3, adapted from Boller and Buderath[22], showcases the different design philosophies that may be adopted.

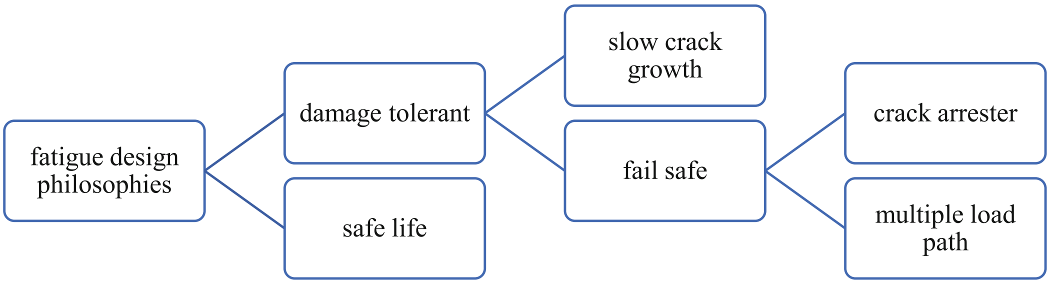

Figure 2.3: Fatigue design philosophies [15], adapted from Boller and Buderath[22].

2.2.2 Regulations

The introduction of composite materials in aircraft construction posed a big challenge not only from a design scope but also from a regulation one. This novel class of materials presented properties that required specific certification procedures [10]. Rouchon exposes the main properties addressed early on in tailoring the certification procedures [10]:

- Sensitivity to environment, mainly concerning matrix dominated properties due to their organic nature.
- High sensitivity to in-plane delamination, which arises from their laminated construction.
- Less sensitivity to fatigue when compared to metals, resulting from the brittle behaviour of thermoset matrices and leading to static strength being the dominant issue.
- Structural properties are process dependant, since the material does not exist before manufacturing the part, which poses obstacles for material qualification and quality assurance.
- Poor electrical conductivity, relevant for lightning certification procedures.

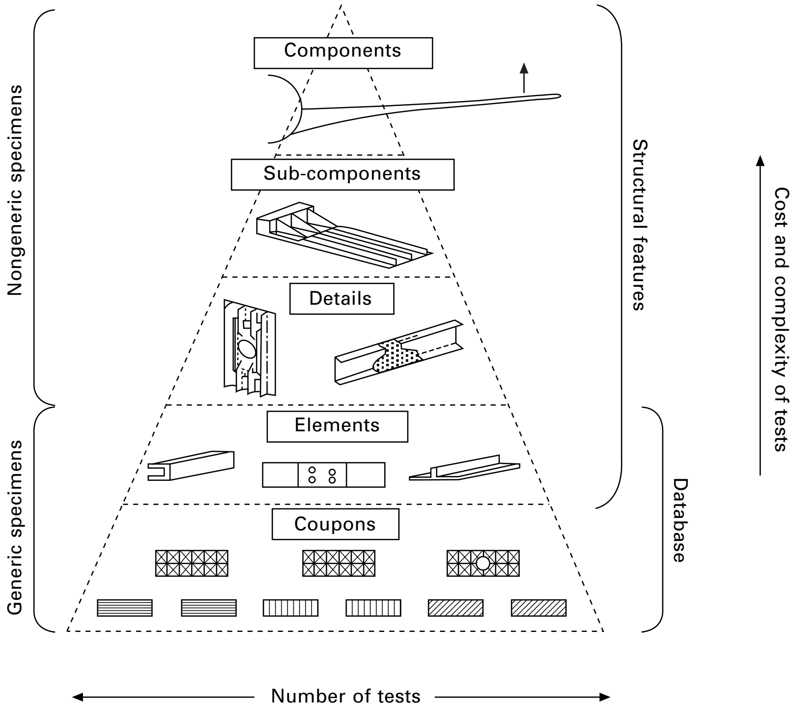

Figure 2.4: Building block approach for certification of aircraft materials and structures [3].

The first primary composite structures certification papers remote to the late 70s with the Advisory Circular (AC) `AC 20 107` [23], issued to deal with DC10 and L1011 vertical fins and Boeing 737 horizontal stabiliser, which all were developed as prototypes in a programme supported by NASA [10]. This AC was intended to be periodically updated to reflect progress drawn from experience. Its latest issue, jointly prepared and agreed upon by FAA and the European member countries of the Joint Airworthiness Requirements (JAR) group, dates back to 1984 [10].

Throughout the years, regulations have been adapting along with data from accidents as well as the improving knowledge on materials such as composites. A summary of regulations evolution is presented on Table 2.1 [16].

Due to composites inherent nature of only providing mechanical properties after being processed, a building block approach was proposed in order to establish a more solid certification path [24]. This building block presents itself in the form of a test pyramid as shown in Figure 2.4.

Nowadays, FAR-25 and CS-25 papers are the compulsory standard requirements issued by the FAA [25] and EASA [26], with the former including the foundation rules for aircraft development and operation, and the latter technical interpretations of airworthiness criteria. This regulations are very extensive documents, that are divided in chapters, with the most important ones being: B (Flight), C (Structure), D(Design and Construction).

Table 2.1: Summary of regulations evolution history.

Period	Regulation	Evolution Stories
1949	CAR 4b.316	Implemented fatigue strength in aircraft designs (based on safety by retirement).
1954	HavillandD.H.106	Full-scale fatigue tests should be detached from static tests.
1956	CAR 4b.270	Introduced fail-safe option, and test validation requirements to the safety by design concept.
1958	B-47	Fatigue analysis cannot solely assure aircraft safety- design loads should be proximate to real operations.
1958-1969	ASIP series Doc.	Incorporated ASIP for military aircraft, to ascertain fatigue life with full-scale fatigue tests.
1964	14 CFR 25.571	CAR 4b.270 was rectified to 14 CFR 25.571 without major alterations.
1968	ASD-TR-66-57	Necessary tests for 1) Materials; 2) Machining processes; 3) Joints to final assemblies.
1970	F-5	It is necessary to balance designs for static and fatigue. introduced cold working as a way to increase tiredness.
1966-1977	KC-135	Static and fatigue designs must be balanced, and material selection is crucial.
1972	MIL-SID-1530	Validation tests for coupons, junctions, components, structural operating mechanisms and control systems were necessary for ASIP.
1978	Amdt.25-45/AC 25.571-1	Increased Damage Tolerance Requirements for every civil aircraft, including in-service fleets.
1986	AC 25.571-1A	Taken into account separate source damages.
1997	AC 25.571-1 B	Instituted the concept of scatter factors in certification.
1998	Amdt.25-96/AC 25.571-1C	Required test validations for No WFD appeared before DSG for civil aircraft.
2004	MIL-STD-1530B	Superseded MIL-HDBK1530B, in which the required items for corrosion were included.
2005	MIL-STD-1530C	Risk analysis was included into ASIP and a link to airworthiness certification was made.
2010	Amdt.25-132/AC 25.571-1D	Establish LOV validation standards for civil aircraft that are applicable to all currently operating aircraft.
2016	MIL-STD-1530D	Adding criteria for composite, cost-effective service life, and ndi method capabilities.

2.3 Composite Failure Mechanisms

Composite materials are a remarkable class of engineering materials known for their exceptional strength-to-weight ratio, making them increasingly popular in diverse industries. However, their unique composition presents complex challenges in understanding and predicting failure mechanisms. The intricate interplay of its constituent materials and their interfaces can lead to a wide range of failure modes [27]–[30].

Before breaking apart, laminated materials typically undergo various localized failures at smaller scales, discrete damage events. These events include fibre breakage, pull-out, or kinking/buckling, as well as matrix cracking and fiber/matrix debonding. Additionally, there is also delamination between plies. These damages progressively develop and build up during the loading [30]–[35].

Failure of composite structures may be considered under two different approaches:

- First Ply Failure (FPF) - usually characterized by matrix-dominated mechanisms that lead to complete structural collapse, even without fibre breakage [30]. This approach is commonly used in the aeronautical field.
- Last Ply Failure (LPF) - induced by fibre-dominated mechanisms in a catastrophic fashion [30].

The different types of failures mechanisms, Figure 2.5, can be arranged in two big categories, namely intralaminar and interlaminar damage. Intralaminar damage relates to the unique underlying micromechanical failure modes, while interlaminar damage refers to the interfacial separation of plies [30], [35].

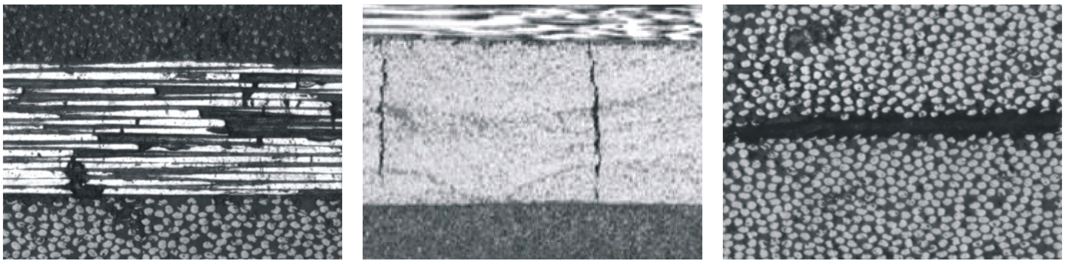

(a) Fibre breakage (b) Matrix transverse cracking (c) Delamination

Figure 2.5: Types of damage in laminated composites [36].

Developing accurate failure criteria has been the main focus regarding numerical simulation of composite materials. Often in the literature, there are many papers establishing comparisons between different failure criteria such as the *Worldwide Failure Exercise* [37], [38]. The next subsections will focus on outlining the main criteria found in the literature.

2.3.1 Fibre Failure

Fibre failure in tension takes place in composite laminates as a result of the accumulation of individual fibre failures within plies, that gets critical when there are insufficient undamaged fibres remaining to carry the required loads. The common practice among authors was to analyse fibre failure in tension through a maximum stress or maximum strain criteria at the ply level, using experimental results as reference values [39]. However, some authors took other approaches at the subject like a quadratic interaction criteria involving in-plane shear, proposed by Hashin [40], and later modified by Chang [41] to consider nonlinear shear behaviour. In the other hand Puck and Schürmann [42] utilised a max strain criterion including a stress magnification factor relating to normal stress. The aforementioned approaches to fibre failure are summarised in Table 2.2.

Table 2.2: Failure criteria for fibres under tension [39].

Criteria	Equation
Fibre Max-stress	$\sigma_1 \geqslant X_\mathrm{T}$
Fibre Max-strain	$\varepsilon_1 \geqslant \varepsilon_{1_\mathrm{T}}$
Hashin-3D (1980) [40]	$\left(\frac{\sigma_1}{X_\mathrm{T}}\right)^2 + \frac{1}{S_{12}^2}\left(\tau_{12}^2 + \tau_{13}^2\right) \geqslant 1$
Hashin-2D (1980) [40]	$\left(\frac{\sigma_1}{X_\mathrm{T}}\right)^2 + \left(\frac{\tau_{12}}{S_{12}}\right)^2 \geqslant 1$
Chang-Chang (1987) [41]	$\sqrt{\left(\frac{\sigma_1}{X_\mathrm{T}}\right)^2 + \frac{\tau_{12}^2/2G_{12}+\frac{3}{4}\alpha\tau_{12}^4}{S_{12_\mathrm{is}}^2/2G_{12}+\frac{3}{4}\alpha S_{12_\mathrm{is}}^4}} \geqslant 1$
Puck (1998) [42]	$\frac{1}{\varepsilon_{1_\mathrm{T}}}\left(\varepsilon_1 + \frac{\nu_{\mathrm{f}12}}{E_{\mathrm{f}1}} m_{\mathrm{f}_\sigma}\sigma_2\right) \geqslant 1$

Compression-induced fiber failure manifests through the intricate interplay of two fundamental mechanisms: microbuckling and the emergence of kink bands. While the classification of these phenomena as distinct failure modes is still a matter of discussion, microbuckling is generally regarded as a more widespread form of failure, whereas kinking tends to initiate from localized microstructural imperfections and represents the predominant failure characteristic observed in post-test analysis. [34]. Table 2.3 highlights the different criteria for the compression case.

Table 2.3: Failure criteria for fibres under compression [39].

Criteria	Equation
Fibre Max-stress	$\sigma_1 \geqslant X_\mathrm{C}$
Fibre Max-strain	$\varepsilon_1 \geqslant \varepsilon_{1_\mathrm{C}}$
Greszczuk (1974) [43]	$\sigma_1 \geqslant \frac{G_{12}^\mathrm{m}}{1-V_\mathrm{f}}$
Chang-Lessard(1991) [44]	$\sigma_1 \geqslant \bar{X}_\mathrm{C}$
Puck (1998) [42]	$\frac{1}{\varepsilon_{1\mathrm{c}}} \left\lvert \left(\varepsilon_1 + \frac{\nu_{\mathrm{f}12}}{E_{\mathrm{f}1}} m_{\mathrm{f}_\sigma} \sigma_2 \right) \right\rvert \geqslant 1 - \left(10\gamma_{21}\right)^2$
LaRC03 (2003) [45]	$\sigma_{22}^m < 0 : \left\langle \frac{\lvert\tau_{12}^m\rvert + \eta_{12}\sigma_{22}^m}{S_{12_\mathrm{is}}} \right\rangle \geqslant 1$
	$\sigma_{22}^m > 0 : (1-g)\left(\frac{\sigma_{22}^m}{Y_{T_\mathrm{k}}}\right) + g\left(\frac{\sigma_{22}^m}{Y_{T_\mathrm{ks}}}\right)^2 + \left(\frac{\tau_{12}^m}{S_{12\ \mathrm{s}}}\right)^2 \geqslant 1$
LaRC04 (2005) [34]	For $\sigma_{2m2m} < 0 : \frac{\lvert\tau_{1m2m}\rvert}{S_{12\ \mathrm{s}} - \eta_{12}\sigma_{2m2m}} \geqslant 1$
	For $\sigma_{2m2m} > 0 :$
	$(1-g)\left(\frac{\sigma_{2m2m}}{Y_{\mathrm{T}_\mathrm{is}}}\right) + g\left(\frac{\sigma_{2m2m}}{Y_{T_\mathrm{is}}}\right)^2 + \frac{\Lambda_{23}^0 \tau_{2m3\varphi}^2 + \chi(\gamma_{1m2m})}{\chi\left(\gamma_{12_\mathrm{i}}^u\right)} \geqslant 1$
Maimí et al. (2007) [46]	$\left\langle \lvert\tau_{12}^m\rvert + \eta_{12}\sigma_{22}^m \right\rangle / S_{12} \geqslant 1$

Besides fibre failure under tension or compression as separate failure modes, some authors developed formulations that account for both mechanisms,Table 2.4.

Table 2.4: Failure criteria for fibres under tension and compression [39].

Criteria	Equation
Lee (1982) [47]	$\sigma_1 \geqslant \sigma_\mathrm{FN}$ or $\sqrt{\left(\sigma_{12}^2 + \sigma_{13}^2\right)} \geqslant \sigma_\mathrm{FS}$
Christensen (1997) [48]	$\alpha_2 k_2 \sigma_1 + \frac{1}{4}(1+2\alpha_2)\sigma_1^2 - \frac{(1+\alpha_2)^2}{2}\frac{(\sigma_2+\sigma_3)}{2}\sigma_1 \leqslant k_2^2$
Huang et al. (2003) [49]	Use dissipated energy density $\phi(\varepsilon)$ to indicate damage: fibre failure for $\phi(\varepsilon) > D_t$, where D_t is the dissipated energy density threshold.

2.3.2 Matrix Failure

Matrix failure of laminated composites is complicated phenomenon, characterized by the initiation of matrix cracks primarily at defect sites or fiber-matrix interfaces. These cracks gradually propagate throughout the laminate, ultimately converging and culminating in failure along a crucial fracture plane. Extensive literature has been dedicated to the analysis of matrix cracking and failure, with numerous scholars devising approaches to forecast crack initiation. Employing fracture mechanics theories, these studies aim to predict the growth and accumulation of damage stemming from pre-existing cracks, as well as anticipate the angle of the fracture plane under diverse loading conditions [39].

Matrix failure in tension assumes a critical fracture plane along the transverse tension direction, normally involving an interaction between in-plane shear stresses and the tensile normal. In a similar fashion to fibre failure, the maximum stress or maximum stress criteria are often used. The Hashin and Rotem proposal [50] relies in a quadratic interaction criterion that like the fibre counterpart was further developed to include important aspects, such as nonlinear shear terms, in situ transverse tensile and shear strengths, incorporating crack density, the use of through-thickness shear and strength terms, and the inclusion of fracture mechanics terms from a consideration of a cracked ply. [39]. Table 2.5 presents the formulation for the different criteria. It is important to denote that the Cuntze and Freund [51] one is only based on transverse tensile stress and strength and through-thickness shear stress. Table 2.6 and Table 2.7 show the formulations relating to compression and to both tension and compression, respectively.

Table 2.5: Matrix failure under tension criteria [39].

Criteria	Equation
Matrix Max-stress	$\sigma_2 \geqslant Y_\mathrm{T}$
Matrix Max-strain	$\varepsilon_2 \geqslant \varepsilon_{2_\mathrm{T}}$
Hashin-3D (1980) [40]	$\frac{(\sigma_2+\sigma_3)^2}{Y_\mathrm{T}^2} + \frac{\tau_{23}^2-\sigma_2\sigma_3}{S_{23}^2} + \frac{\tau_{12}^2-\tau_{13}^2}{S_{12}^2} \geqslant 1$
Chang-Chang (1987) [41]	$\sqrt{\left(\frac{\sigma_2}{Y_\mathrm{T}}\right)^2 + \frac{\tau_{12}^2/2G_{12}+\frac{3}{4}\alpha\tau_{12}^4}{S_{12_\mathrm{s}}^2/2G_{12}+\frac{3}{4}\alpha S_{12_\mathrm{s}}^4}} \geqslant 1$
Puck (1998) [42]	$\sqrt{(\tau_{21}/S_{21})^2 + \left(1-p_{\perp 1}^{(+)}Y_\mathrm{T}/S_{21}\right)^2(\sigma_2/Y_\mathrm{T})^2 +}$ $p_{11}^{(+)}\sigma_2/S_{21} \geqslant 1-\lvert\sigma_1/\sigma_{1\mathrm{D}}\rvert$
LaRC03 (2003) [45]	$(1-g)\left(\frac{\sigma_2}{Y_{\mathrm{T_h}}}\right) + g\left(\frac{\sigma_2}{Y_{\mathrm{T_k}}}\right)^2 + \left(\frac{\tau_{12}}{S_{12_\mathrm{h}}}\right)^2 \geqslant 1$
Cuntze (2004) [51]	$\left[I_2+\sqrt{I_4}/2Y_\mathrm{T} \geq 1\right]$ $I_2=\sigma_2+\sigma_3, I=(\sigma_2-\sigma_3)^2+4\tau_{23}^2$
LaRC04 (2005) [34]	$(1-g)\left(\frac{\sigma_2}{Y_{\mathrm{T_k}}}\right) + g\left(\frac{\sigma_2}{Y_{\mathrm{T_k}}}\right)^2 + \frac{\Lambda_{23}^0\tau_{23}^2+\chi(\gamma_{12})}{\chi\left(\gamma_{12_\mathrm{h}}^{\mu}\right)} \geqslant 1$
Maimí et al. (2007) [46]	$\sigma_2 \geqslant 0: \sqrt{(1-g)\left(\frac{\sigma_2}{Y_\mathrm{T}}\right) + g\left(\frac{\sigma_2}{Y_\mathrm{T}}\right)^2 + \left(\frac{\tau_{12}}{S_{12}}\right)^2} \geqslant 1$ $\sigma_2 < 0: \left\langle\lvert\tau_{12}\rvert+\eta_{12}\sigma_2\right\rangle/S_{12} \geqslant 1$

Table 2.6: Matrix failure under compression criteria [39].

Criteria	Equation
Matrix Max-stress	$\sigma_2 \geqslant Y_\mathrm{C}$
Fibre Max-strain	$\varepsilon_2 \geqslant \varepsilon_{2_\mathrm{C}}$
Hashin-2D (1980) [40]	$\sigma_2/Y_C\left[(Y_c/2S_{23})^2-1\right]+(\sigma_2/2S_{23})^2+(\tau_{12}/S_{12})^2 \geqslant 1$
Chang-Lessard (1991) [44]	$\sqrt{(\sigma_2/Y_\mathrm{C})^2+\frac{\tau_{12}^2/2G_{12}+\frac{3}{4}\alpha\tau_{12}^4}{S_{12\ \mathrm{s}}^2/2G_{12}+\frac{3}{4}\alpha S_{12\ \mathrm{s}}^4}} \geqslant 1$
Puck (1998) [42]	For 2D plane stress, Mode B, $\theta_\mathrm{fp}=0°$, $\frac{1}{S_{21}}\left(\sqrt{\tau_{21}^2+\left(p_{\perp 1}^{(-)}\sigma_2\right)^2}+p_{\perp 1}^{(-)}\sigma_2\right) \geqslant 1-\left\lvert\frac{\sigma_1}{\sigma_{1\mathrm{D}}}\right\rvert$ for $\sigma_2<0$ and $0 \leqslant \lvert\sigma_2/\tau_{21}\rvert \leqslant R_{\perp\perp}^A/\lvert\tau_{21c}\rvert$
LaRC03 (2003) [45]	$\sigma_1<Y_\mathrm{C}:\tau_{23_\mathrm{em}}^\mathrm{m}/S_{23}+\tau_{12_\mathrm{em}}^\mathrm{m}/S_{12_\mathrm{is}} \geqslant 1$ $\sigma_1 \geqslant Y_\mathrm{C}:\tau_{23_\mathrm{err}}/S_{23}+\tau_{12_\mathrm{em}}/S_{12_\mathrm{s}} \geqslant 1$ τ_{23}^m, τ_{12}^m : stresses in 2D kink frame, at φ
LaRC04 (2005) [34]	$\sigma_1 \geqslant -Y_\mathrm{C}:\left(\frac{\tau_{23}^\alpha}{S_{23}-\eta_{23}\sigma_n}\right)^2+\left(\frac{\tau_{12}^\alpha}{S_{12\ \mathrm{s}}-\eta_{12}\sigma_n}\right)^2 \geqslant 1$ $\sigma_1<-Y_\mathrm{C}:\left(\frac{\tau_{23}^m}{S_{23}-\eta_{23}\sigma_n^m}\right)^2+\left(\frac{\tau_{12}^m}{S_{12}-\eta_{12}\sigma_n^m}\right)^2 \geqslant 1$ $\sigma_n, \tau_{23}^\alpha, \tau_{12}^\alpha$: stresses in fracture plane, at α $\sigma_n^m, \tau_{23}^m, \tau_{12}^m$: stresses in 3D kink frame, at ϕ, φ
Maimí et al. (2007) [46]	$\sqrt{(\tau_{23}/S_{23})^2+(\tau_{12}/S_{12})^2} \geqslant 1$ $\alpha_0=53°, \theta=\arctan(-\sigma_{12}/\sigma_{22}\sin\alpha_0)$ $\tau_{23_{er}}=\langle -\sigma_{22}\cos\alpha_0\left(\sin\alpha_0-\eta_{23}\cos\alpha_0\cos\theta\right)\rangle$ $\tau_{12_{er}}=\langle\cos\alpha_0\left(\lvert\tau_{12}\rvert+\eta_{12}\sigma_{22}\cos\alpha_0\sin\theta\right)\rangle$

Table 2.7: Failure criteria for matrix in tension and compression [39].

Criteria	Equation
Lee (1982) [47]	$\sigma_2 \geqslant \sigma_{\mathrm{MN}}$ or $\sqrt{\left(\sigma_{12}^2+\sigma_{13}^2\right)} \geqslant \sigma_{\mathrm{MS}}$
Christensen (1997) [48]	$\alpha_1 k_1 \left(\sigma_2+\sigma_3\right)+\left(\sigma_{12}^2+\sigma_{31}^2\right)+$ $\left(1+2\alpha_1\right)\left[\frac{1}{4}\left(\sigma_2-\sigma_3\right)^2+\sigma_{23}^2\right] \leqslant k_1^2$ $k_1=S_{12}=\frac{1}{2}\left\|Y_{\mathrm{C}}\right\|, \alpha_1=\frac{1}{2}\left(\|\mathrm{Y}_{\mathrm{C}}/\mathrm{Y}_{\mathrm{T}}-1\right)$
Gosse (2001) [52]	$J_1=\varepsilon_1+\varepsilon_2+\varepsilon_3$ or $\varepsilon_{\mathrm{eqv}}=\sqrt{\frac{\left(\varepsilon_1-\varepsilon_2\right)^2+\left(\varepsilon_1-\varepsilon_3\right)^2+\left(\varepsilon_2-\varepsilon_3\right)^2}{2}}$
Huang et al. (2003) [49]	Failure when $J_1 \geqslant J_{1_{\mathrm{crit}}}$ or $\varepsilon_{eqv} \geqslant \varepsilon_{\mathrm{eqv\ crit}}$ use dissipated energy density $\phi(\varepsilon)$: matrix failure for $0 \leqslant \phi(\varepsilon) \leqslant D_t$

2.3.3 Delamination

Delamination is a significant mode of failure observed in laminated fibre-reinforced polymer matrix composites. It plays a crucial role in distinguishing their behaviour from that of the metallic counterpart. This failure mechanism occurs as a result of elevated interlaminar stresses combined with the inherent low through-thickness strength exhibited by these composites. The underlying cause stems from the limited reinforcement provided by fibres oriented within the plane of the laminate, rendering the composite reliant on the relatively weaker matrix to bear loads in the perpendicular direction. Furthermore, the typically brittle nature of matrix resins exacerbates this phenomenon [53].

Delamination can occur due to various sources. Figure 2.6 depicts the most common ones, being them: curved free edges, external ply drops, corners, skin stiffener interaction, solid-sandwich transitions, internal ply drops and straight free edges [54].

Modeling of delamination failure was possible with the development of fracture mechanics concepts. To correctly understand delaminations one must know beforehand the different fracture modes possible [54], Figure 2.7:

- **Mode-I** - portrays the opening of crack faces.

- **Mode-II** - represents the sliding mode.
- **Mode-III** - depicts the tearing mode, i.e., out of plane shear.

Another important concept for comprehending delamination is the strain energy release rate, commonly denoted as G, which traduces the driving force for propagation of a crack. Back in 1957, Irwin [55], derived an expression to calculate the work necessary to close a crack of length $a+\Delta a$ to a length a. He assumed that for brittle materials, since they do not go under significant plastic deformations or even none, all the external energy supplied would contribute to create new cracks. Therefore, the work to close the crack would be equal to the one necessary to extend the crack from a to $a+\Delta a$. From this Irwin obtained the following equation for the strain energy release rate, G:

$$G = \lim_{\Delta a \to 0} \frac{W}{\Delta a} = \lim_{\Delta a \to 0} \frac{1}{2\Delta a} \int_0^{\Delta a} \sigma_y(\Delta a - r) \cdot v(r)\, dr \tag{2.1}$$

The importance of this concept of energy release rate is that it can be associated to different modes of fractures to determine the interlaminar fracture toughness for each case and thus predict the the beginning and progression of delamination. For each mode, the strain energy release rate symbol takes the index leading to G_I, G_{II} and G_{III}. In order to determine this quantities the American Society for Testing and Materials (ASTM) developed specific experiments for each mode, which can be found in the `MIL Handbook 17` [56]. The setups explored in this document are:

- Double Cantilver Beam (DCB) for Mode-I.
- Mixed Mode Beding (MMB) for mix Mode-I and Mode-II
- End Notch Flexure (ENF) for pure Mode-II.

The determination of interlaminar fracture toughness involves evaluating a critical value of the strain energy release rate, denoted as G_c, which is graphically represented as a function of the mixed-mode ratio, G_{II}/G [54], Figure 2.8.

To enable the propagation of delamination, a criterion that accounts for mixed-mode failure is necessary. One such criterion is the power-law criterion, originally formulated by Wu and Reuter in 1965 [57], which can be expressed as follows (m, n and p are empirically determined):

$$\left(\frac{G_I}{G_{Ic}}\right)^m + \left(\frac{G_{II}}{G_{IIc}}\right)^n + \left(\frac{G_{III}}{G_{IIIc}}\right)^p \geq 1 \tag{2.2}$$

Another well known criterion is the one developed by Benzeggagh and Kenane in 1966 [58], applicable for 2D problems:

$$\frac{G_I + G_{II}}{G_{Ic} + (G_{IIc} - G_{Ic}) \left[\frac{G_{II}}{G_I + G_{II}}\right]^m} \geq 1 \tag{2.3}$$

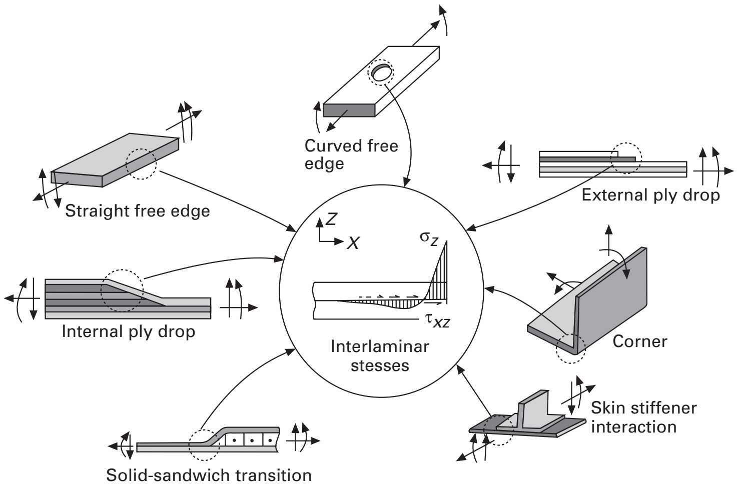
Curved free edge
Straight free edge
External ply drop
Z
X
σz
τxz
Interlaminar stesses
Internal ply drop
Corner
Skin stiffener interaction
Solid-sandwich transition

Figure 2.6: Delamination sources [54].

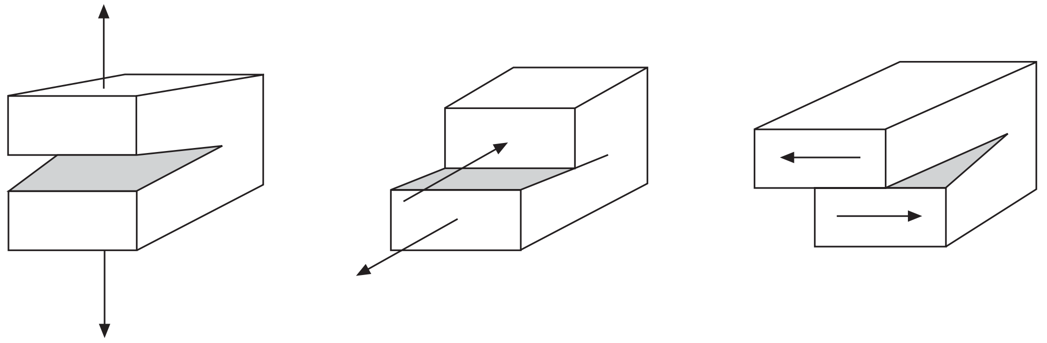

Mode-*I* (opening) Mode-*II* (sliding shear) Mode-*III* (tearing shear)

Figure 2.7: Fractures modes [54].

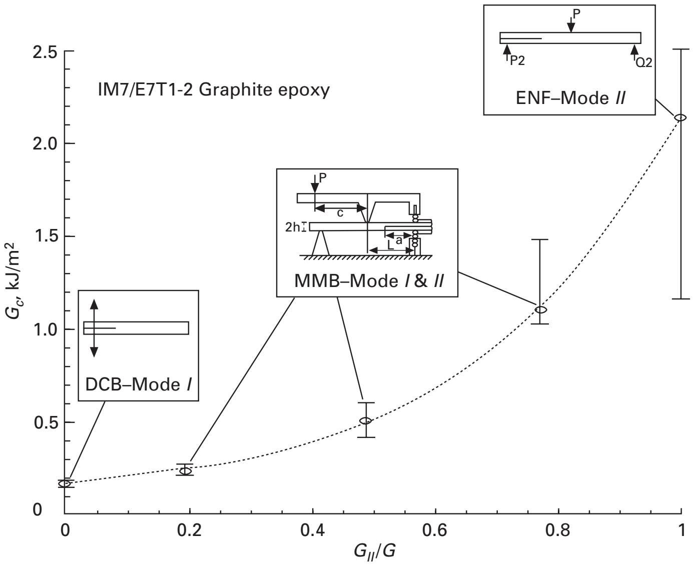

Figure 2.8: Criteria for Mode-I and Mode-II delamination [54].

For the 3D case, Reeder [59] derived another criterion, which accounted for different values of G_{IIc} and G_{IIIc}:

$$\frac{G_I + G_{II} + G_{III}}{G_{Ic} + \left(\frac{G_{II}(G_{IIc}-G_{Ic})+G_{III}(G_{III}-G_{Ic})}{G_I+G_{II}+G_{III}}\right)\left[\frac{G_{II}+G_{III}}{G_I+G_{II}+G_{III}}\right]^{m-1}} \geq 1 \tag{2.4}$$

Table 2.8 and Table 2.9 summarise some of the most commonly used failure criteria for delamination initiation and propagations, respectively.

Table 2.8: Failure criteria for delamination initiation [39].

Criteria	Equation
Max stress initiation	$\sigma_3 \geqslant Z_\mathrm{T}, \tau_{31} \geqslant S_{31}, \tau_{23} \geqslant S_{23}$
Hashin (1982) [40]	$\left(\frac{\sigma_3}{Z_\mathrm{T}}\right)^2 + \left(\frac{\tau_{23}}{S_{23}}\right)^2 + \left(\frac{\tau_{31}}{S_{31}}\right)^2 \geqslant 1$
Lee (1982) [47]	$\sigma_3 \geqslant Z_\mathrm{T}$ or $\sqrt{(\sigma_{12}^2 + \sigma_{13}^2)} \geqslant S_{23}$
Tsai (1997) [60]	$\frac{\sigma_1^2-\sigma_1\sigma_3}{X_\mathrm{T}^2} + \left(\frac{\sigma_3}{Z_\mathrm{T}}\right)^2 + \left(\frac{\tau_{23}}{S_{23}}\right)^2 \geqslant 1$
Tong-Tsai (1997) [60]	$\frac{\sigma_1^2-\sigma_1\sigma_3}{X_\mathrm{T}^2} + \left(\frac{\sigma_3}{Z_\mathrm{T}}\right) + \left(\frac{\tau_{23}}{S_{23}}\right)^2 \geqslant 1$
Degenerated Tsai (1997) [60]	$\left(\frac{\sigma_1}{X_\mathrm{T}}\right)^2 + \left(\frac{\sigma_3}{Z_\mathrm{T}}\right)^2 + \left(\frac{\tau_{23}}{S_{23}}\right)^2 \geqslant 1$

Table 2.9: Failure criteria for delamination propagation [39].

Criteria	Equation
Power Law Growth (1984) [61]	$\left(\frac{G_\mathrm{I}}{G_\mathrm{Ic}}\right)^m + \left(\frac{G_\mathrm{II}}{G_\mathrm{IIc}}\right)^n + \left(\frac{G_\mathrm{II}}{G_\mathrm{IIc}}\right)^p \geqslant 1$
Yan et al. (1991) [62]	$G_\mathrm{T} \geqslant G_{I_c} + \rho\frac{G_{II}}{G_I} + \tau\left(\frac{G_{II}}{G_I}\right)^2$
Reeder (1993) [63]	For $\frac{G_{II}}{G_I} < \frac{\frac{1}{\zeta}G_{I_c}+G_{I_{I_c}}}{G_{I_c}+\xi G_{I_c}}, \frac{G_I-\xi G_{II}}{G_{I_c}} \geqslant 1$ For $\frac{G_{II}}{G_I} < \frac{\frac{1}{\zeta}G_{I_c}+G_{I_c}}{G_{I_c}+\xi G_{I_c}}, \frac{\zeta G_{II}-G_I}{\zeta G_{II_c}} \geqslant 1$
B-K Law (1966) [58]	$G_\mathrm{T} \geqslant G_{I_\mathrm{C}} + \left(G_{I_\mathrm{C}} - G_{I_\mathrm{C}}\right)[G_{II}/(G_I + G_{II})]^\eta$

2.3.4 Interface elements

The first step to model and compute delamination in composite materials stands on the necessity to use the correct interface method to stimulate the adhesive, where usually a fracture mechanics approach is applied for delamination growth investigations to appraise the energy release rates G for self-similar delamination development [64].

The delamination models are divided into two different topics such as initiation and propagation and most of its assessments are stress-based with the inclusion of some criteria like the quadratic interaction of the interlaminar stresses in combination with a characteristic distance. Thus, it is necessary to apply some significant testing due to the fact that the typical distance is an average length that depends on the geometry and material qualities [64]–[66].

To evaluate energy rates it is commonly used the Virtual Crack Closure Technique (VCCT) developed by Rybicki and Rybicki and Kanninen [67] based on Irwin's assumption. In this method, just one analysis is necessary to determine the energy release rates which makes it computationally efficient [64].

Useful insights from the VCCT may be taken regarding the onset and delamination stability in a delamination growth simulation, but it might be required to use a more powerful and advanced moving mesh technique to force the crack front when local energy rates reach critical levels [68]. Furthermore, the hardest part may be the determination of the delamination front location regarding some unusual geometries and load scenarios, which mandate the inclusion of a specified starting delamination.

Thereby, to overcome the difficulties aforementioned (de)cohesion elements may be used at the interfaces between laminates. These are primarily explained by Dudgale-Barenblatt cohesive zone approach [69], [70], [85] base Griffith's fracture theory for a negligible cohesive size when compared with the characteristic dimensions, independently from constitutive equation shape [71]. Beyond that, it allows the simulation to predict both the onset and propagation of the delamination even if there is no previous information of the crack's location and propagation direction [64].

Two different groups of decohesion elements may be formed, with one being that of continuous interface elements and the other of point decohesion elements. The employment of streamlined interaction criteria of energy release rates for delamination propagation prediction and the absence of an interaction requirement for softening initiation prediction under mixed-mode loading are hallmarks of previously established decohesion components.

2.4 Global-Local FEM

Quite often finite element models become too complex to be modelled with fully 3D meshes that could translate to unfeasible simulation times, so analysts have to resort to more computational efficient elements such as shell elements. However, this switch from a 3D formulation to a 2D one comes at some expense, and can affect the accuracy of the model. One way to tackle this without compromising too much the computational cost is the use of global-local approaches [72].

The search to develop accurate and faster numerical tools has been a quest of engineers over the years with several works focusing on the meshing scales issue for different subregions [73], [74]. Global-Local techniques emerged as way to overcome the limitations of local multigrid algorithm in finite element formulations, such as the one proposed by Brandt [73] and further developed by Parsons and Hall [74]. This type of approach presented some major drawbacks as the usually are intrusive in commercial finite element codes and also due to complex transfer of information between meshes at the overlapped region.

Having this into consideration, Gendre et al. [75] suggested a non-intrusive coupling concept to analyse local non-linearities within the purpose of reducing the FE codes resources where it use the non-overlapping domain decomposition (DD) data transfer method to modify the conventional global/local method.

There are two models for the iterative global/local algorithm: a nonlinear local fine mesh and a linear global coarse mesh models. The technique indicates that the boundary or interface of both meshes must match. Therefore, the iterative global/local approach presents several benefits except for the matching mesh on the interface, where the data transfer of nodal displacement and force between the two models only occurs along the interface by avoiding any modification of the industrial code or the solver [76].

There are multiple manners of connecting the different models that make up the solution scheme ranging from one and two-way strategies, to loose and tight coupling procedures, which are potential distinctions of the modern technologies. One-way coupling refers to the fact that information is only transferred from one model to another whether from the global to the local or vice-versa while two-way coupling, as the name says, transmit information in both directions. In loose coupling procedures it is necessary to separate models to be able to have different simulations that share information that can be computed sequentially which is not the same in tight coupling because it can resolve the global and local systems of equations simultaneously [77].

2.4.1 Submodeling in Abaqus

The finite element commercial software `Abaqus` has already implemented in its code the features necessary to perform a submodeling technique in a intuitive fashion. Using this feature a small areas within complex models can be refined and used to interpolate the global model's solution. This modeling strategy is useful when a precise and detailed answer is needed for the local area, but the detailed modeling of that area does not significantly impact the overall solution. The overall solution, along with any applied loads on the local area, determines the response at the boundary of the local region, which then influences the solution of the submodel. The accuracy of the submodel's boundary reaction is dependent on the accurate specification of the global model.

Abaqus provides two submodeling techniques: node-based and surface-based. The node-based approach is particularly interesting because it allows for a useful technique called shell-to-solid submodeling. This technique saves computational efforts by defining a large-scale shell model and transferring the boundary conditions to a more complex solid model, resulting in more detailed results for the local area of interest.

Shell-to-solid submodeling

To account for discontinuities and slight misalignments between the nodes in the shell model and the corresponding locations in the solid model, an interpolation procedure is necessary to accurately transfer the displacement field. Abaqus incorporates two types of tolerances to establish the relationship between the local and global models.

The first step is to identify the nearest location on the global model's shell mid-surface. This point is then referred to as the "image node" of the driven node. To determine if the image node falls within the scope of the global model, an external tolerance parameter is utilized. Subsequently, the distance between the driven node and its image node is compared to half of the maximum shell thickness specified by the user, as shown in Figure 2.9.

If the distance between the driven node and its image node falls within half of the maximum shell thickness plus the external tolerance, the node is considered acceptable. However, if the global model has varying shell thicknesses, this check will only provide an approximate accuracy and may not protect the user in areas of the global model where the thickness is less than the maximum thickness set by the user.

Once the positions of the driven nodes (or image nodes in the case of shell-to-solid example) have been determined, the prescribed values of the driven variables are interpolated from the results obtained from the output file of the global model.

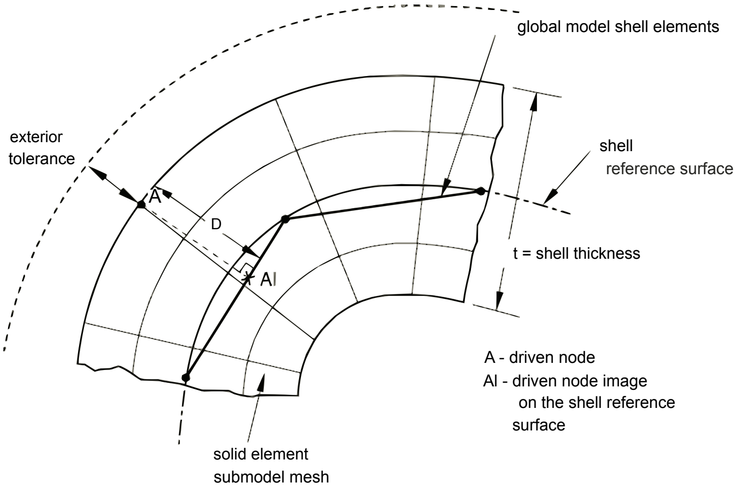
global model shell elements
exterior tolerance
shell reference surface
A
D
AI
t = shell thickness
A - driven node
AI - driven node image on the shell reference surface
solid element submodel mesh

Figure 2.9: Centre zone definition for shell-to-solid submodeling. [78].

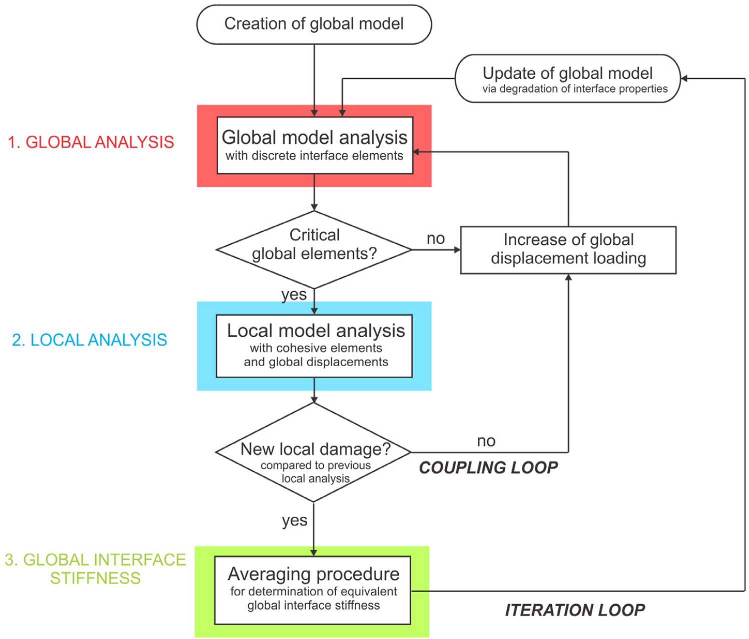
Creation of global model
Update of global model
via degradation of interface properties
1. GLOBAL ANALYSIS
Global model analysis
with discrete interface elements
Critical
global elements?
no
Increase of global
displacement loading
yes
2. LOCAL ANALYSIS
Local model analysis
with cohesive elements
and global displacements
New local damage?
compared to previous
local analysis
no
COUPLING LOOP
yes
3. GLOBAL INTERFACE
STIFFNESS
Averaging procedure
for determination of equivalent
global interface stiffness
ITERATION LOOP

Figure 2.10: Typical two-way loose coupling procedure [72].

2.4.2 Applications of global-local technique in the literature

The global-local technique has been around for sometime and has been employed in finite element analyses of delamination by several researchers. Multiple works focused on the enhancement of already developed global-local formulations in order to ease their setup and provide more accurate results. For example, Krueger and O'Brien [79] developed a shell/3D modelling technique to investigate delamination composites by simulating DCB, ENF and Single Leg Beding (SLB) using VCCT. Another work using VCCT and submodeling is the one by Pietropaoli and Riccio [80], where this techniques and a ply discount approach are combined to predict interlaminar and intralaminar damage evolution in composite stiffened panels subject to compressive loads.

A very common topic of research using global-local techniques is the case of skin-stringer debonding in composite structures. In this particular application, many of the methodologies found in the literature resort to the two-way loose coupling procedures, shown in Figure 2.10.

This type of procedure has been implemented in various skin-stringer analyses using several commercial Finite Element (FE) softwares. The exchange of information between models is done in an iterative fashion, as depicted in Figure 2.10. In this process, non-linear studies are not interrupted because the global and local simulations are executed sequentially rather than concurrently. When updating the global model, it is worth noting that modifications were made to the material properties.

Akterskaia *et al.*[72] proved that the global-local technique can be beneficial, when properly defined, resulting in computational time savings, which in that case was around

65%.

As for panel with cut-outs, it can be found in the literature a few research works as the one of Kapania, Haryadi, and Haftka [81], [82]. In this study, Kapania, Haryadi, and Haftka resorted to the Ritz method to extract the global model displacements and to the finite element method for the local one. They assessed that for circular cut-outs the Ritz method was quite accurate, but not the case for elliptical and stepped cut-outs. However, with the implementation of the global-local scheme an improvement of 31% regarding the elliptical cut-outs displacements was achieved, and 98% for the slopes and moments. The authors also obtained significant computational cost savings from 55% less CPU time and 70% less data storage.

Besides the works referenced above, there are many studies on the application of global-local techniques for delamination prediction or even to simply analyse more accurate and complete stress distributions, commonly for shell global models were the through thickness stress is available and could be of interest [72], [76], [79], [80].

Part III

Numerical Finite Element Model

Chapter 3

Cohesive Zone Model

As previously anticipated, the failure of laminated fibre-reinforced composites may occur due to a variety of intra and interlaminar damage mechanisms , such as delamination, fibre failure and matrix cracking. There are many elements such as loading conditions, geometric-configurations and stacking sequences that can influence the damage mechanisms. Nevertheless, delamination is a dominant form of damage due to the composite intrinsic weakness in interlaminar bonding with high potential to undermine the laminate overall structural integrity. The identification process of delamination initiation and propagation still remains a challenge in this class of materials.

A technique for simulating delamination in finite element software can be classified under the field of Damage Mechanics, specifically through the use of Cohesive Zone Model (CZM). CZM is particularly useful for conducting non-linear progressive failure analyses, including the assessment of ply damage and delamination [31], [83]. As a result, they are the preferred choice for evaluating complex three-dimensional (3D) structures that involve multiple instances of delamination initiation and propagation. Due to their effectiveness in modeling interlaminar damage, CZM have gained widespread popularity.

The Cohesive Zone Model, depicted in Figure 4.1, is a numerical way of representing crack surfaces in quasi-brittle materials. It incorporates a hypothetical fracture line, here referred to as a dashed line, to account for the presence of damage. This fracture line allows for the transfer of cohesive forces between different surfaces, and these cohesive forces are governed by a cohesive law that relates them to the crack opening displacement (CODs). The cohesive law is based on the concept of fracture energy and establishes the relationship between cohesive forces and Crack Open Displacements.

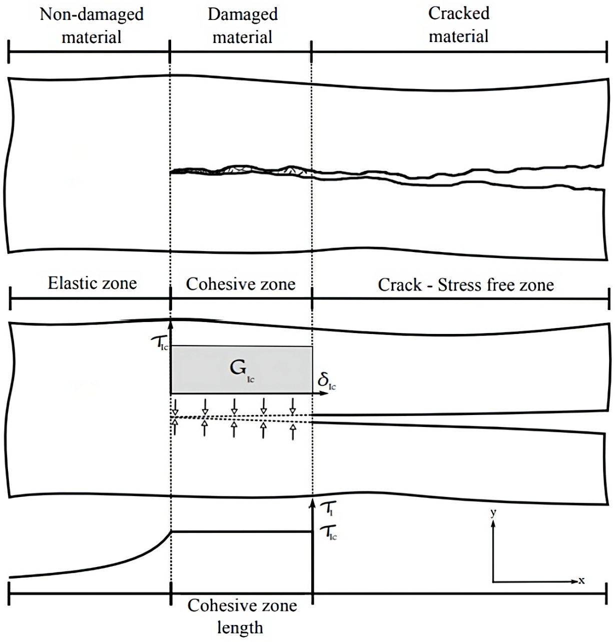

Figure 3.1: Cohesive zone model of the damaged fibre-reinforced polymer. The top figure represents the Fracture Process Zone (FPZ); the middle figure describes the cohesive model concept; the bottom figure shows the stress distribution along the crack zone for a pure mode I loading and a constant cohesive law [84].

Cohesive Zone Model (CZM), as documented in existing literature, rely on a cohesive interfacial law, often referred to as a traction-separation law. This law defines the mechanical relationships between cohesive tractions (σ) and interfacial separations (δ), which have a significant impact on the softening behaviour and the development of the Fracture Process Zone [85]. According to this law, as the separation between interfaces increases, the initially maximum tractions across the interface gradually decrease and eventually vanish when complete decohesion occurs. This results in the total degradation of stiffness and strength [31], [36].

Cohesive zone models offer a valuable means of characterizing both the initiation and propagation of damage, allowing for a comprehensive understanding of the fracture behaviour within a continuum. Analysing a quasi-brittle bar with length L and a cross-section A, Figure 3.2, the cohesive law can be easily comprehended by looking at Equation 3.1, where d represents the damage variable moved by displacement changes. In simple words, the materials ability to carry loads decreases with the increase of damage, which is obtained from d.

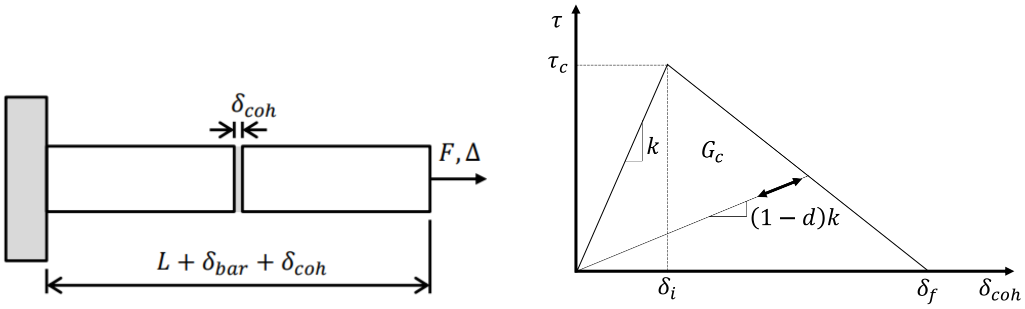

(a) Elastic bar with cohesive crack. (b) Bilinear cohesive law

Figure 3.2: Quasi-brittle bar with a cohesive interface.

$$\boldsymbol{\tau} = \begin{cases} k\delta, & \delta < \delta_i \\ (1-d)k\delta, & \delta_i \le \delta \le \delta_f \end{cases} \tag{3.1}$$

Determining initiation strength, fracture toughness, and shape parameters typically requires experimental characterization. These determinations can vary depending on three opening modes: mode I (normal direction), shear mode II (in-plane direction), mode III (out-of-plane direction), and mixed-mode [85]. However, challenges associated with directly measuring these variables have led researchers to adopt alternative methods like analytical or semi-analytical computations using inverse techniques [86]–[88].

Multiple laws have been proposed to represent interlaminar damage in composite materials. These cohesive laws vary primarily in terms of the criteria they use to determine the initiation and progression of damage under mixed-mode conditions. Additionally, they differ in the assumed idealized shape that governs the progression of damage. Such shapes can range from bi-linear to trapezoidal or exponential profiles. However, it's important to note that even simplified geometries may exhibit limited accuracy [85]. The softening law might exhibit a maximum point at small displacements to account for localized deformation at the fracture tip and a longer decay at larger crack opening displacements to represent the effects of bridging in the region behind the crack.

In order to overcome this issued and better represent this complex behaviour, researcher proposed the use of multi-linear softening laws, which result from the combination of two or more bi-linear cohesive laws, Figure 3.3 [31], [36], [89], [90].

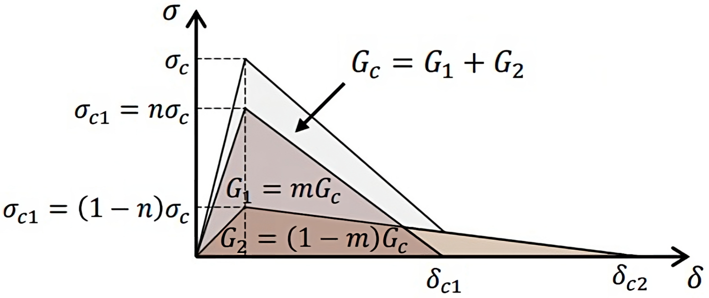

Figure 3.3: Tri-linear cohesive law obtained by combining two bilinear laws [36].

Transposing the aforementioned concepts of CZM to its finite element representation, namely for `Abaqus`, a first look at the physical representation of the concept is essential, Figure 3.4.

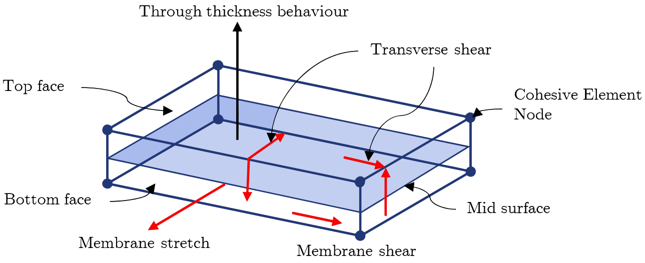

Figure 3.4: Graphical representation of a three-dimensional cohesive element [78].

The transverse shear behaviour of the cohesive element is determined by measuring the relative displacement between the bottom and top faces in a plane perpendicular to the thickness direction. While it is assumed that the cohesive elements do not generate any stresses in a purely membrane response, the stretching and shearing of the mid-surface of the element, located between the bottom and top faces, are associated with membrane strains within the cohesive element [78].

To model bonded interfaces in composite structures, it is recommended to use a traction-separation-based approach. In compliance with this modeling strategy, cohesive elements are used to represent extremely thin adhesive layers, which can be considered to have negligible thickness for practical purposes. These cohesive elements need to be strategically placed in areas where stress concentrations are expected and where cracks may occur.

`Abaqus` implementation of the traction-separation model follows a linear elastic formulation that is followed by delamination initiation and further propagation. The elastic

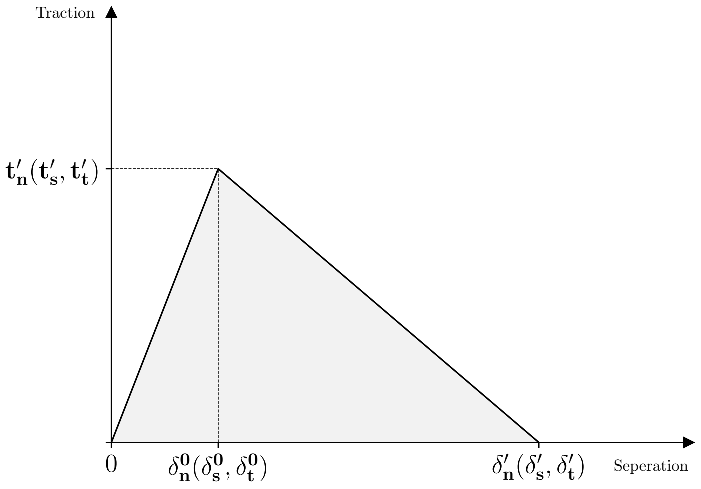
Traction
$\mathbf{t'_n(t'_s, t'_t)}$
0
$\delta^{\mathbf{0}}_{\mathbf{n}}(\delta^{\mathbf{0}}_{\mathbf{s}}, \delta^{\mathbf{0}}_{\mathbf{t}})$
$\delta'_{\mathbf{n}}(\delta'_{\mathbf{s}}, \delta'_{\mathbf{t}})$
Seperation

H

Figure 3.5: Traction separation response [78].

behaviour of such type of elements is defined as in Equation 3.2, with the traction vector t composed by two shear tractions and a normal traction, [78].

$$\mathrm{t} = \begin{Bmatrix} t_n \\ t_s \\ t_t \end{Bmatrix} = \begin{bmatrix} E_{nn} & 0 & 0 \\ 0 & E_{ss} & 0 \\ 0 & 0 & E_{tt} \end{bmatrix} \begin{Bmatrix} \varepsilon_n \\ \varepsilon_s \\ \varepsilon_t \end{Bmatrix} = \mathrm{E}\varepsilon \tag{3.2}$$

The approach for modelling damage in cohesive materials is similar to the framework used for continuum solids. It involves three main components: damage initiation criteria, an evolution law, and the option to delete elements once a defined damaged state is reached. However, it is important to note that modelling damage in traction-separation response has its own unique characteristics that need to be thoroughly studied before conducting the simulation. The initial response for the cohesive element is linear and follows the configuration shown in Figure 3.5.

Maximum and Quadratic Nominal Stress Criteria

There are different damage initiation criteria implemented in `Abaqus`, one of them being the Maximum and Quadratic Nominal Stress Criteria, which is defined by Equation 3.3 and Equation 3.4. For this criteria damage is said to start when the nominal stress ratio reaches the value one.

$$\max\left\{\frac{\langle t_n\rangle}{t_n^o}, \frac{t_s}{t_s^o}, \frac{t_t}{t_t^o}\right\} = 1 \tag{3.3}$$

$$\left\{\frac{\langle t_n\rangle}{t_n^o}\right\}^2 = \left\{\frac{t_s}{t_s^o}\right\}^2 = \left\{\frac{t_t}{t_t^o}\right\}^2 = 1 \tag{3.4}$$

Maximum and Quadratic Nominal Strain Criteria

Another criteria is the Maximum and Quadratic Nominal Strain Criteria which in defined not in stress but in strain, Equation 3.5 and Equation 3.6. The philosophy is the same, and damage occurs when the nominal strain ration is equal to one.

$$\max\left\{\frac{\langle\varepsilon_n\rangle}{\varepsilon_n^o}, \frac{\varepsilon_s}{\varepsilon_s^o}, \frac{\varepsilon_t}{\varepsilon_t^o}\right\} = 1 \tag{3.5}$$

$$\left\{\frac{\langle\varepsilon_n\rangle}{\varepsilon_n^o}\right\}^2 = \left\{\frac{\varepsilon_s}{\varepsilon_s^o}\right\}^2 = \left\{\frac{\varepsilon_t}{\varepsilon_t^o}\right\}^2 = 1 \tag{3.6}$$

In the context of damage evolution, the cohesive law describes how the stiffness of the material deteriorates once the damage initiation criteria are satisfied. The software employs a framework similar to that used for conventional materials, but it offers various options specifically tailored for this aspect of the simulation.

In the traction-separation model, the stress components are affected by the presence of damage, and this influence is determined by these equations:

$$t_n = \begin{cases} (1-D)\overline{t}_n & \overline{t}_n \geq 0 \\ \overline{t}_n & \text{otherwise (no damage compressive stiffness)} \end{cases} \tag{3.7}$$

$$t_s = (1-D)\overline{t}_s \tag{3.8}$$

$$t_t = (1-D)\overline{t}_t \tag{3.9}$$

In these equations D represents the overall damage variable within the adhesive. Initially, D is set to 0 and gradually increases to 1 as the material undergoes additional loading after damage initiation. The symbols $\overline{t}_n$, $\overline{t}_s$, and $\overline{t}_t$ denote the stress components predicted by the elastic traction-separation behaviour based on the current strains, without any damage.

When considering damage under both normal and shear deformation, it's important to emphasize the significance of the effective displacement and equivalent normal strain, as described the following equations [78].

$$\delta_m = \sqrt{\langle\delta_n\rangle^2 + \delta_s^2 + \delta_t^2} \tag{3.10}$$

$$\varepsilon_m = \sqrt{\langle\varepsilon_n\rangle^2 + \varepsilon_s^2 + \varepsilon_t^2} \tag{3.11}$$

Understanding the functionality of the software in the context of mixed mode delamination is crucial. Figure 3.6 visually depicts how damage initiation and evolution are influenced by the mode mixity in a traction-separation response with isotropic shear behaviour, providing a schematic illustration of this relationship. The two horizontal axes represent the magnitudes of shear and normal separation, while the vertical axis represents the traction. The uncovered triangles in the vertical coordinate planes represent the reactions under pure normal and pure shear deformation. Each intermediate vertical plane in the figure represents the damage response under mixed mode settings with different mode mixes.

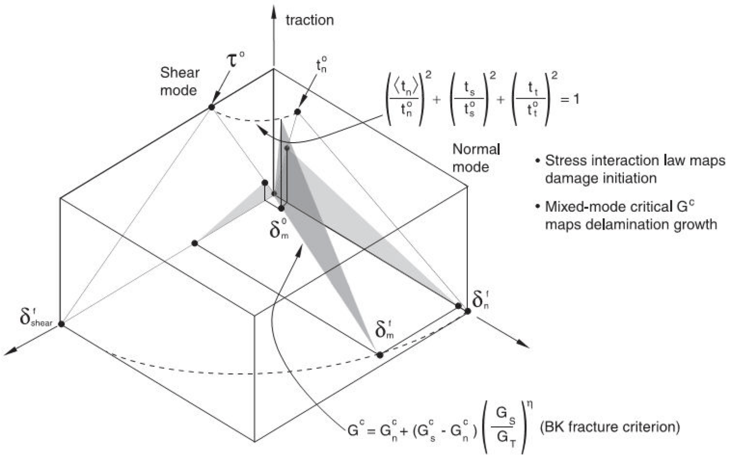
traction
Shear mode
τ^o
t_n^o
$\left(\frac{\langle t_n \rangle}{t_n^o}\right)^2 + \left(\frac{t_s}{t_s^o}\right)^2 + \left(\frac{t_t}{t_t^o}\right)^2 = 1$
Normal mode
• Stress interaction law maps damage initiation
• Mixed-mode critical G^C maps delamination growth
δ_m^o
δ_n^f
δ_{shear}^f
δ_m^f
$G^c = G_n^c + (G_s^c - G_n^c)\left(\frac{G_S}{G_T}\right)^\eta$ (BK fracture criterion)

Figure 3.6: Illustration of mixed-mode response in cohesive elements [78].

`Abaqus` provides a variety of ways to define the damage evolution, offering great flexibility to analysts when performing research work in the field of delamination and cohesive zone modelling. Table 3.1 Table 3.2 summarises the damage evolution laws available and the additional parameters that control those laws, respectively.

Table 3.1: Damage Evolution in Abaqus [78].

	Evolution Law	**Formulation**
Based on Effective Displacement	Linear Damage	$D = \frac{\delta_m^f(\delta_m^{\max} - \delta_m^o)}{\delta_m^{\max}\left(\delta_m^f - \delta_m^o\right)}$
	Exponential Damage	$D = 1 - \left\{\frac{\delta_m^o}{\delta_m^{\max}}\right\}\left\{1 - \frac{1 - \exp\left(-\alpha\left(\frac{\delta_m^{\max} - \delta_m^o}{\delta_m^f - \delta_m^o}\right)\right)}{1 - \exp(-\alpha)}\right\}$
	Tabular Damage	Specify directly the fracture energy as a function of the mode mix in tabular form.
Based on Energy	Power Law Form	$G^C = 1/\left(\left\{\frac{m_1}{G_n^C}\right\}^{\alpha} + \left\{\frac{m_2}{G_s^C}\right\}^{\alpha} + \left\{\frac{m_3}{G_t^C}\right\}^{\alpha}\right)^{1/\alpha}$
	BK Form	$G_n^C + \left(G_s^C - G_n^C\right)\left\{\frac{G_S}{G_T}\right\}^{\eta} = G^C$
	Linear Damage	$D = \frac{\delta_m^f(\delta_m^{\max} - \delta_m^o)}{\delta_m^{\max}\left(\delta_m^f - \delta_m^o\right)}$
	Exponential Damage	$D = \int_{\delta_m^o}^{\delta_m^{\max}} \frac{T_{\text{eff}}\, d\delta}{G^C - G_o}$

Table 3.2: Parameter definition for Damage Evolution [78].

Symbol	**Definition**
$\boldsymbol{\delta_m^0}$	Effective Displacement at damage initiation
$\boldsymbol{\delta_m^f}$	Effective Displacement at failure
$\boldsymbol{\delta_{max}^f}$	Maximum value of the effective displacement during loading history
$\boldsymbol{G_n}$	Work done by the tractions and their conjugate relative displacement in the normal direction
$\boldsymbol{G_s}$	Work done by the tractions and their conjugate relative displacement in the first shear direction
$\boldsymbol{G_t}$	Work done by the tractions and their conjugate relative displacement in the second shear direction
$\boldsymbol{G_T}$	$G_T = G_n + G_s + G_t$
$\boldsymbol{G_T}$	Energy dissipated due to work in the first and second shear directions, $G_S = G_s + G_t$
$\boldsymbol{G^C}$	Energy dissipated due to failure
η	Material Parameter

For the models developed in the present document the evolution laws assumed was the BK law, based on its extensive use in the literature and proved to be accurate and efficient alongside the Quadratic Stress Nominal Criteria.

Encompassing this whole formulations, `Abaqus` provides a series of different cohesive elements, namely the `COH3D6`, `COH3D8`, `COH3D6P` and the `COH3D8P` elements. The elements used throughout this work will be the `COH3D8`, which is a 8-node three-dimensional cohesive element, that based on the literature can provide accurate delamination representation.

Chapter 4

Open-hole tensile test model

4.1 Scope of the model

The proposed work is to develop a global-local analysis of a civil aircraft composite wing-box to assess free-edge delamination in an inspection hole on the lower skin. However, since there is no experimental data regarding the wing-box model used, another model had to be developed to validate the cohesive zone model approach as well as the global-local technique.

4.2 Specimen Configuration

The model considered to perform the validation of the method is an open-hole tensile test of a composite specimen, since its geometry resembles the one of the wing-box with an inspection hole that will be analysed later.

The specimen configuration chosen was the same as presented by Green, Wisnom, and Hallett [91], Figure 4.1.

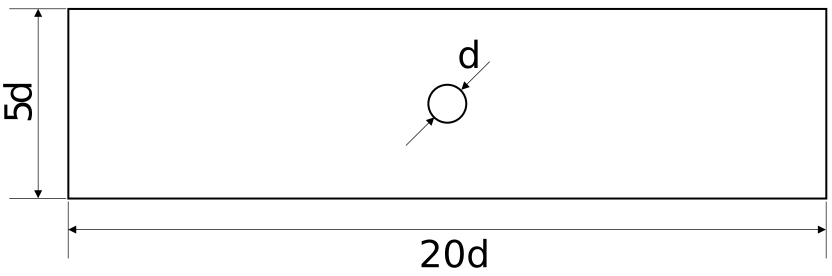

Figure 4.1: Open-hole specimen dimensions

The coupons manufactured in Green *et al.* [91] were IM7/8552 unidirectional carbon-fibre/epoxy pre-pregs with a nominal thickness of 0.125mm. The layup used was $[45_m/90_m/-45_m/0_m]_{ns}$, with 0° being the load direction, leading to a quasi-isotropic laminate. The tensile test was performed for a variety of specimens with hole diameters ranging from 3.175mm to 25.4mm and different combinations of m, n and ply thickness. Table 4.1 sums up the specimens configurations that failed by delamination.

Table 4.1: Failure stresses [MPa], (variation, %), for open hole tension of $[45_m/90_m/-45_m/0_m]_{ns}$ laminates failed by delamination [91].

No. of blocked plies, m	No. sub-laminates, n	T_{ply} [mm]	T [mm]	Hole diameter [mm]			
				3.175	6.35	12.4	25.4
2	1	2	0.25	396 (5.2)	-	-	-
4	1	4	0.5	275 (5.6)	285 (5.2)	362 (2.6)	417 (4.1)
8	1	8	1.0	202 (7.9)	-	-	232 (1.9)

For the simulations shown in the next sections only the specimen with $m = 4$, $n = 1$, a hole diameter of 3.175mm and a total ply thickness of 4mm was considered.

4.2.1 Material Properties

The material at hand, as mentioned before, is the IM7/8552. The properties for this material were retrieved from [92] and are shown in Table 4.2.

Table 4.2: IM7/8552 properties [92].

E_1	$E_2 = E_3$	$G_{12} = G_{13}$	G_{23}	$\nu_{12} = \nu_{13}$	ν_{23}
161 GPa	11.4 GPa	5.17 GPa	3.98 GPa	0.32	0.436
X_t	X_c	Y_t	Y_c	$S_{12} = S_{13}$	ρ
2806 MPa	1690 MPa	60 MPa	185 MPa	90 MPa	1.58 g/cm^3
G^t_{fc}	G^c_{fc} [93]	G_{nc} [94]	G_{sc} [94]		
112.7 kJ/m^2	25.9 kJ/m^2	0.2 kJ/m^2	1.0 kJ/m^2		

Since the objective of the simulation is to predict delamination, a cohesive section will be defined in-between plies. The properties used for the interface cohesive elements are the ones presented in Table 4.3.

Table 4.3: Cohesive properties.

K_n	τ_n	τ_{sh}	G_{IC}	G_{IIC}	η	ρ
$3 \cdot 10^5$ N/mm^3	30 MPa	50 MPa	0.2 kJ/m^2	0.5 kJ/m^2	1.45	1.58 g/cm^3

Chapter 5

OHT reference model

In this chapter, two different finite element models with a 3D formulation, that were setup to be used as a reference to the global-local results, will be discussed. These two models apply different composite damage model, namely the Hashin model [40] implemented in `Abaqus` and an interlaminar damage model presented in [95] and [96], via a user defined subroutine.

All the simulations were performed using an Intel Xeon E5-2659 v4 cpu with 24 cores, from which only 12 were used.

5.1 OHT with Hashin Damage Model

The following subsections will highlight and discuss the finite element model, of the open-hole tensile test with Hashin damage, details and settings.

5.1.1 Geometry and Material definition

The material definition follows the configuration aforementioned, with a $[45_4/90_4/-45_4/0_4]_s$ layup, 0.125mm ply thickness and the material properties of Table 4.2 and Table 4.3. The cohesive layers were considered to have 0.001mm of thickness, with a quadratic stress based damage initiation criterion and a bilinear damage evolution law. The mode mixity-was instead regulated with the BK law [58].

The geometry was first designed as parallelepiped block with the dimensions specified in Figure 4.1 including the hole, which then was sliced using partition planes to obtain the discretized plies and cohesive layers. In this discretization, the blocked plies, i.e., the consecutive ones with the same fibre orientation, were considered as a single partition, since in theory there is no mismatch in ply properties and therefore that should not be a critical interface for delamination, which allowed to not include the cohesive layers in-between those plies and making the model less computational expensive. With this approach it was possible to model the specimen in a single part avoiding the definition of additional interactions in an assembly.

5.1.2 Boundary Conditions

To achieve uniaxial tension in the simulation the boundary conditions must be carefully applied in order to avoid unwanted stress concentrations at those locations, which may result in inaccurate results.

The specimen was constrained as in Figure 5.1:

- the left most faces (red pattern) were constrained in the load direction (x), U1=0.
- the bottom left and right edges (purple edges) were constrained in the specimen transversal direction (y), U2=0.
- the two vertical edges in the left and right of the specimen (yellow edges) were constrained in the out-of-plane direction (z), U3=0

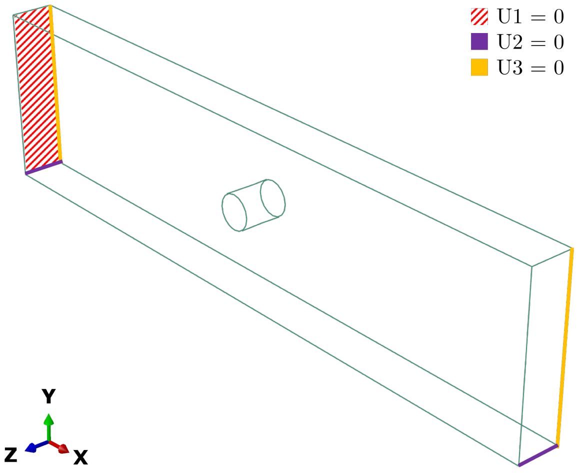

Figure 5.1: Open-hole reference model boundary conditions.

5.1.3 Load

The displacement was applied using a reference point and the interaction type `Equation` provided by `Abaqus`, which is a linear multi-point constraint requiring a linear combination of nodal variables equal to zero:

$$A_1 u_i^P + A_2 u_j^Q + \ldots + A_N u_k^R = 0 \tag{5.1}$$

with u_i^P being the displacement at a node P for the degree of freedom i, while A_n are the coefficients defining the relative motion of the nodes [78].

Having the reference point and the right most face of the specimen properly linked by the `Equation` interaction, a prescribed displacement of 2.5% of the specimen's length imposed in the x direction, Figure 5.2.

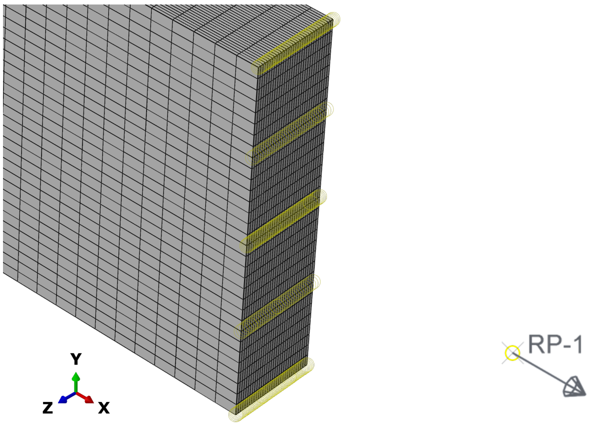

Figure 5.2: Open-hole reference model interaction and prescribed displacement.

5.1.4 Mesh

`Abaqus` only supports the Hashin damage model for shell elements, so for this reason 3D elements could not be used and continuum shell ones were employed, namely the `SC8R`. Briefly, the `SC8R` continuum element has an 8 noded hexahedron configuration and accounts for thickness changes, finite membrane strains and large rotations which are desirable for large-strain analysis [78]. For the cohesive layers the elements used were the `COH3D8`.

The mesh as represented in Figure 5.3 was divided in two sections that separate the zone close the whole and the rest of the specimen. In the zone of the hole, a finer mesh was created to better capture the stress concentration effect caused by that geometrical discontinuity with the element size decreasing from 0.5mm to 0.1mm along the radial direction. The coarser part of the mesh has 0.5mm by 1mm element size.

The final mesh resulted having had a total of 284544 elements. The element deletion option was activated for this analysis. Although a mesh convergence study is not shown in this work, it is important to highlight that it should have been performed to ensure the a more complete model development.

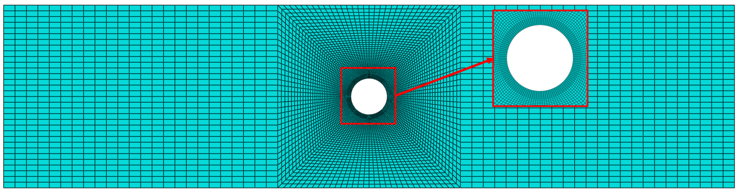

Figure 5.3: Open-hole reference model mesh.

5.1.5 Step

Since a tensile test is performed in a quasi-static static state, a suitable simulation type must be used. Initially a Dynamic Implicit approach with a step time of 190.5s, which in relation to the applied displacement translates to a loading rate of 0.5mm/min as in the tests performed by Green, Wisnom, and Hallett [91], was adopted. The quasi-static application procedure provided by `Abaqus` was also used and the non-linear geometric effects were considered. However, the model was having convergence issues and was computationally heavy.

To overcome this drawback the simulation was switched to a Dynamic Explicit one, that for highly nonlinear cases perform better than the implicit integration counterpart. When defining a quasi-static simulation with an explicit solver special care has to be taken into account to avoid the introduction of inertial effects. So to avoid a high speed deformation wave, an eigenmodes analysis of the specimen was conducted to determine its natural frequency, which was 2192.3Hz, giving a natural period of approximately $4.56 \cdot 10^{-4}$s. The step was then taken as three times this value, 0.0014s.

The core of explicit integration schemes relies in very small time steps which leads to a large increment number. If the total step time is too high the number of increments may become excessive and simulation time may not be feasible. Yet there is an interesting feature of explicit integration schemes known as mass scaling, which virtually increases the systems mass to allow for a large time increment and therefore reducing the simulation time. Still, careful consideration of the parameters involved in its definition must be taken, with the most important measure to look at being the minimum stable time increment which is directly correlated to the minimum element size and the material density.

For the present model the `Semi-automatic mass scaling` option of `Abaqus` was defined with a target time increment of $3 \cdot 10^{-8}$s at every increment for the whole model.

Kinetic and total internal energies of the model where monitored along the simulation to ensure that the kinetic energy can be considered close to zero when compared to total internal one, meaning that there are no kinetic effects and the simulation is performed in a quasi-static manner.

5.1.6 Results

Considering the finite element model just described, the simulation ran all the way through with a total simulation time of 2127s, that is approximately 35.5min.

First of all, the energies as previously mentioned should be checked and as depicted in Figure 5.4, the internal energy is much higher than the kinetic one and the latter can be assumed as close to zero, thus quasi-static state was achieved.

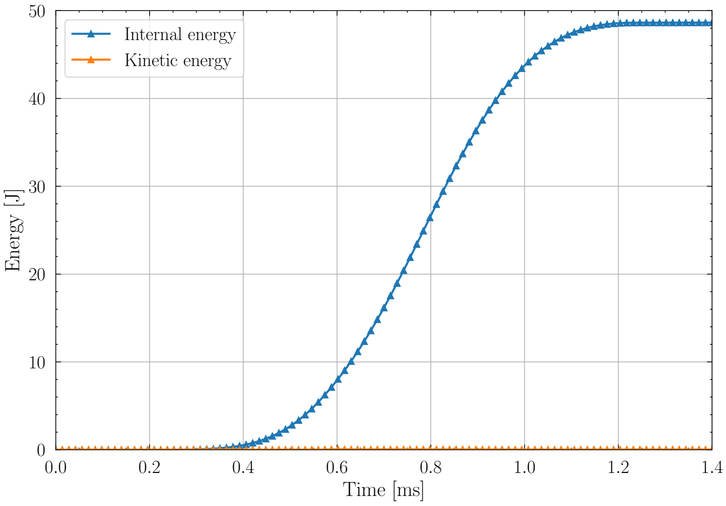

Figure 5.4: Energies for the open-hole reference model with Hashin damage.

To assess the validity of the model, the stress-strain curve can be plotted to determine the failure stress to be compared with the reference one from Table 4.1.

The stress-strain curve shown in Figure 5.6 was obtained from the the reaction forces, read at the reference point were the displacement was applied, divided by the cross sectional area of the specimen and the displacement at the reference point divided by the specimen's length.

The expected load-displacement curve shape, and consequently the stress-strain curve shape, is one similar to Figure 5.5.

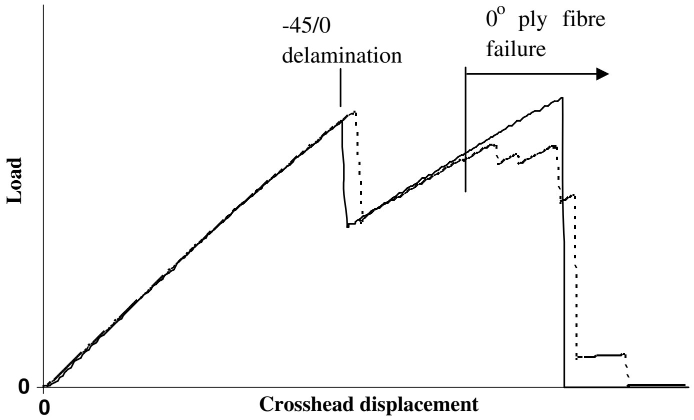

Figure 5.5: Typical load-displacement curve for specimens failing by delamination [91].

However, the obtained curve, Figure 5.6, is far from being similar to the experimental one. This can be attributed to the lack of interlaminar damage behaviour in the Hashin damage model, which only assumes intralaminar damage.

Nonetheless, for the sake of comparison the failure stress value was considered to be the one at the "break" of the curve were a slight change in stiffness may have occurred, as done by Wisnom [53], having a value of 421.84 MPa. This value relative to the reference of 275 MPa presents an error of 53.4%.

Such big difference may be explained by the limitations of the 2D Hashin damage model. Although it accounts for four different intralaminar damage mechanisms, namely fibre and matrix tension and compression, the 2D formulation of this model is limited to plane stress-states due to lack of the effects caused by the out-of-plane stress making it not adequate for strong three dimensional stress state. Besides that, the out-of-plane stress is known to present considerably high values at certain regions, such as free edges, which can be of great impact in the delamination behaviour captured by the cohesive elements. The 2D Hashin damage criterion determines the element deletion accordingly to the damage variable within its formulation, which means that when this variable reaches the critical value the elements are deleted regardless of excessive element distortion failure and that it lacks an important feature of its 3D counterpart which is the inclusion of the maximum and minimum principal strains as an additional deletion criteria to prevent the influence of element distortion. This can be a limitation and source for disparity between numerical and experimental values, but for the present case this may not be the issue, since this would imply a lower ultimate strength.

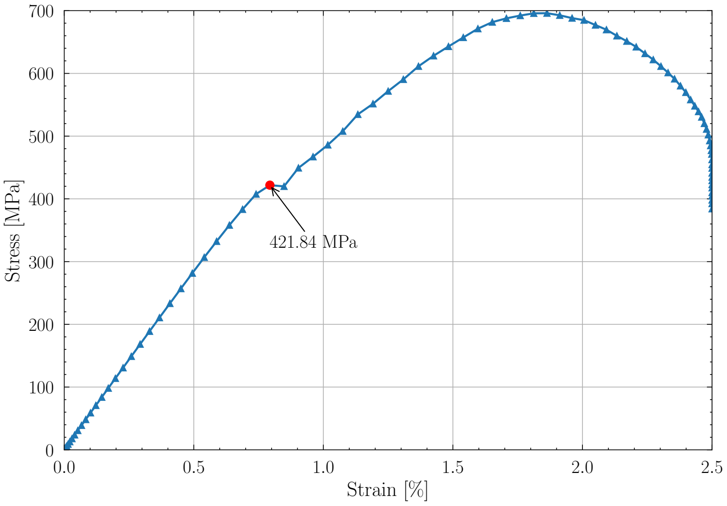

Figure 5.6: Stress-Strain curve for OHT with Hashin damage.

The delamination contours for the three different interfaces, taken at the time step where the failure stress was considered can be seen in Figure 5.7. Analysing these contours another indicator of the erroneous results may be observed. From the literature, the specimen configuration at hand fails by delamination at the -45/0 interface [53], [91]. While the interfaces showing the most degraded cohesive elements are the 90/-45 and 45/90 ones.

The -45/0 interface shows a "peanut shape like" pattern that is common to delamination in open-hole tensile tests, but for the 90/-45 interfaces this pattern is not observed. Unwanted free edge effects, especially regarding out-of-plane stress, coming from the outer edges of the specimen may be a reason for such pattern at the 90/-45 interface and also at the 45/90 one. Looking at the out-of-plane stress for the two interfaces exhibiting the largest delamination areas at the outer edges of the specimen, Figure 5.8 and Figure 5.9, it can be observed that there are stress concentrations close to those edges, at the 45/90 and 90/-45 interfaces, about the same magnitude of the ones present close to the hole for the σ_{13}] and σ_{23}] stresses. The -45/0 interface stress contours do not present such results, thus its delamination pattern is not influenced by the effects described. For the plies suffering from the outer edges influence, this indicates that the free edge effects in those areas are almost equivalent in terms of effect on the overall specimen interface which attenuates the stress concentration caused by the hole, therefore altering the delamination pattern. Adding buffer zones to the edges inducing the unwanted effect could have been a solution but their implementation showed no effect.

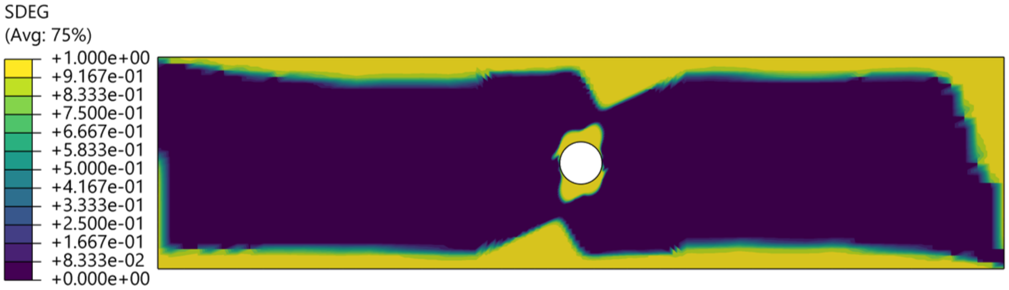

(a) 45° /90° interface.

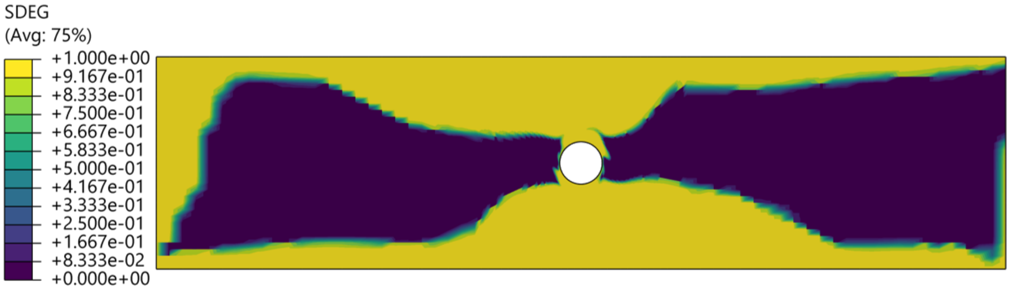

(b) 90° / − 45° interface.

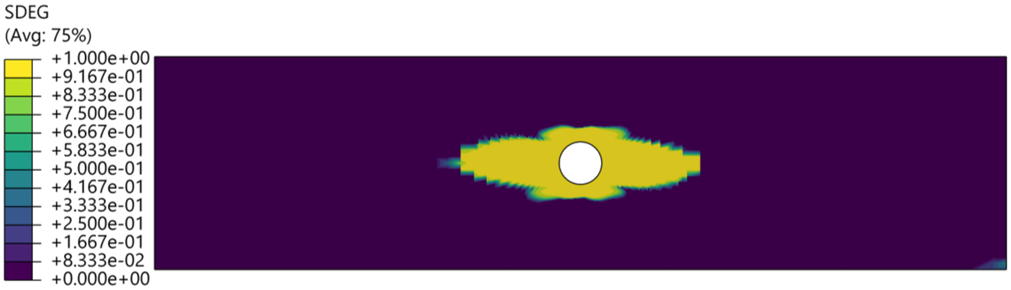

(c) −45° /0° interface.

Figure 5.7: Stiffness degradation of the cohesive interfaces for the open-hole with Hashin damage model, at the assumed point of failure. Contour plotted on undeformed shape.

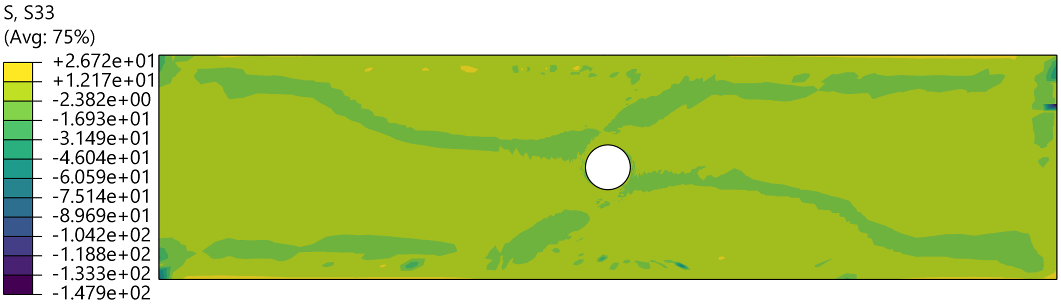

(a) σ_{33} [MPa]

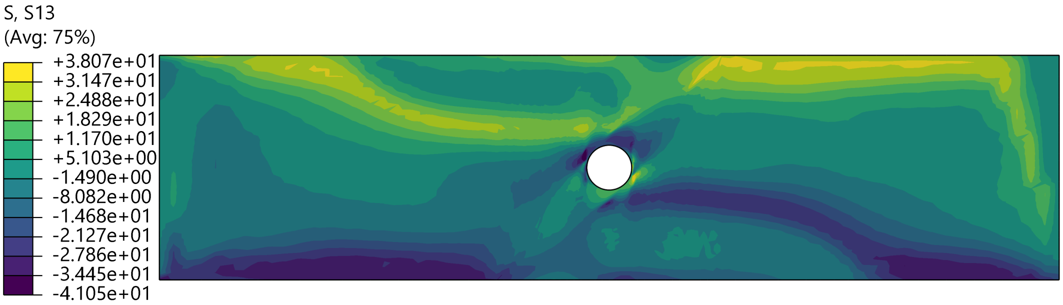

(b) σ_{13} [MPa]

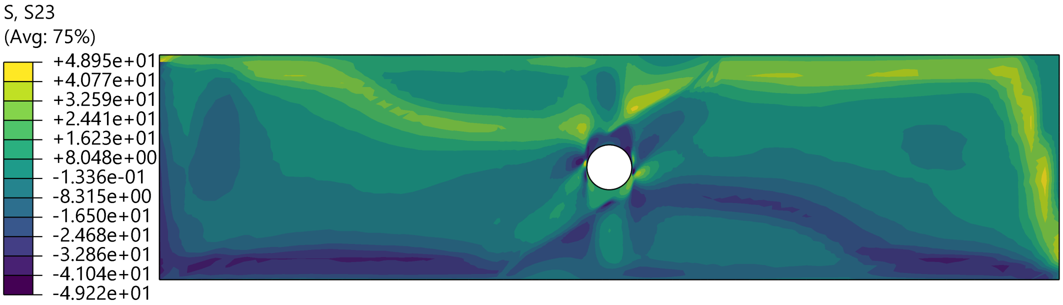

(c) σ_{23} [MPa]

Figure 5.8: Out-of-plane stresses for the interface 45°/90° at the assumed point of failure. Contour plotted on undeformed shape.

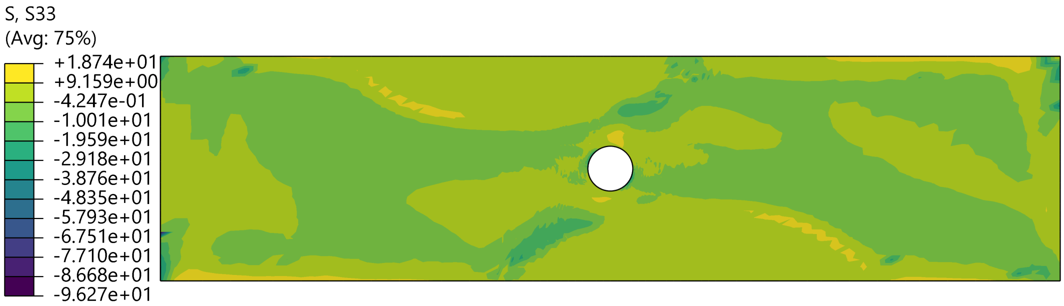

(a) σ_{33} [MPa]

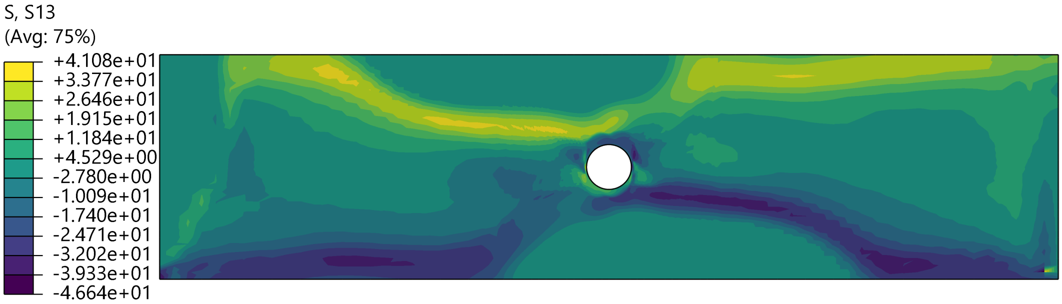

(b) σ_{13} [MPa]

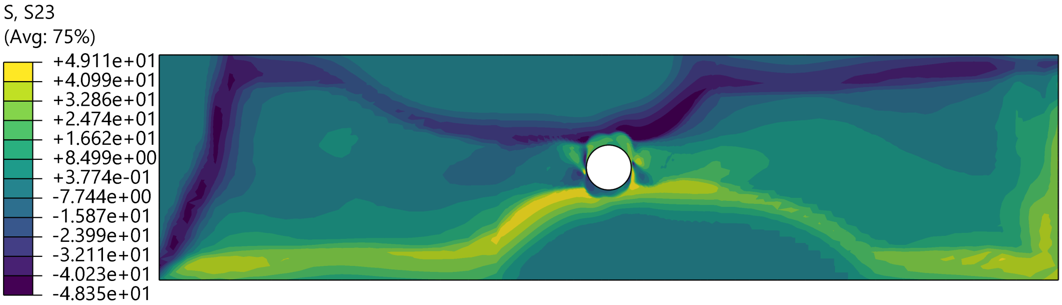

(c) σ_{23} [MPa]

Figure 5.9: Out-of-plane stresses for the interface $90^\circ/-45^\circ$ at the assumed point of failure. Contour plotted on undeformed shape.

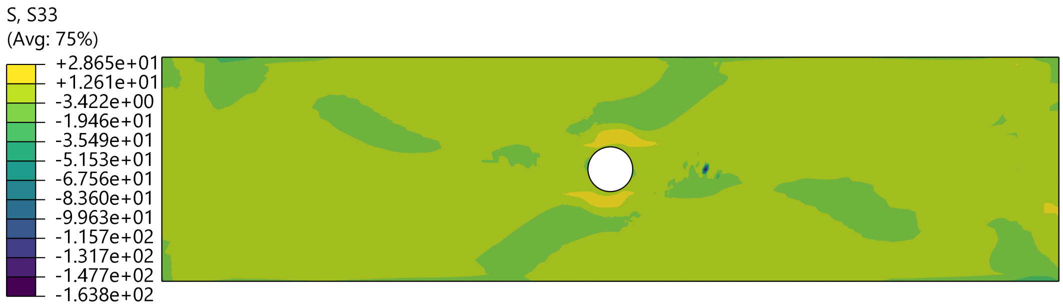

(a) σ_{33} [MPa]

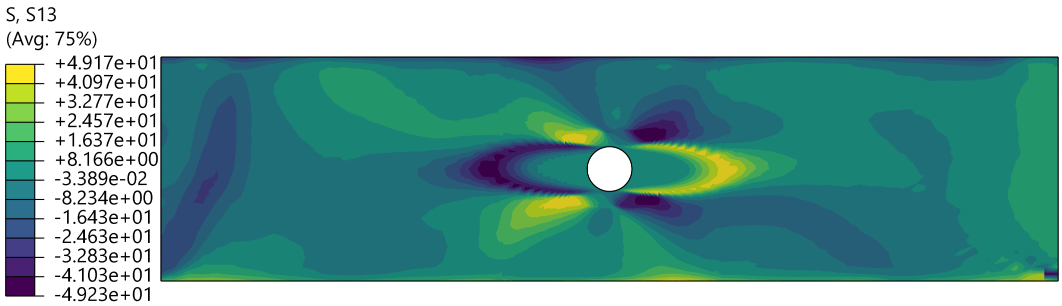

(b) σ_{13} [MPa]

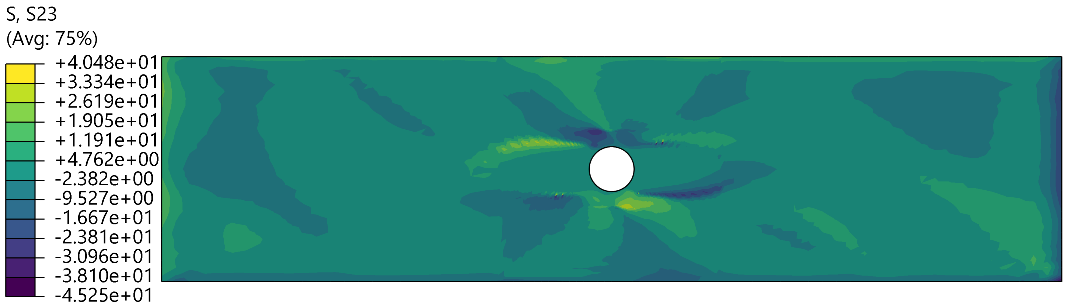

(c) σ_{23} [MPa]

Figure 5.10: Out-of-plane stresses for the interface −45°/0° at the assumed point of failure. Contour plotted on undeformed shape.

5.2 OHT with Intra and Interlaminar damage via VUMAT

The second open-hole reference model was a similar one to the that of the previous section, but instead of recurring to the built-in intralaminar Hashin damage model an intra and interlaminar user defined subroutine written in `Fortran`, known in the finite element analysis field as a `VUMAT`, was utilised.

The following sections will outline a summary of the interlaminar model considered, the modifications with respect to the previous finite element model and ending with a analysis and discussion of the results.

5.2.1 Interlaminar damage model

This user defined material model is based on and interlaminar damage model proposed by Turon, Camanho, Costa, *et al.* [95] and was written by González, Maimí, Turon, *et* *al.* [96] and enhanced with an intralaminar damage model. The material model has a 3D formulation for explicit finite element analysis where the cohesive elements simulate the onset and propagation of delamination for composite materials. The model follows a thermodynamically consistent framework that account for mixed-mode loading conditions [96].

The delamination model follows a similar continuum damage formulation to the ones of Mazars [97] and Simo and Ju [98] with the constitutive equation defined as in Equation 5.2 in a displacement driven manner, were D_{ij} is the undamaged stiffness tensor, $\mathbf{\Delta}_i$ are free variables of the system and d is a variable to ensure that model is irreversible.

$$\tau_i = \frac{\partial \Psi}{\partial \mathbf{\Delta_i}} = (1-d)D^0_{ij}\mathbf{\Delta_j} - dD^0_{ij}\delta_{3j}\langle -\mathbf{\Delta_3}\rangle \quad i,j = 1,2,3 \tag{5.2}$$

The mode-mixity is governed by the BK law [58], that yields to Equation 5.3:

$$\mathbf{\Delta}^f = \frac{\mathbf{\Delta}^o_3\mathbf{\Delta}^f_3 + \left(\mathbf{\Delta}^o_{shear}\mathbf{\Delta}^f_{shear} - \mathbf{\Delta}^o_3\mathbf{\Delta}^f_3\right)\beta^\eta}{\mathbf{\Delta}^0} \tag{5.3}$$

With $\mathbf{\Delta}^o_3$ and $\mathbf{\Delta}^o_{shear}$ being the relative displacements for damage onset in pure Mode I and shear mode respectively and $\mathbf{\Delta}^f_3$ and $\mathbf{\Delta}^f_{shear}$ the damage propagation counterpart.

The damage onset criterion is the same as the one for damage propagation, which differs from the usual stress-based formulations for cohesive damage, since it is based on energy terms [96]. The final equation, in terms of displacement, yields:

$$\mathbf{\Delta}^o = \left(\left(\mathbf{\Delta}^o_3\right)^2 + \left(\left(\mathbf{\Delta}^o_{shear}\right)^2 - \left(\mathbf{\Delta}^o_3\right)^2\right)\beta^\eta\right)^{\frac{1}{2}} \tag{5.4}$$

This cohesive model is for zero-thickness elements so it had to be adapted to accommodate non-zero-thickness elements, i.e., for continuum elements the input data is in the form of a strain tensor instead of relative displacements. The detailed mathematical formulation of the model and subsequent modification for non-zero thickness element is thoroughly described in González, Maimí, Turon, *et al.* [96].

5.2.2 Geometry and material definition

Initally, this model equal to the one with the Hashin damage model, except for the composite material definition that was defined as a user material to make us of the subroutine (VUMAT). After running some simulations and tuning parameters, the model was unstable and was aborting due to excessive element distortion caused by erroneous wave propagation.

At this point, a change in the model definition was performed. Instead of modelling the specimen as a single sliced part, each ply and cohesive layer, including the ones between plies with the same fibre orientation, were modelled separately and joined together using general contact interaction with a frictionless and `hard contact` definition.

Apart from that, all the dimensions and material properties were maintained. The damage initiation criteria was also the quadratic nominal stress with bilinear damage evolution.

5.2.3 Boundary Conditions

The boundary conditions were the same as the ones presented in Figure 5.1.

5.2.4 Load

The load application was switched from an imposed displacement to an imposed velocity set to 1052.63mm/s, which is way higher than the 0.5mm/min performed in the experimental test by Green, Wisnom, and Hallett [91], but explicit analysis, as already mentioned, cannot accommodate large step times in order for the simulation to be executed in a reasonable computational time. The smooth amplitude application of the velocity was also considered in the same fashion as for the previous model.

5.2.5 Mesh

The mesh for the current model was done using the same elements as before, namely the `C3D8I` for the plies and the `COH3D8` for the cohesive layers, but this time the global element size was set to be of 0.5mm resulting in the discretisation in Figure 5.11.

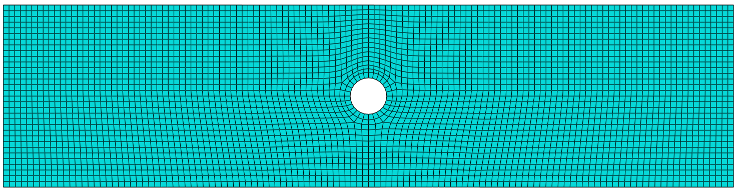

Figure 5.11: Open-hole reference model with VUMAT mesh.

5.2.6 Step

The step definitions used were similar to the one of the previously discussed model without the mass scaling option, since the simulation time was lower and reasonably acceptable and with a smaller step time of 0.0005s, because at the development stage it was observed that the specimen failing before half of the 0.00014s step time and there was no point on performing the simulation in the same time frame. Alternatively the applied velocity could be reduced and step time maintained.

Additionally, two different models were simulated were the first had the default settings when creating the model in the `Abaqus` GUI also element deletion activated, and the second one with the same settings and also the `NLGEOM` option.

5.2.7 Results

The simulation times for the three open-hole models with the damage model embedded in the the material definition via VUMAT are presented in Table 5.1, with the model were non-linear effects were active having a significantly higher simulation time as expected when using this option.

Table 5.1: Simulation times for the open-hole model with the VUMAT.

Model	Time [min]
Element deletion	26.43
Element deletion and NLGEOM	77.58

Looking at the energies plot, Figure 5.12 it can be seen that the conditions for a quasi-static simulation with the explicit analysis was achieved, with the kinetic energy being much lower than the internal one and nearly zero in comparison. The energies of the model with with the NLGEOM option presents some oscillations at the end, that only appeared after the specimen's failure, and therefore can be ignored.

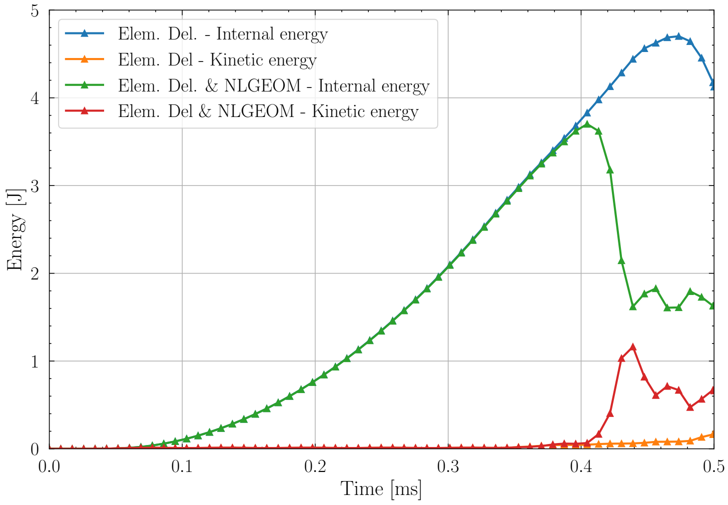

Figure 5.12: Energies for the open-hole reference models with VUMAT.

Moving into the stress-strain curves, shown in Figure 5.13, the shape is similar to the one presented in Figure 5.5 up to the first load drop. These curves do not present the reload behaviour that has been seen in the reference shape due to the specimen failing catastrophically at the end, due to excessive element distortion.

Regarding the failure stress value, a plateau region is clearly observed in the graphs before an accentuated drop in the curve. This plateau region was considered to be the one were failure is due and thus the failure stress in approximately 285 MPa, which relative to the reference (275 MPa) only differs 3.64%. In comparison with the model with the

2D Hashin damage, this presents a much better correlation with experimental data, regarding the failure stress, due to a 3D formulation being present, i.e., a formulation that account for the out-of-plane stresses in the plies which play a major role in delamination behaviour. Also the different material damage models included in the VUMAT, that resort to a different formulation than the ones provided `Abaqus`, may have provided a better capturing of other failure modes than delamination, which affect the out-of-planes stresses.

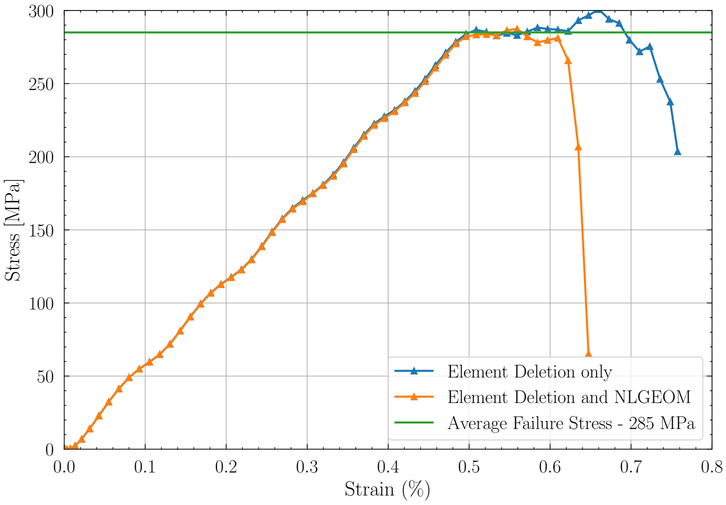

Figure 5.13: Stress-Strain curves for full 3D OHT model with intra and interlaminar damage VUMAT.

From the analysis of the curves, both the energies and stress-strain ones, it can be inferred that the `NLGEOM` doesn't present an apparent advantage, hence either the default settings model or the one with element deletion may be used, since computational cost is smaller. However, the results from the model with `NLGEOM` are slightly different in terms of deformed shape as the following results will show.

Figure 5.14 and Figure 5.15 show the stiffness degradation state at the three cohesive interfaces for both models with the VUMAT taken at the time step where the failure stress of 285 MPa is reached. For the model with element deletion only the most degraded interface is the 90/-45 on which, does not correlate with the data from the literature that as already mentioned states the -45/0 as the critical one. For the other model, the delamination shape changes a bit and the results got closer to the experimental ones. The 90/-45 interface now is not the most singularly the most degraded one, but also the -45/0 interface shows a very degraded state and its contour is also closer to the ones found in the literature, as observed when comparing Figure 5.16 and Figure 5.17.

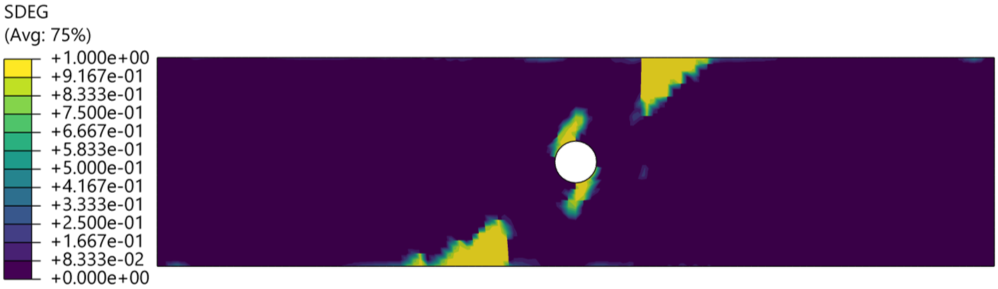

(a) 45°/90° interface.

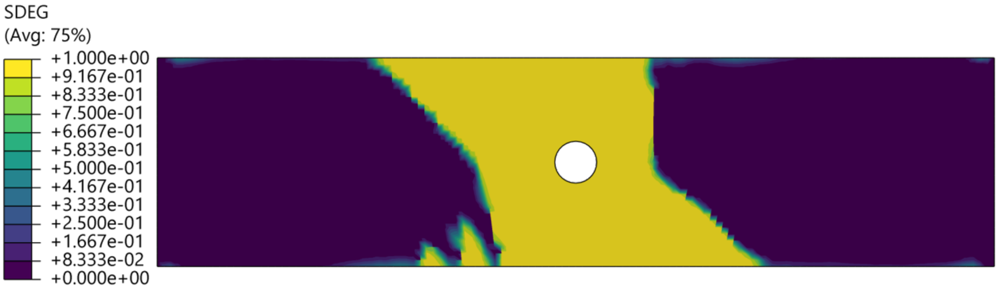

(b) 90°/ − 45° interface.

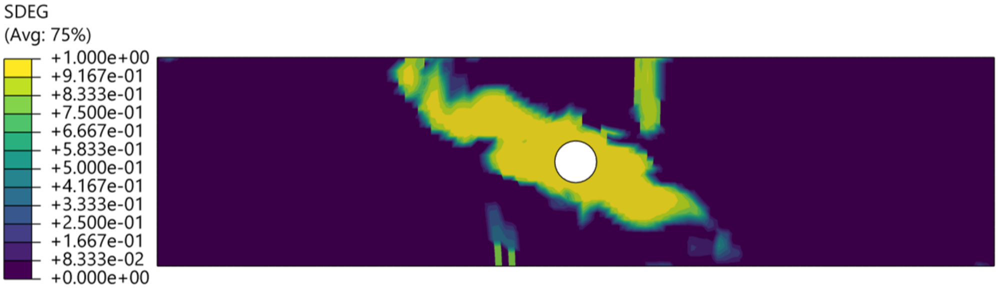

(c) −45°/0° interface.

Figure 5.14: Stiffness degradation of the cohesive interfaces for the open-hole with VUMAT and element deletion. Contour plotted on undeformed shape.

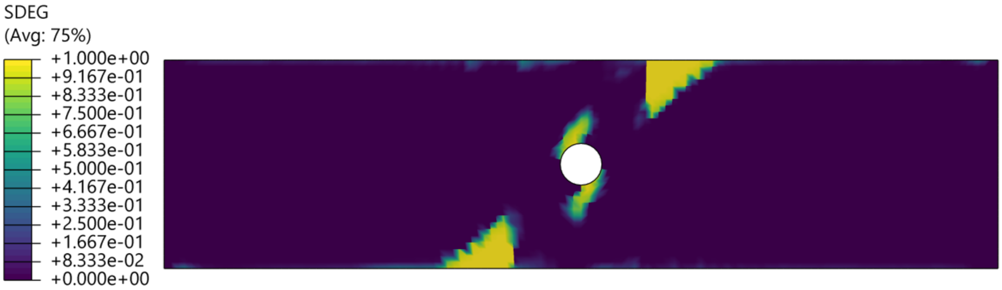

(a) 45°/90° interface.

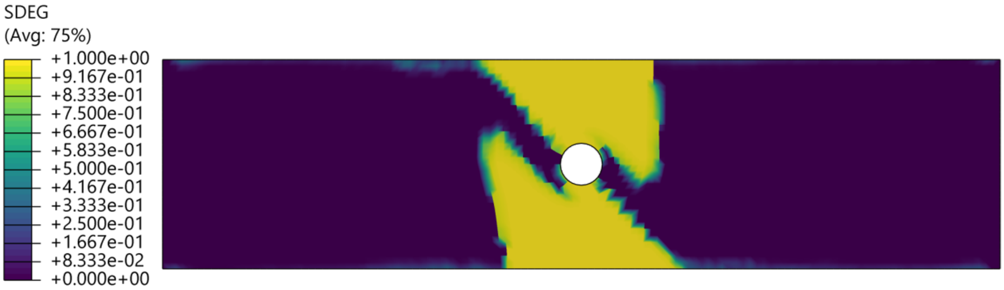

(b) 90°/ – 45° interface.

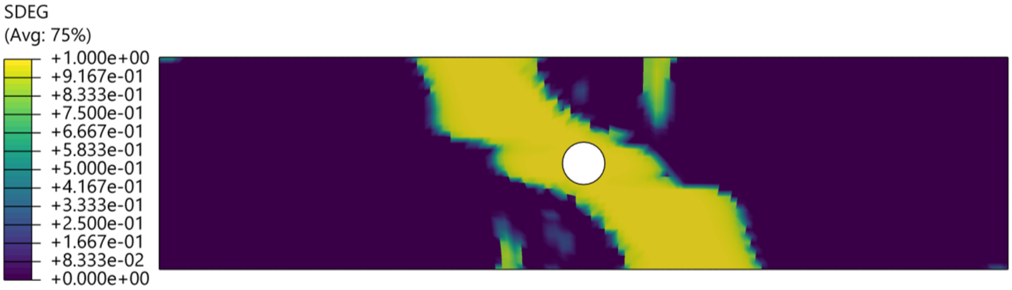

(c) −45°/0° interface.

Figure 5.15: Stiffness degradation of the cohesive interfaces for the open-hole with VUMAT and NLGEOM on. Contour plotted on undeformed shape.

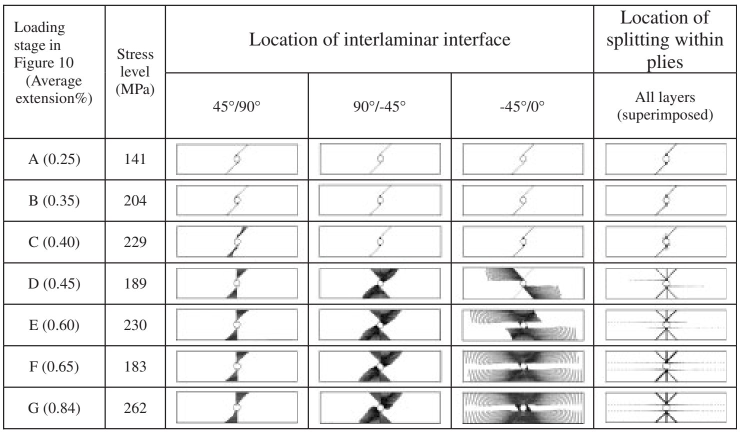

Loading stage in Figure 10 (Average extension%)	Stress level (MPa)	Location of interlaminar interface			Location of splitting within plies
		45°/90°	90°/-45°	-45°/0°	All layers (superimposed)
A (0.25)	141				
B (0.35)	204				
C (0.40)	229				
D (0.45)	189				
E (0.60)	230				
F (0.65)	183				
G (0.84)	262				

Figure 5.16: Typical delamination and splitting progress from FEM [99].

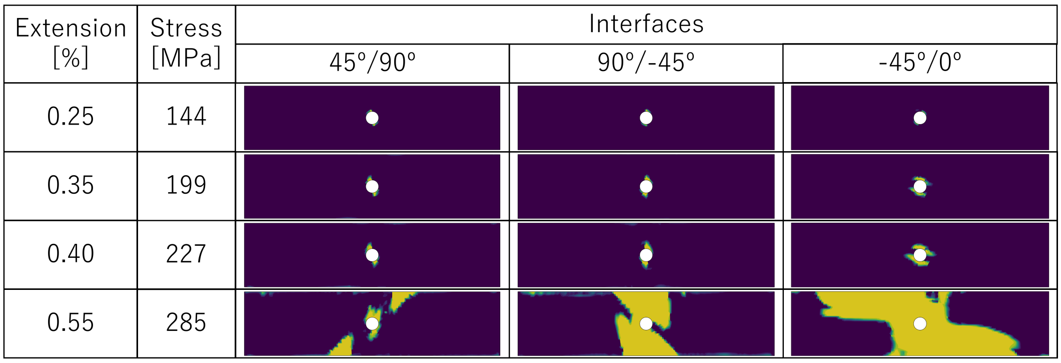

Figure 5.17: Delamination evolution for the OHT with VUMAT and NLGEOM.

Chapter 6

OHT global-Local model

In this chapter, a global-local model of the open-hole specimen aforementioned will be described along with the results and insights obtained. For the present case a global shell model will drive a solid local model.

6.1 Global Model

The global model of then open-hole specimen was formulated as fully linear elastic 2D model with a mesh of 5600 `S4R` shell elements, Figure 6.1, once only the displacement field was of interest to drive the local model. The material was once again the IM7/8552 and the same properties of Table 4.2 were used. The ply stacking was achieved using `Abaqus` composite layup tool.

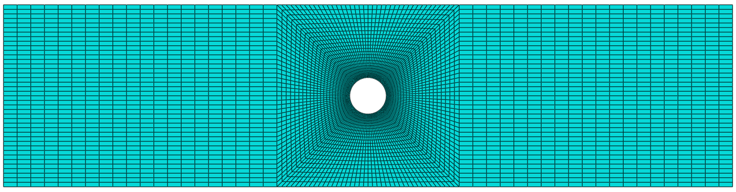

Figure 6.1: Open-hole global model mesh.

Regarding the boundary conditions, to obtain an uniaxial tension state the same philosophy of Figure 5.1 was adopted and adapted to the 2D formulation. Instead of constraining faces and edges, lines and vertices were constrained, respectively. The load application was also via a prescribed displacement following a smooth amplitude curve.

The step was a Static General one with the step time of the same 190.5s that combined with the 1.5785mm displacement gives the reference's 0.5mm/min load rate.

An important detail when performing global-local analysis is to write the global model data with minimal round-off errors, thus the output precision when submitting the `Abaqus` job was set to `full`.

6.1.1 Results

Since the model is purely linear, the simulation took only 3.7s. The displacements in the load direction (U1) and the transversal direction (U2) can be seen in Figure 6.2.The out-of-plane displacement field is not represented since it is approximately null.

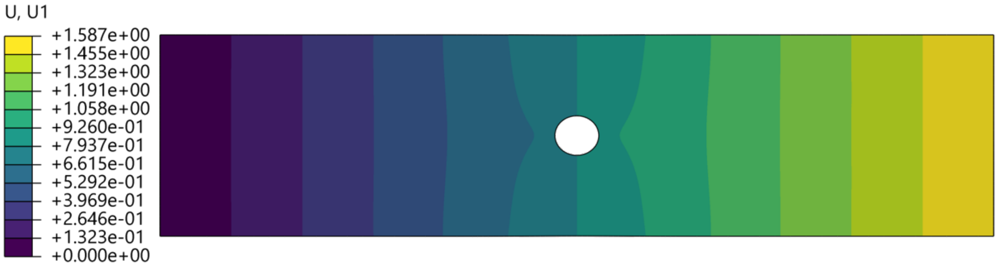

(a) Displacement U1 (x axis).

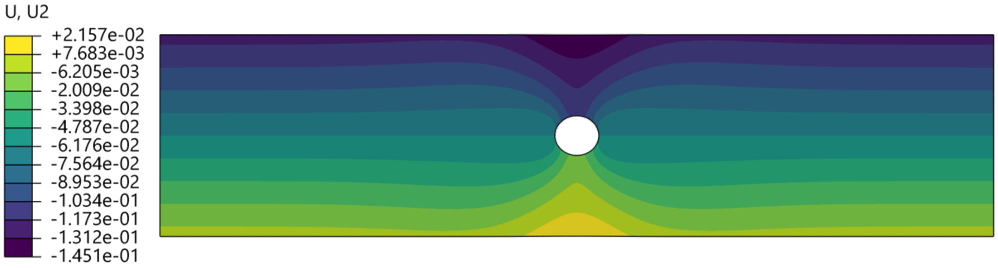

(b) Predicament U2 (y axis).

Figure 6.2: Open-hole global model displacement field in [mm], scale factor of 1.

6.2 Local model

The local model of the open hole was taken has a square, whose dimensions were the same as the specimen's width, and centred at the hole, Figure 6.3. The ply and cohesive layers discretization was performed in a similar manner to the one described in subsection 5.1.1, with the plies of same fibre orientation being stacked and cohesive layers were introduced in the misaligned interfaces.

Two different materials definitions were considered one with the Hashin damage model and one with the VUMAT subroutine mentioned in section 5.2.

This implicated also having two different meshes in terms of element definition, with the Hashin model using `SC8R` elements for the IM7/8552 plies, and the VUMAT model using `C3D8I` elements. The cohesive elements used were the same, `COH3D8`. The mesh size has a total of 187200 elements, 33600 cohesive elements and 153600 solid elements. The mesh element sizes ranged from 1.4mm to 0.6mm (biggest dimension), in a bias fashion toward the hole, and in the out-of-plane direction there each ply section was discretised with four elements, to account for the real four stacked plies with the same fibre orientation, and the cohesive layers with one element. The final mesh is shown in Figure 6.4.

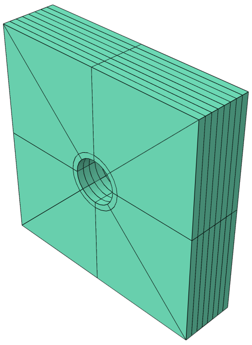

Figure 6.3: Open-hole local model geometry.

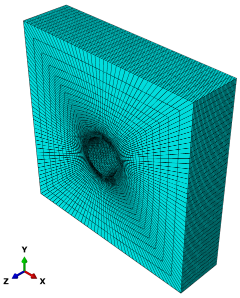

Figure 6.4: Open-hole local model mesh.

The boundary conditions for this model were defined using the `Abaqus` built-in submodeling boundary conditions with the settings as in Figure 6.5.

The step considered was a dynamic explicit one with the same settings as in subsection 5.1.5.

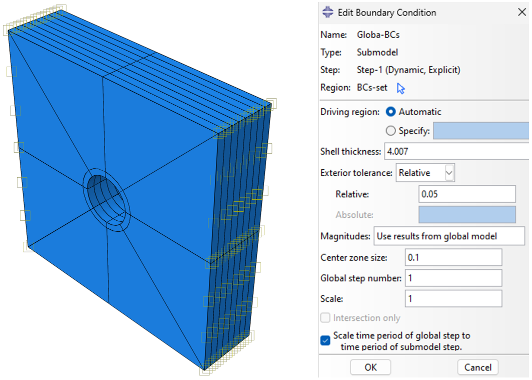

Name: Globa-BCs
Type: Submodel
Step: Step-1 (Dynamic, Explicit)
Region: BCs-set
Driving region: ● Automatic
○ Specify:
Shell thickness: 4.007
Exterior tolerance: Relative
Relative: 0.05
Absolute:
Magnitudes: Use results from global model
Center zone size: 0.1
Global step number: 1
Scale: 1
☐ Intersection only
☑ Scale time period of global step to time period of submodel step.

Figure 6.5: Open-hole local model boundary conditions

6.2.1 Results

Hashin model

For the Hashin local model the simulation ran in approximately 22 minutes. Figure 6.6 shows the an overlay plot of the global and local models with the displacement magnitude field, which allows to identify that the transfer of information from the global to the local model was correctly achieved. The kinetic and internal energy also fulfilled the requirement for a quasi-static analysis.

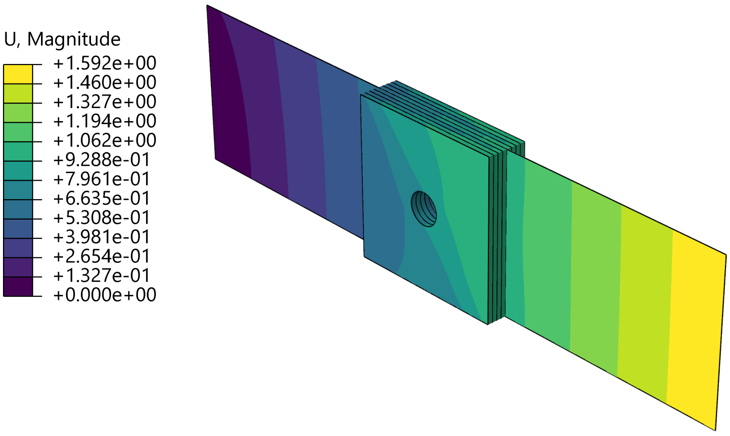

Figure 6.6: Open-hole global-local model displacement magnitude overlay plot, [mm].

As for the delamination results, Figure 6.7 shows the delamination state at the increment were SDEG reaches the value 1, meaning that the cohesive elements with that value have fully degraded in terms of stiffness. As in the reference open-hole model with the Hashin damage, the most critical ply seems to not be the correct one, the -45/0 interface, but instead the 90/45 one. This result is merely indicative of a not accurate enough simulation of the damage propagation as already seen before with this damage model. However, the contours are relatively close to the one of the Hashin reference model, which may demonstrate that the global-local modelling approach works, only the material damage formulation is limiting the accuracy of the results or even the mesh Figure 5.7.

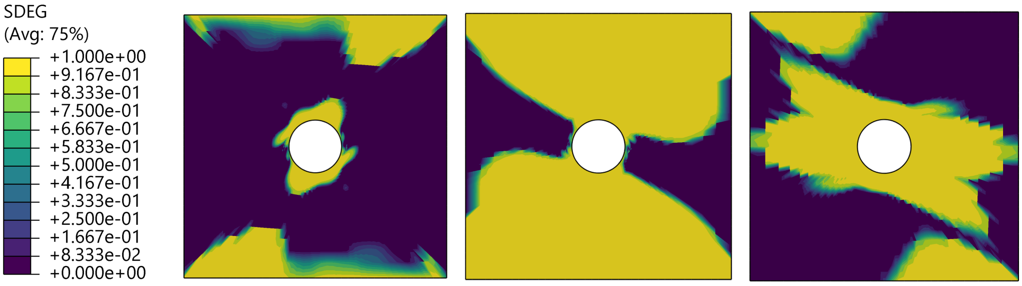

Figure 6.7: Stiffness degradation of the cohesive interfaces for the open-hole local model with Hashin damage. From left to right, the interfaces are 45/90, 90/45 and -45/0, respectively. Contour plotted on undeformed shape.

VUMAT model

For the VUMAT model the simulation ran for 46 minutes up to 34% of the step time, at which it aborted due to excessive element distortion. Several runs with different parameters were tried to eliminate this issue, but without success. The kinetic and internal energy also fulfilled the requirement for a quasi-static analysis so the issue was not coming from inertial effects. One possible cause of such error could be related to the VUMAT code itself, although no apparent bug was found either in the VUMAT or in the open-hole model. Upon this, the overlay plot could not be done due to the displacement field of the local model not being complete step time wise. Still, Figure 6.8 and Figure 6.9 show the equivalent displacement states for the global and local models, that show a correct transfer of information between the models.

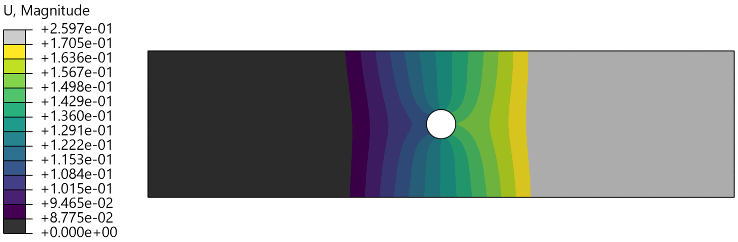

Figure 6.8: Open-hole global model displacement in coherence with the local model, [mm].

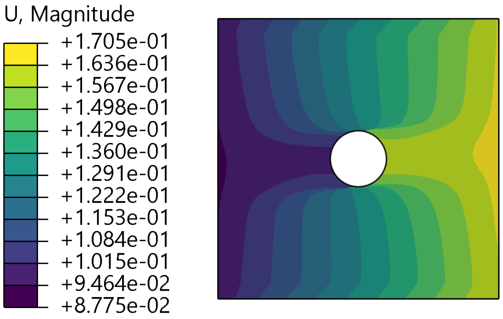

Figure 6.9: Open-hole local VUMAT model displacement before abortion, [mm].

Nonetheless, the simulation reaches the failure state of the cohesive layers, that is represented in Figure 6.10. By observing this contours, delamination seems to be following a path that will lead to something close to the ones of the VUMAT reference model, Figure 5.14. Thus, the global-local modelling can be said to be working correctly and the difference in contours arising from material models issues or even from the meshing itself.

The contours also indicate delamination propagation paths that may had led to similar contours of the ones simulated by Jiang, Hallett, Green, *et al.* [99], which tested six different configurations of the specimen considered, including one with the same composite layup as presented, by varying either the hole size, the ply thickness or the parameters m and n regarding the layup, Figure 5.16.

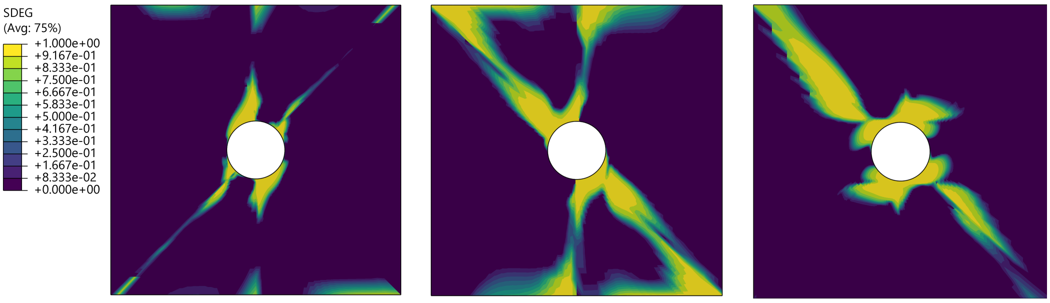

Figure 6.10: Stiffness degradation of the cohesive interfaces for the open-hole local model with VUMAT. From left to right, the interfaces are 45/90, 90/45 and -45/0, respectively. Contour plotted on undeformed shape.

Part IV

Wing-Box Finite Element Model

Chapter 7

Global Model

7.1 Generation of the model

In this section, the wing-box model will be explained, along with its dimensions, CAD modeling, materials. boundary conditions ans loads.

7.1.1 Model description

The geometry considered for the wing-box is presented in Figure 7.1, Figure 7.2, Figure 7.3, Figure 7.4.

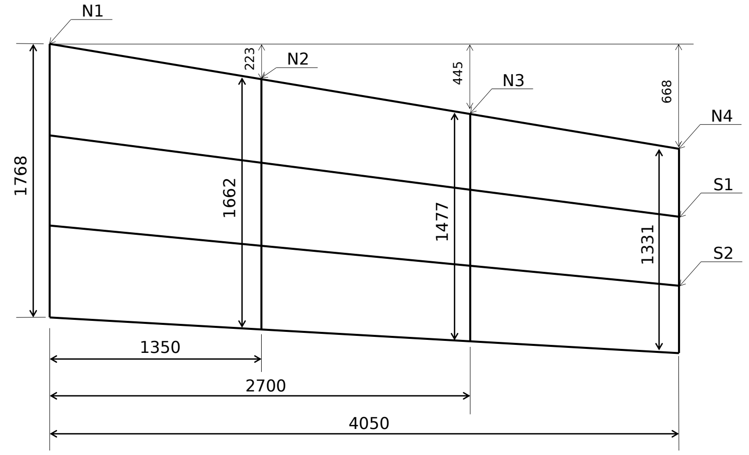
N1
N2
N3
N4
S1
S2
223
445
668
1768
1662
1477
1331
1350
2700
4050

Figure 7.1: Wingbox planform dimensions [mm].

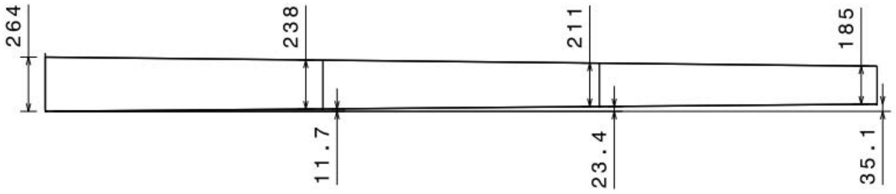
264
238
211
185
11.7
23.4
35.1

(a) L1

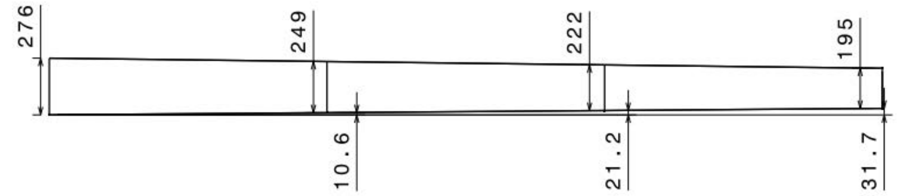
276
249
222
195
10.6
21.2
31.7

(b) L2

Figure 7.2: Spars geometry [mm].

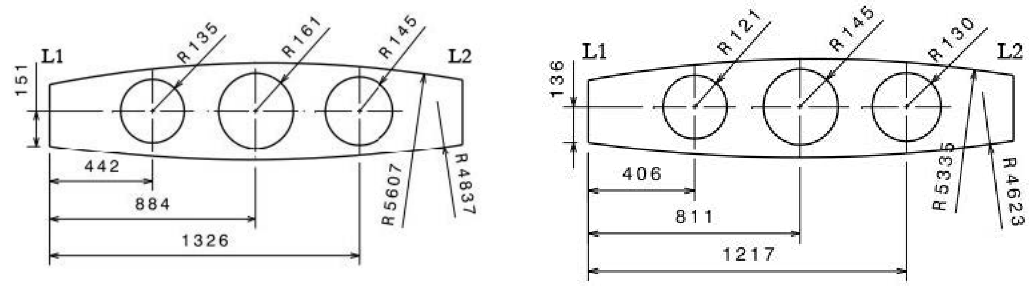
L1
R135
R161
R145
L2
151
442
884
1326
R5607
R4837
L1
R121
R145
R130
L2
136
406
811
1217
R5335
R4623

(a) N1 (b) N2

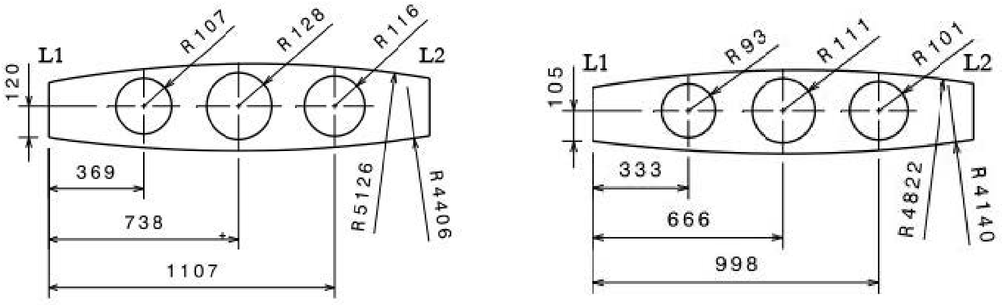
L1
R107
R128
R116
L2
120
369
738
1107
R5126
R4406
L1
R93
R111
R101
L2
105
333
666
998
R4822
R4140

(c) N3 (d) N4

Figure 7.3: Ribs geometry [mm].

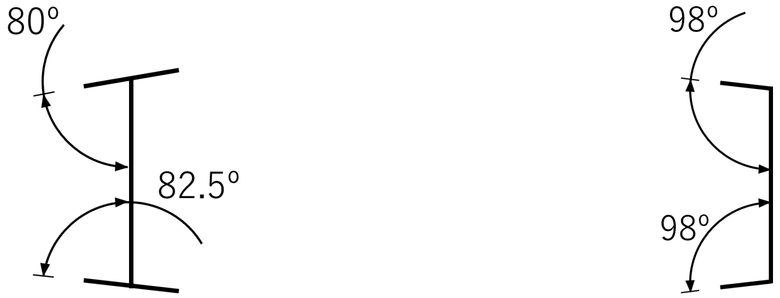

(a) Main front spar, L1. (b) Secondary rear spar, L2.

Figure 7.4: Flanges geometry.

The wing-box geometry was modelled with the following considerations in mind:

- The rib N1 is 450mm away from the wing's root.
- The main spar, L1, is at 13% of the airfoil's chord, and the secondary one, L2, at 75%.
- The ribs and spars are manufactured with a unique vending radius of 2mm.
- The lower skin has a circular inspection hole at the centre of central panel in the lower skin, with a diameter of 100mm, Figure 7.6.

Regarding the profiles shown in Figure 7.4:

- The main spar, L1, has an inclined I cross-section with constant flanges dimensions of 70×1.5 mm^2.
- The secondary spar, L2, has an inclined C cross-section with constant flanges dimensions of 35.5×1.5 mm^2 oriented toward the main spar, L1.
- The ribs have a C cross-section with flanges of 30×1 mm^2.

It is to note that the cruise speed and wing load are, respectively, 161.9 m/s and 2562 N/m2, the rib web 1.5 mm, the spar L1 web 2.5 mm, and the spar L2 web 2 mm. The upper skin comprises a $[0/45/-45/90]_{2s}$ layup where the ply thickness is 0.1 mm.

7.1.2 CAD model and Mesh

A detailed explanation of how the model was generated will not be presented in this part since this is not the objective of this work, rather a small description will be given as a walk-through the main steps of the creation of the 3D CAD model.

The first elements to be defined in the model were the vertices of the ribs of the wing box. Then it was created a 2D plane with a sketch of the ribs, being these used as a support to generate a shell through the loft tool, generating by this way the skin of the wing box. It is then possible to create the spars and its webs using, once again, datum planes. The geometry of each rib is then further improved through the addition of details such as the lightning holes. The final result is shown in Figure 7.5

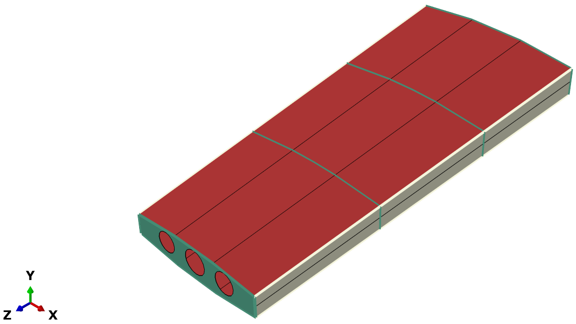

Figure 7.5: Wing-box CAD model coloured by material definition – red for composite, green for Al 2024-T3, and white for Al7475-T6.

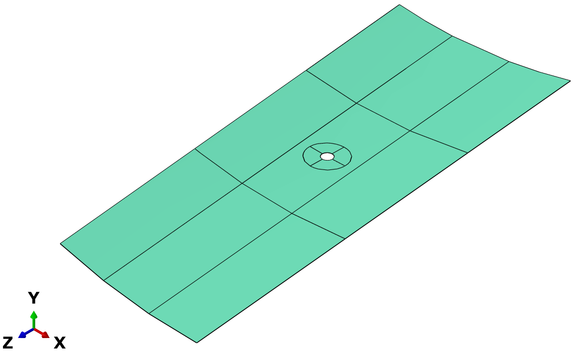

Figure 7.6: Win-box lower skin with the inspection hole.

Afterwards, the wing-box was discretized using a general mesh with a global size of approximately 20mm, with `S4R` and `S3R` shell elements, and `B31` beam elements, Figure 7.7.

7.1.3 Materials

As mentioned before, some aircraft have already reached the 50% mark regarding the use of composite materials in their primary structures. To account for this shift in aircraft manufacturing the wing-box model will be made out of aluminium and a carbon fiber reinforced laminated composite.

The composite skin has the properties shown in Table 7.1. The ribs material is the extensively used Al 2024-T3, Table 7.2, and the spars one is the Al 7475-T6, Table 7.3.

Table 7.2: Al 2024-T3 properties.

E_1	ν	ρ
74.4552 GPa	0.33	2.7 g/cm^3

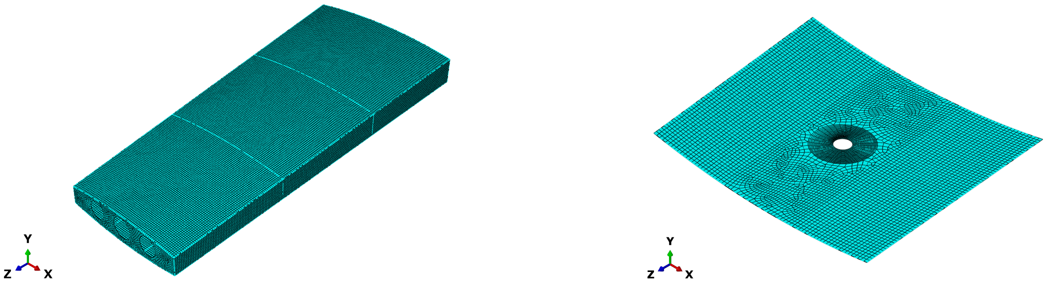

(a) Wing-box

(b) Lower centre panel.

Figure 7.7: Wing-box mesh

.

Table 7.1: IM7/8552 properties [100].

E_1	$E_2 = E_3$	$G_12 = G_13 = G_23$	ν_12	
171.420 GPa	9.08 GPa	5.29 GPa	0.34	
X_t	X_c	Y_t	Y_c	S_{12}
2323.5 MPa	1200.1 MPa	62.3 MPa	253 MPa	92.3 MPa

Table 7.3: Al 7475-T6 properties.

E_1	ν	ρ
71.0082 GPa	0.33	2.7 g/cm^3

7.1.4 Boundary Conditions

In order to establish the boundary conditions, the wing-box was conceptualized as a beam experiencing flexural and torsional loadings. For the purpose of this analysis, only an intermediate section of the wing-box was examined, with the first rib, rib N1, located at a distance of 450 mm from the root of the wing-box. Consequently, the model can be likened to a section cleaved from a larger beam, necessitating the definition of loads and boundary conditions at both ends of the section. These conditions arise from the forces and moments exerted by the adjacent sections on the analysed section. This conceptualization is depicted in Figure 7.8, serving to illustrate the aforementioned considerations.

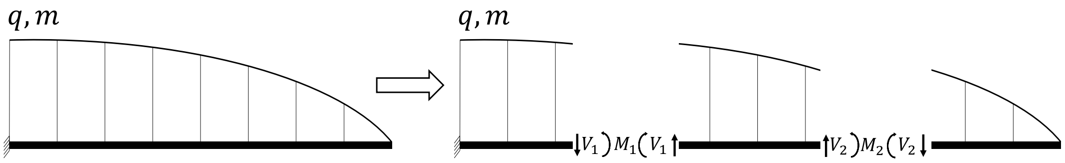

Figure 7.8: Beam approximation.

In this configuration, the wing-box section is treated as an isolated entity with loads acting at both ends, arising from the interactions with the surrounding components of the wing-box, as well as the externally applied loads specific to the analysed section. However, due to the challenges associated with reproducing a free-body diagram in Abaqus, an alternative approach was adopted. This involved imposing the known displacements and rotations at one end, while applying the resulting forces and moments from the remaining structure at the other end. This methodology is visually depicted in Figure 7.9.

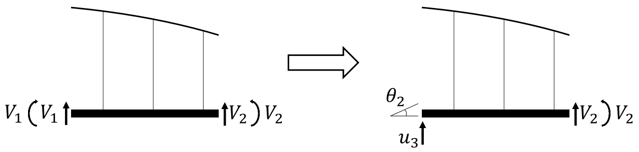

Figure 7.9: Beam approximation equivalent boundary conditions.

Given that the studied section resides at a moderate distance from rib N1, which serves as the foundation of the model, and the wing-box root, it is justifiable to assume minimal displacements and rotations at the base of the model, rendering it effectively fixed. However, since the wing-box section is primarily connected to the adjacent section near the wing-box root through the spars, as well as skins, the fixation of the model's base was selectively applied solely to the web of the spars. Further support was provided by the rib N1, resulting in a configuration akin to a simply-supported structure, as illustrated in Figure 7.10.

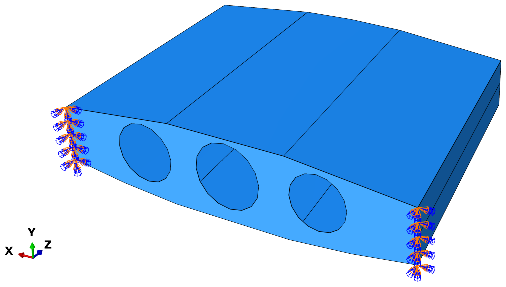

Figure 7.10: Wing-box boundary conditions.

7.1.5 Loads

The load case applied in the finite element model was that of a critical gust scenario, with a positive load factor of $n_z = 1.5$ and also a scale factor of 3 to force an extreme load scenario where failure is set to occur. The load data used is the same as the one introduced in the class of Aeronautical Structures Analysis, lectured at FEUP in the master's in Aeronautical Structures, and is presented in Table 7.4 and represented graphically in Figure 7.11, along with regions for load estimation, where v_{z_1} and v_{z_2} are the vertical shear loads in the main and secondary spars respectively.

Table 7.4: Critical gust load case.

x [mm]	v_y [N/mm]	v_{z1} [N/mm]	v_{z2} [N/mm]
0	0.0609	0.88149	0.24347
505.3	0.056642	0.8616	0.23695
1010.5	0.052378	0.84265	0.23018
1515.8	0.048207	0.82428	0.22317
2021.1	0.044213	0.80611	0.21591
2526.3	0.040459	0.7878	0.2084
3031.6	0.036993	0.76902	0.20066
3536.8	0.033846	0.74947	0.19267
4042.1	0.031033	0.72883	0.18446
4547.4	0.028549	0.70683	0.17601
5052.6	0.026374	0.68321	0.16735
5557.9	0.024471	0.65771	0.15847
6063.2	0.022786	0.6301	0.14937
6568.4	0.021246	0.60016	0.14008
7073.7	0.019763	0.56769	0.13059
7578.9	0.018232	0.53251	0.12091
8084.2	0.016529	0.49443	0.11106
8589.5	0.014515	0.45331	0.10104
9094.7	0.012033	0.40902	0.090859
9600	0.0089083	0.36142	0.080537

The load values presented before are distributed along th wing-box and in order to model them as concentrated forces the correspondent area under the graphs for each region highlighted was considered. The vertical red lines mark the position of the ribs being N1 the leftmost line and N4 the rightmost one, adn the gray lines separate the regions for load estimation. So in summary, the regions considered are:

- **N1:** 225-1125 [mm]
- **N2:** 1125-2475 [mm]
- **N3:** 2475-3825 [mm]
- **N4:** 3825-5175 [mm]
- **Tip:** from 5175mm to the end of the graph.

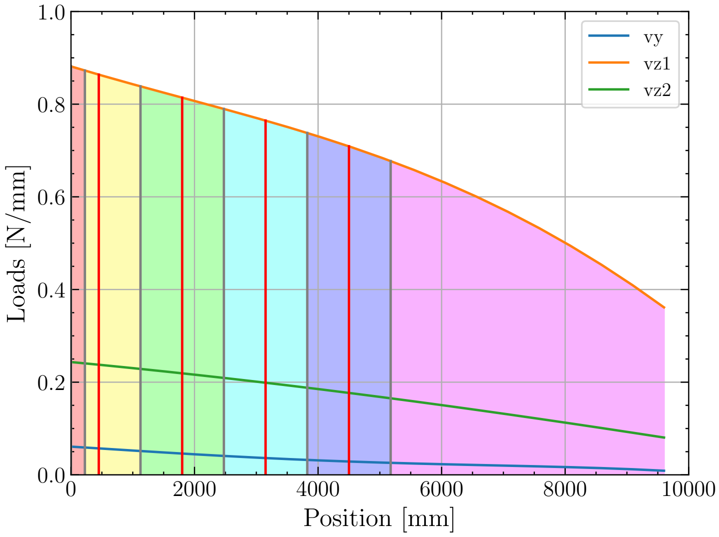

Figure 7.11: Wing regions for loads estimation.

Table 7.5: Shear force values.

	N1	N2	N3	N4	Tip
Color	**Yellow**	**Green**	**Cyan**	**Blue**	**Lilac**
V_z [N]	980.93	1394.69	1300.05	1195.06	2925.85
V_{z1} [N]	756.99	1080.69	1014.68	940.80	2924.73
V_{z2} [N]	207.67	290.760	263.880	234.780	548.808
V_y [N]	48.87	61.09	48.28	38.38	81.49

Table 7.5 presents the loads calculated from the integration of the area under the graph for each region.

Since `Abaqus`, does not allows the application of concentrated moments on surfaces, a different approach had to be conducted. The "Structural distributed coupling" method featured with linear weighting was adopted and a reference point was defined at the aerodynamic centre of the rib N4 along with a coupling constraint encompassing the reference point and all rib N4 nodes.

To calculate the shear forces and bending moments originating from the wing-box's tip Equation 7.1 and Equation 7.2 can be used, where V represents the resulting shear forces, v the distributed shear force, M the resulting bending moment, and Y the distance of the point i to the rib N4.

$$V_i = V_{i-1} + \frac{v_i + v_{i-1}}{2} \dot{} (Y_{i-1} - Y_i) \tag{7.1}$$

$$M_i = M_{i-1} + \frac{V_i + V_{i-1}}{2} \dot{} (Y_{i-1} - Y_i) \tag{7.2}$$

Table 7.6: Resulting bending moments acting on the wing tip.

M_y [N/mm]	M_z [N/mm]
7 940 047.64	214 197.32

The graphs obtained from the application of these equations is depicted in Figure 7.12. Table 7.6 synthesises the resulting values used in the finite element model.

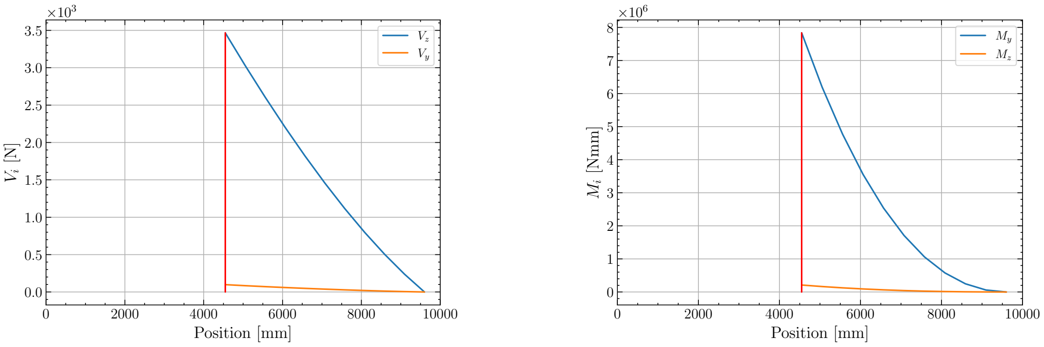

(a) Wing tip shear forces.

(b) Wing tip Bending moments.

Figure 7.12: Wing tip loads.

The finite element model with all the previous mentioned loads are shown in Figure 7.13. It is important to recall that the loads presented before were then multiplied by a scale factor of 3 and also a safety coefficient of 1.5.

7.2 Simulation setup

Considering the aforementioned model of the wing-box, this section will focus on the simulation setup aspects, such as solver type, step type, etc.

Since this model is to be used as a global model for the refined local part around the lower skin inspection hole, only the displacement field is of interest since it will be used as a boundary condition to drive the local model simulation. Therefore, no damage evolution or nonlinear geometric formulations were considered.

The solver chosen was the `Abaqus Standard`, which encompasses an implicit integration scheme and the step type used was the *Static, General* one, with a step time of 1s.

Also, all the loads were defined with a smooth amplitude curve which is defined in `Abaqus` by Equation 7.4, between two consecutive data points (t_i, A_i) and (t_{i+1}, A_{i+1}), with t being a time point and A an amplitude value between 0 and 1. The curve for the

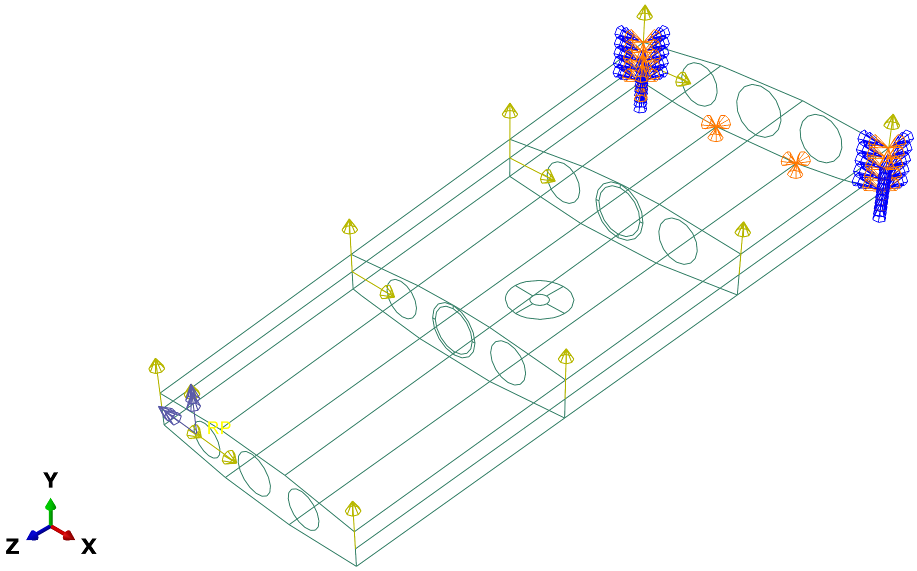

Figure 7.13: Wing-box FEM model with applied loads and boundary conditions.

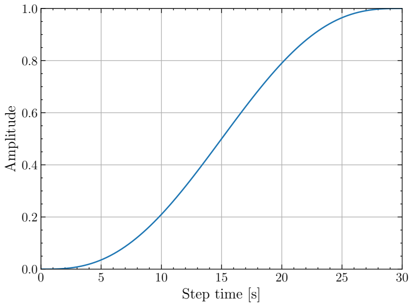

Figure 7.14: Smooth amplitude curve.

present simulation is presented in Figure 7.14 [78].

$$a = A_i + (A_{i+1} - Ai)\,\xi^3(10 - 15\xi + 6\xi^2), \qquad \text{for } t_i \le t \le t_{i+1} \tag{7.3}$$

$$\xi = \frac{t - t_i}{t_{i+1} - t_i} \tag{7.4}$$

The step time was discretized in fixed increments of 1s each.

7.3 Results

Since the simulation was fully linear, it ran smoothly without any convergence issue and the displacement fields, which are the outputs of interest for the following local model, can be observed in Figure 7.15. A more complete display of the displacement fields may be observed in Appendix A.

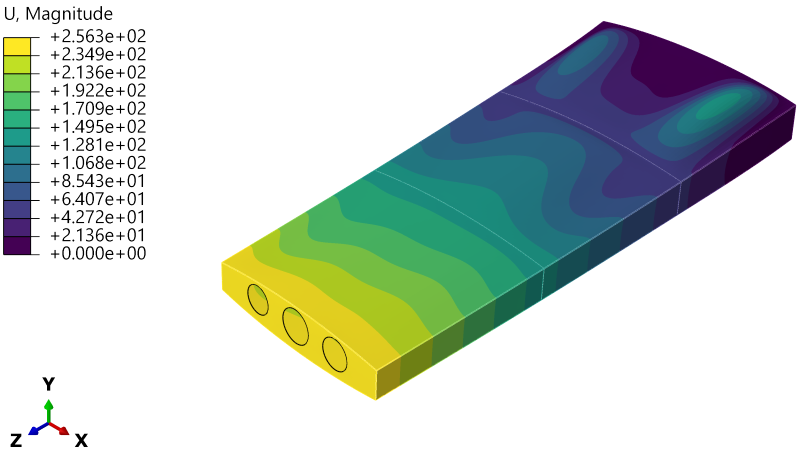
U, Magnitude
+2.563e+02
+2.349e+02
+2.136e+02
+1.922e+02
+1.709e+02
+1.495e+02
+1.281e+02
+1.068e+02
+8.543e+01
+6.407e+01
+4.272e+01
+2.136e+01
+0.000e+00
Y
Z
X

Figure 7.15: Wing-box displacement magnitude [mm], scale factor of 1.

Chapter 8

Local Model

This chapter will expose the geometry modelling of the local part of interest, namely the inspection hole in the bottom skin, as well as the boundary conditions and simulation settings used.

8.1 Generation of the model

To model a refined local part around the inspection hole, a chunk of the bottom skin was cut with a radius of 200mm, Figure 8.1.

The local part was fully modelled with 3D elements, instead of shell elements like in the global model. In order to do so, a new geometry must be defined to account for each ply individually as well as the cohesive layers between them.

8.1.1 CAD model and Mesh

Following the description stated above, to model the local part as a stack of 3D element layers the loft feature provided by `Abaqus` was employed. From the global model, the four vertices that delimit the bottom skin of the wing-box's second bay and the respective arch radius were retrieved, Figure 7.1,Figure 7.2, Figure 7.3, and are summarised in Table 8.1

Table 8.1: Bay 2 vertices and arc radius [mm].

Rib N2	$[223.0, 11.7]$	$[1845.0, 10.6]$	4623.0
Rib N3	$[445.0, 23.4]$	$[1922.0, 21.2]$	4406.0

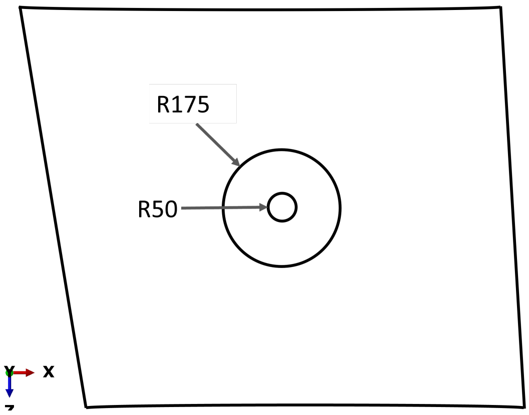

Figure 8.1: Schematic of the wing-box chunk to be used as a local part.

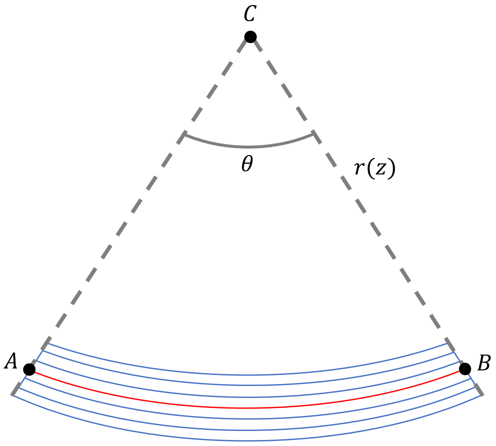

Figure 8.2: Sketch approach for the wing-box local part loft sections.

With this data, the respective arc centres were calculated and also the angle between the ends, which allowed to draw the sketches for the loft sections as in Figure 8.2. The red line in the figure represents the position of the global model shell skin, C the arc centre , θ the angle between points A and B, and $r(z)$ the radius of the arc with z varying accordingly to the ply or cohesive layer distance to the red line, in the radial direction. The ply thickness is the same of the global model, and the cohesive layers were set to 0.001mm.

The result from the lofts is a full 3D model of the wing-box second bay lower skin, Figure 8.3. From that skin a disk like chunk was cut as shown before in Figure 8.1, leading to the final geometry depicted in Figure 8.4.

From the final geometry, a mesh of hexahedral was generated with the element sizes specified in Table 8.2 and graphically displayed in Figure 8.5. The composite plies were modelled analogously to the open-hole model discussed before with `C3D8I` elements, and the cohesive layers with `COH3D8`. The number of `C3D8I` elements was 176960 and of `COH3D8` was 165900, giving a total of 342860 elements.

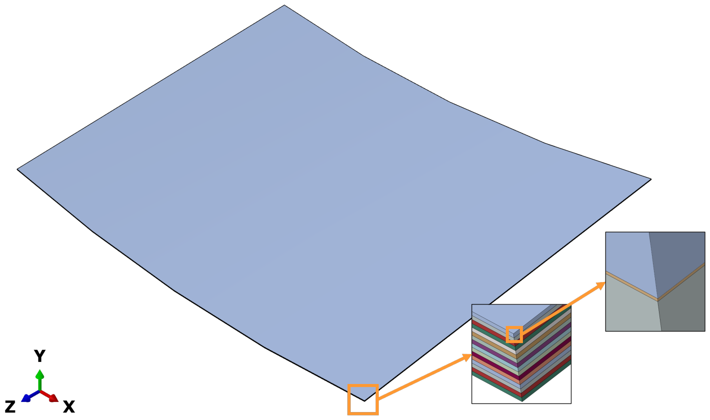

Figure 8.3: Second bay lower skin obtained from the lofts. The zoomed pictures highlight the different plies and in-between cohesive layers.

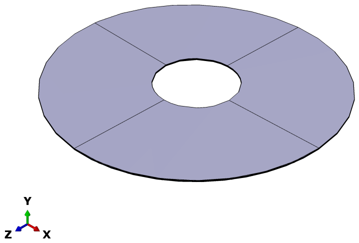

Figure 8.4: Wing-box local part final geometry.

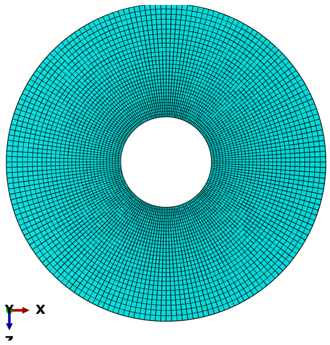

Figure 8.5: Wing-box local part mesh.

Table 8.2: Local part mesh element sizes.

Outer Circle	**Inner Circle**	**Radial Bias**	**Through Thickness**
6mm	1.7mm	6mm to 3mm	1mm

8.1.2 Materials

The materials used were the already mentioned IM7/8552 for the plies, with the properties of Table 7.1 and for the cohesive layers the properties can be seen in Table 8.3.The damage initiation criteria considered was the quadratic nominal stress and a bilinear damage evolution law.

Table 8.3: Cohesive properties for the wing-box local model.

K_n	τ_n	τ_{sh}	G_{IC}	G_{IIC}	η	ρ
$1 \cdot 10^6$ N/mm^3	62.3 MPa	92.3 MPa	0.28 kJ/m^2	0.79 kJ/m^2	1.45	1.58 g/cm^3

A buffer zone in the cohesive plies, considering only the elastic properties, was also defined to mitigate the appearance of singularities in the boundary conditions, Figure 8.6.

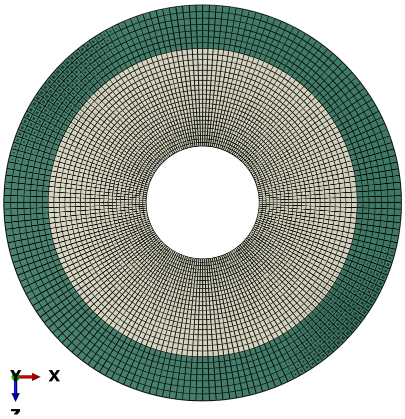

Figure 8.6: Wing-box local model cohesive buffer zone, the green part is purely elastic and the white part includes the damage initiation and damage evolution definition.

8.1.3 Boundary Conditions

The boundary conditions come from the displacement field of the global model, and were applied to the model via the submodeling boundary condition available in `Abaqus`. The setup used can be seen in Figure 8.7.

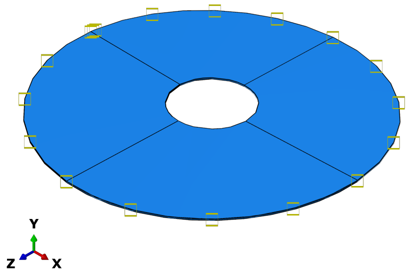

Figure 8.7: Wing-box local model boundary conditions.

8.2 Simulation setup

The step was defined as a dynamic implicit one with the same step time of the global model, 1s. The NLGEOM option was set to off.

8.3 Results

The simulation ran in 4.6 min and the overlay plot of the displacement fields of the global and local wing-box model is represented in Figure 8.8. The displacements transfer occurred seamlessly which indicates that the global-local setup was properly defined.

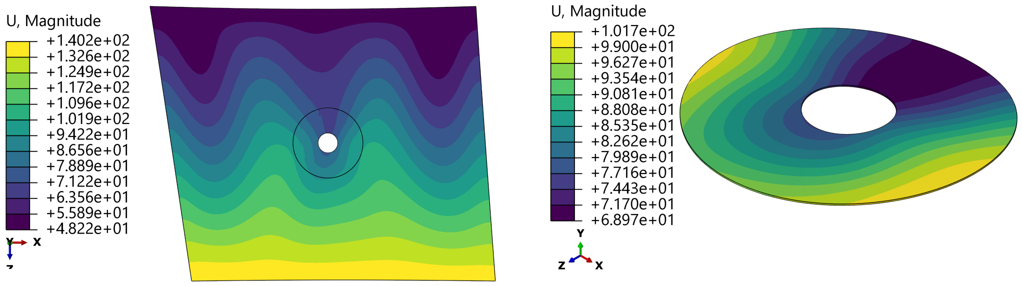

Figure 8.8: Wing-box displacement overlay plot with the global model and local model displacement , [mm].

About the delamination, it didn't occur with the maximum value of variable indicating the initiation of damage (QUADSCRT) being only 0.02392. Such low value indicates that the load applied is not sufficient to trigger delamination at the hole edges.

However, it is important to highlight that the global-local approach worked and also the the spots where delamination will most probably start can already be seen, Figure 8.9b and Figure 8.9c. It is also noticeable the correlation between the zones with higher Von Mises stress and the zones were delamination was starting to appear.

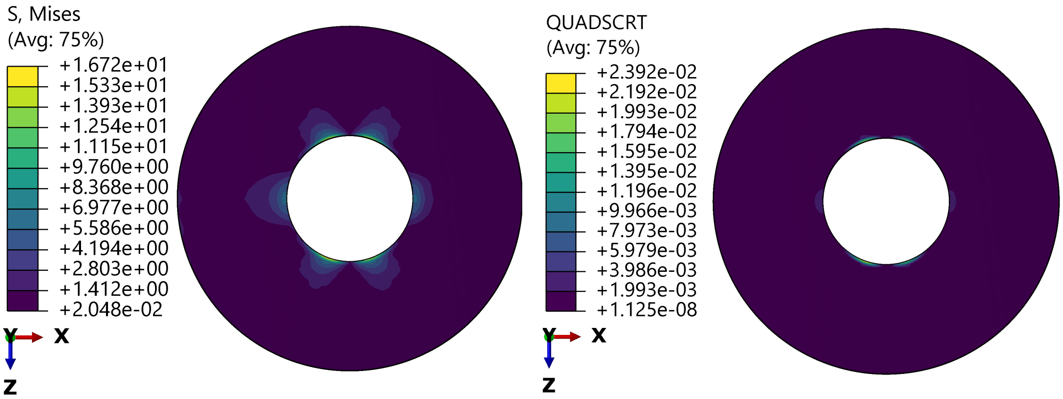

(a) Von Mises stress [MPa].

(b) Damage initiation variable (QUADSCRT)

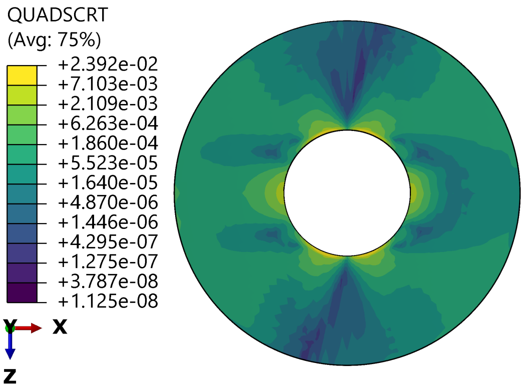

(c) Damage initiation variable (QUADSCRT) with logarithmic scale.

Figure 8.9: Wing-box local model most critical ply results, interface 0°/45°.

8.4 Other models

Since delamination was not achieved with the previous formulation, some other models were developed including intra and interlaminar damage laws via a UMAT, for implicit analysis, and via a VUMAT, for explicit analysis. Unfortunately, the introduction of such subroutines did not perform well with local model and strange behaviours were happening as seen in Figure 8.10.

For this model with the UMAT it seems that there was a problem in the region defined through the user subroutine, while in the buffer zone the behaviour of the model seems to be in agreement with the one observed in the global and local model previously discussed. Right at the first increment, some of the damage state variables defined in the UMAT reached the critical value which could indicate wrong material properties definition, to high load rate or coding error within the UMAT.

As for the material properties, they were checked multiple times and also were retrieved from a research work [100] that implemented them in finite element models without issues. Regarding the load rate, both the global and local model step times were adjusted to 30s and the maximum increment set to 0.5s to ensure the gradual application of the loads.

Even with this modifications to the original models the problems persisted, which ultimately leads to believe that error source might be the UMAT subroutine, but since it was programmed by a third party it was not possible to find the bug due to the lack of familiarization with the code. This highlights the intricate of process of composite damage failure simulation, which relies not only on complex mathematical formulations but also in their correct implementation into numerical tools that can be used by finite element analysts in any given case.

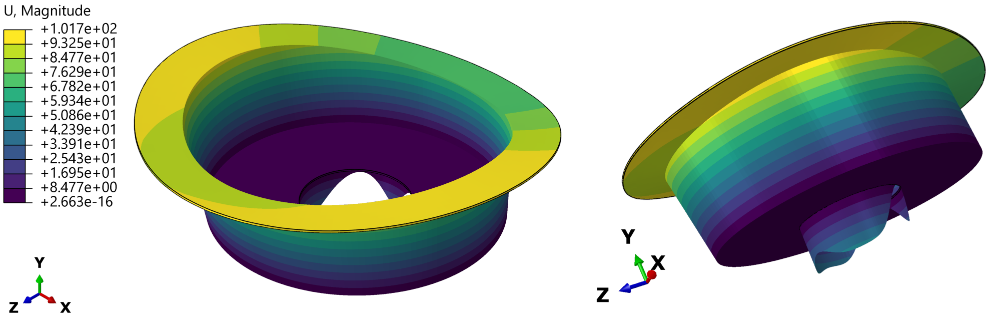

Figure 8.10: Wing-box local model with inter and intralaminar damage model via UMAT displacement field.

8.5 Curved thin shells

The curvature presented by the wing-box skin may be a root cause for the difficulty in modelling its behaviour via finite element method. As described by Hart-Smith, the traditional formulation for in-plane shear strain in curved thin shells is affected by serious first-order errors due to its intrinsic assumptions and simplifications [101]. This issue and others that may have not been spotted yet within the traditional formulations implemented in finite element codes, for either shells, curved shells or composites, can pose a serious obstacle to simulations including components with curvature as the one here presented.

Part V

Conclusions and Future Work

Chapter 9

Conclusions and Future Work

9.1 Conclusion

The present thesis focused on the development of a global-local finite element methodology to predict interlaminar failure on composite structures, namely delamination. In the first part a review on the current state of the art regarding composite structures in the aeronautical field, composite failure mechanisms and global local techniques was conducted. From this analysis it was clear that this industry is shifting its mindset more and more toward CFRP structures and also towards computational tools, especially the finite element model, to overcome the expensive laboratory testing of such materials.

However, employing computational tools like finite element models require an extensive support on experimental data that can validate its accuracy and allow the extrapolation to other structures different from the validation ones. Laminated materials often undergo localized failures at smaller length scales before reaching ultimate rupture, that gradually develop and accumulate during the loading process that may result in catastrophic failure. When performing a finite element simulations of composites an important step is to define the modelling scale. As the scale becomes lower it gives more accurate results, but computational cost needs to be taken into account and a trade-off must be defined. To assess damage failure in the overall laminate the preferred scale is the one denoted as mesoscale, which relies on a ply-by-ply discretisation of the laminate, where each ply is modelled with homogenised properties.

Global-local techniques have been developed by several researches over the years and present a powerful tool in finite element analysis of complex structures. It can be said that the global-local modelling approach presents some challenges regarding geometrical modelling and meshing. The boundary condition interface between the local and global models is a very sensitive region that if not properly defined can lead to erroneous displacement transfers which consequently lead to inaccurate results. It is important to highlight that the geometric transposition from a shell mode to full 3D model in curved part accommodating separate layers for the plies and cohesive interfaces is a very tricky process that can quickly lead to wrong geometric definition. For the wing-box model the part was curved posed a big challenge in making the "slice like" part definition to obtain the mesoscale model of the laminate, mainly due to limitations in the `Abaqus` CAD features. Either for the open-hole models of for the wing-box one, the one-way global to local transfer of information was achieved and properly established. For the open-hole reference model with Hashin damage an approximately 38% reduction in simulation time was achieved by employing these technique. For the open-hole models with the VUMAT this cannot be calculated since the local model aborted midway through. As for the wing-box, although there is no full 3D reference model and that the delamination initiation point was not reached, it was seen that a global-local approach can be a used to determine delamination failure initiation in a quick manner, since up to that point the model is fully linear and thus computational cost is not high.

Regarding delamination, the cohesive zone modelling technique was conducted by means of `COH3D8` elements governed by a quadratic traction criteria and a the BK law, and of some models via VUMAT containing a more evolved interlaminar damage model than the one provided by `Abaqus`. Delamination initiation and propagation was achieved on the open-hole models but not in the wing-box case.

Although delamination happens, it was already discussed that the results are not in perfect agreement with experimental and other finite element data coming from the literature. Several models were developed during the execution of this project in a quest to overcome the simulation inaccuracy regarding delamination initiation and propagation, either by implicit integration models or by using user defined material models including progressive damage for the explicit counterpart via VUMAT. However errors during simulations, such as abortion due to excessive element distortion or wrong behaviour of the local model, as in Figure 8.10 limited the outcomes and did not allow to observe an improvement in the results accuracy.

Material properties and simulation settings were tweaked several times to try triggering a different behaviour, and also different meshes were created but the issues still persisted. Since boundary condition interface is a very critical part of global-local finite element models, buffer zones were also tried with the user subroutines models, to avoid singularities caused by the elements at those locations, but it did not make a significant effect on the results. One possible explanation for the simulations issues might come from the material model coded in the subroutines used, since the models defined with the Hashin damage model provided by `Abaqus` did not show any simulation errors and ran smoothly till the end, with only its results being far from realistic ones. This indicates that allegedly the global-local models were well defined were correctly setup and working and the issues were coming from the material models.

In summary, it can be said one of the objectives of this thesis was fulfilled with a global-local one-way approach being successfully implemented, and highlighting that it can be easily achieved, providing that the appropriate meshes are developed and boundary conditions are properly defined. The other objective of this work, was not fully fulfilled with delamination initiation and propagation being observed at least for the open-hole validation models, but the accuracy of the results being distant from what was expected. With this in mind, the biggest obstacle to the present work was without a doubt the accurate modelling of composite failure mechanisms, that still to this day are on of the core topics of research regarding composites.

9.2 Future Work

In spite of the increasing number of publications regarding global-local finite element model techniques and even more of damage in composite materials, both experimental and numerical studies need to be conducted to continue extending the knowledge base on composite materials characterization including their complex damage failure mechanisms. Even with a much better computational power that a few decades ago, the quest for reliable and computational cheaper tools are still a very current topic, since the more power you have the more complex simulations will be, so results can be of high fidelity and maybe substitute physical experiments in total.

Diving into the global-local techniques, several formulations for finite element applications with such approaches can be found within the literature as well as in commercial softwares like `Abaqus`. In this work it was presented the base configuration of this method, being it a one-way coupling approach. An interesting further study would be to implement a two-way coupling procedure that would allow an iterative simulation scheme towards a more accurate solution. Another study that could be conducted, although not as interesting, would be to develop a model using shell-to-solid coupling but within the same model, i.e., at the local area of interest a switch from a shell elements mesh to a 3D would be modelled.

Regarding the damage failure of composite, and especially delamination, research around this topics is still largely conducted by many academic institutions as well as federal entities such as NASA. Although the literature proposes several models to simulate composite damage failure, their implementation is mostly validated for simple test such as tensile tests, compressive tests, DCB tests, ENF test, etc.. When translating those models to more complex structures, issues may arise, not from the mathematical formulation side, but from the implementation in the softwares. Thus a better implementation of such damage models within finite element codes should be of primary focus for either scholars or companies that developed commercial finite element codes. Taking this into consideration, future works should focus a meticulous definition of damage models and their implementation in finite element models, especially for more complex structures such as the on of the wing-box presented in this work.

Bibliography

[1] R. Boyer, “Aircraft Materials,” in *Encyclopedia of Materials: Science and Technology*, K. H. J. Buschow, R. W. Cahn, M. C. Flemings, *et al.*, Eds. Oxford: Elsevier, 2001, pp. 66–73, ISBN: 978-0-08-043152-9. DOI: https://doi.org/10.1016/B0-08-043152-6/00013-9. [Online]. Available: https://www.sciencedirect.com/science/article/pii/B0080431526000139.

[2] E. A. Starke and J. T. Staley, “24 - Application of modern aluminium alloys to aircraft,” in *Fundamentals of Aluminium Metallurgy*, R. Lumley, Ed. Woodhead Publishing, 2011, pp. 747–783, ISBN: 978-1-84569-654-2. DOI: https://doi.org/10.1533/9780857090256.3.747. [Online]. Available: https://www.sciencedirect.com/science/article/pii/B9781845696542500249.

[3] A. P. Mouritz, “2 - Aerospace materials: past, present and future,” in *Introduction to Aerospace Materials*, A. P. Mouritz, Ed. Woodhead Publishing, 2012, pp. 15–38, ISBN: 978-1-85573-946-8. DOI: https://doi.org/10.1533/9780857095152.15. [Online]. Available: https://www.sciencedirect.com/science/article/pii/B9781855739468500029.

[4] C. Niu and M. Niu, *Composite Airframe Structures: Practical Design Information and Data.* Conmilit Press, 1992, ISBN: 9789627128069. [Online]. Available: https://books.google.pt/books?id=--pGAQAAIAAJ.

[5] M. Arif, M. Asif, and I. Ahmed, “Advanced composite material for aerospace application—a review,” *Int. J. Eng. Manuf. Sci*, vol. 7, no. 2, pp. 393–409, 2017.

[6] J. R. Vinson, “Sandwich structures: Past, present, and future,” in *Sandwich Structures 7: Advancing with Sandwich Structures and Materials*, O. T. Thomsen, E. Bozhevolnaya, and A. Lyckegaard, Eds., Springer Netherlands, pp. 3–12, ISBN: 978-1-4020-3848-8.

[7] C. Soutis, “Carbon fiber reinforced plastics in aircraft construction,” *Materials Science and Engineering: A*, vol. 412, no. 1, pp. 171–176, 2005, ISSN: 0921-5093. DOI: https://doi.org/10.1016/j.msea.2005.08.064. [Online]. Available: https://www.sciencedirect.com/science/article/pii/S0921509305009780.

[8] N. Zimmermann and P. H. Wang, “A review of failure modes and fracture analysis of aircraft composite materials,” *Engineering Failure Analysis*, vol. 115, p. 104 692, 2020, ISSN: 1350-6307. DOI: https://doi.org/10.1016/j.engfailanal.

2020.104692. [Online]. Available: https://www.sciencedirect.com/science/article/pii/S1350630720307020.

[9] F. Romano, A. Sorrentino, L. Pellone, U. Mercurio, and L. Notarnicola, "New design paradigms and approaches for aircraft composite structures," *Multiscale and Multidisciplinary Modeling, Experiments and Design*, vol. 2, no. 2, pp. 75–87, 2019, ISSN: 2520-8179. DOI: 10.1007/s41939-018-0034-8. [Online]. Available: https://doi.org/10.1007/s41939-018-0034-8.

[10] J. Rouchon, "Certification of large airplane composite structures," in *ICAS Congress Proceedings*, vol. 2, pp. 1439–1447.

[11] T. Swift, "Damage tolerance capability," *International Journal of Fatigue*, vol. 16, pp. 75–94, 1994.

[12] S. Waite, "19 - certification and airworthiness of polymer composite aircraft," in *Polymer Composites in the Aerospace Industry (Second Edition)*, P. Irving and C. Soutis, Eds. Woodhead Publishing, 2020, pp. 593–645, ISBN: 978-0-08-102679-3. DOI: https://doi.org/10.1016/B978-0-08-102679-3.00019-8. [Online]. Available: https://www.sciencedirect.com/science/article/pii/B9780081026793000198.

[13] T. Dong and N. H. Kim, "Cost-effectiveness of structural health monitoring in fuselage maintenance of the civil aviation industry †," *Aerospace*, vol. 5, no. 3, p. 87, 2018, ISSN: 2226-4310. [Online]. Available: https://www.mdpi.com/2226-4310/5/3/87.

[14] J. Schijve, "Fatigue damage in aircraft structures, not wanted, but tolerated?" *International Journal of Fatigue*, vol. 31, no. 6, pp. 998–1011, 2009, ISSN: 0142-1123.

[15] S. M. O. Tavares and P. M. S. T. de Castro, "Maintenance," in *Damage Tolerance of Metallic Aircraft Structures: Materials and Numerical Modelling*. Cham: Springer International Publishing, 2019, pp. 17–22, ISBN: 978-3-319-70190-5. DOI: 10.1007/978-3-319-70190-5_2. [Online]. Available: https://doi.org/10.1007/978-3-319-70190-5_2.

[16] J. Lin, "Durability and damage tolerance analysis methods for lightweight aircraft structures: Review and prospects," *International Journal of Lightweight Materials and Manufacture*, vol. 5, no. 2, pp. 224–250, 2022, ISSN: 2588-8404.

[17] F. De Florio, *Airworthiness: An introduction to aircraft certification and operations*. Butterworth-Heinemann, 2016, ISBN: 0081009402.

[18] S. J. Findlay and N. D. Harrison, "Why aircraft fail," *Materials Today*, vol. 5, no. 11, pp. 18–25, 2002, ISSN: 1369-7021. DOI: https://doi.org/10.1016/S1369-7021(02)01138-0. [Online]. Available: https://www.sciencedirect.com/science/article/pii/S1369702102011380.

[19] M. Gorelik, "Additive manufacturing and risk mitigation—a regulatory perspective," in *Proceedings of FAA-AF additive manufacturing workshop, Dayton, OH, USA. DOT/FAA/TC-16/15*.

[20] F. A. Administration, *Title 14: Aeronautics and space, chapter i: Federal aviation administration, department of transportation, subchapter c: Aircraft, part 25: Airworthiness standards: Transport category airplanes, subpart c: Structures, § 25.571(a)(3)*, Code of Federal Regulations, 2023.

[21] U. D. o. Defense, *Aircraft structural integrity program (asip), mil-std-1530c (usaf)*, Government Document, 2005.

[22] C. Boller and M. Buderath, "Fatigue in aerostructures—where structural health monitoring can contribute to a complex subject," *Philosophical Transactions of the Royal Society A: Mathematical, Physical and Engineering Sciences*, vol. 365, no. 1851, pp. 561–587, 2007, ISSN: 1364-503X.

[23] F. A. Administration, "Advisory circular 20-107," *Composite Aircraft Structure*, 1978.

[24] G. Negaard, "The history of the aircraft structural integrity program, aerospace structures information and analysis center report no," en, in *680.1B, Air Force Flight Dynamics Laboratory, Wright-Patterson Air Force Base*, Dayton, Ohio, 1980. [Online]. Available: `https://apps.dtic.mil/dtic/tr/fulltext/u2/a361289.pdf.`.

[25] A. Administration, "Federal aviation administration, dot ards: Transport category subpart a — general," io, *Main*, no. 1, pp. 650–735, 2009.

[26] E.A.S.A., *Cs-25 certification specifications and acceptable means of compliance for large aeroplanes*, en, 2011.

[27] J. H. Kweon, H. J. Son, J. Y. Choi, S. Y. Shin, J. H. Choi, and G. M. Lee, "Progressive failure analysis of unidirectional-fabric laminated composite joints under pin-loading," *Key Engineering Materials*, vol. 334, pp. 1–4, 2007.

[28] M. K. Budzik, S. Heide-Jørgensen, and R. Aghababaei, "Fracture mechanics analysis of delamination along width-varying interfaces," *Composites Part B: Engineering*, vol. 215, p. 108 793, 2021.

[29] P. Liu and Z. Gu, "Finite element analysis of single-leg bending delamination of composite laminates using a nonlinear cohesive model," *Journal of Failure Analysis and Prevention*, vol. 15, pp. 846–852, 2015.

[30] A. Arteiro, G. Catalanotti, J. Reinoso, P. Linde, and P. P. Camanho, "Simulation of the mechanical response of thin-ply composites: From computational micromechanics to structural analysis," *Archives of Computational Methods in Engineering*, vol. 26, pp. 1445–1487, 2019.

[31] A. J. C. Arteiro *et al.*, "Technology development and structural mechanics of composites built of spread tow thin-ply technology," 2012.

[32] C. T. Herakovich, "Mechanics of composites: A historical review," *Mechanics Research Communications*, vol. 41, pp. 1–20, 2012.

[33] A. Turon, J. Costa, P. Maimi, D. Trias, and J. Mayugo, "A progressive damage model for unidirectional fibre-reinforced composites based on fibre fragmentation. part i: Formulation," *Composites Science and Technology*, vol. 65, no. 13, pp. 2039–2048, 2005.

[34] S. T. Pinho, C. G. Dávila, P. P. Camanho, L. Iannucci, and P. Robinson, "Failure models and criteria for frp under in-plane or three-dimensional stress states including shear non-linearity," Tech. Rep., 2005.

[35] P. Camanho and S. Hallett, *Numerical modelling of failure in advanced composite materials*. Woodhead Publishing, 2015.

[36] C. G. Dávila, C. A. Rose, E. V. Iarve, and F. A. Leone, "Modeling fracture and complex crack networks in laminated composites," in *Mathematical methods and models in composites*, World Scientific, 2023, pp. 439–496.

[37] M. Hinton, A. Kaddour, and P. Soden, "Predicting failure in fibre composites: Lessons learned from the world-wide failure exercise," *TECHNICAL PAPERS-SOCIETY OF MANUFACTURING ENGINEERS-ALL SERIES-*, 2002.

[38] M. Hinton, A. Kaddour, and P. Soden, "The world-wide failure exercise: Its origin, concept and content," in *Failure criteria in fibre-reinforced-polymer composites*, Elsevier, 2004, pp. 2–28.

[39] A. C. Orifici, I. Herszberg, and R. S. Thomson, "Review of methodologies for composite material modelling incorporating failure," *Composite structures*, vol. 86, no. 1-3, pp. 194–210, 2008.

[40] Z. Hashin, "Fatigue failure criteria for unidirectional fiber composites," *Journal of applied mechanics*, vol. 47, no. 4, pp. 329–334, 1980.

[41] F.-K. Chang and K.-Y. Chang, "A progressive damage model for laminated composites containing stress concentrations," *Journal of composite materials*, vol. 21, no. 9, pp. 834–855, 1987.

[42] A. P. D.-I. Puck and H. Schürmann, "Failure analysis of frp laminates by means of physically based phenomenological models," *Composites Science and Technology*, vol. 58, pp. 1633–1662, 1998.

[43] L. Greszczuk, *Microbuckling of lamina-reinforced composites*. ASTM International, 1974.

[44] F.-K. Chang and L. B. Lessard, “Damage tolerance of laminated composites containing an open hole and subjected to compressive loadings: Part i—analysis,” *Journal of composite materials*, vol. 25, no. 1, pp. 2–43, 1991.

[45] C. Davila, N. Jaunky, and S. Goswami, “Failure criteria for frp laminates in plane stress,” in *44th AIAA/ASME/ASCE/AHS/ASC structures, structural dynamics, and materials conference*, 2003, p. 1991.

[46] P. Maimí, P. P. Camanho, J. Mayugo, and C. Dávila, “A continuum damage model for composite laminates: Part i–constitutive model,” *Mechanics of materials*, vol. 39, no. 10, pp. 897–908, 2007.

[47] J. D. Lee, “Three dimensional finite element analysis of damage accumulation in composite laminate,” *Computers & Structures*, vol. 15, no. 3, pp. 335–350, 1982.

[48] R. Christensen, “Stress based yield/failure criteria for fiber composites,” *International journal of solids and structures*, vol. 34, no. 5, pp. 529–543, 1997.

[49] H. Huang, G. S. Springer, and R. M. Christensen, “Predicting failure in composite laminates using dissipated energy,” *Journal of composite materials*, vol. 37, no. 23, pp. 2073–2099, 2003.

[50] Z. Hashin and A. Rotem, “A fatigue failure criterion for fiber reinforced materials,” *Journal of composite materials*, vol. 7, no. 4, pp. 448–464, 1973.

[51] R. Cuntze and A. Freund, “The predictive capability of failure mode concept-based strength criteria for multidirectional laminates,” *Composites Science and Technology*, vol. 64, no. 3-4, pp. 343–377, 2004.

[52] J. Gosse and S. Christensen, “Strain invariant failure criteria for polymers in composite materials,” in *19th AIAA Applied Aerodynamics Conference*, 2001, p. 1184.

[53] M. Wisnom, “The role of delamination in failure of fibre-reinforced composites,” *Philosophical Transactions of the Royal Society A: Mathematical, Physical and Engineering Sciences*, vol. 370, no. 1965, pp. 1850–1870, 2012.

[54] I. Raju and T. O’brien, “Fracture mechanics concepts, stress fields, strain energy release rates, delamination initiation and growth criteria,” in *Delamination behaviour of composites*, Elsevier, 2008, pp. 3–27.

[55] G. R. Irwin, “Analysis of stresses and strains near the end of a crack traversing a plate,” 1957.

[56] N. Amsc and A. A. CMPS, “Composite materials handbook,” *Polymer matrix composites materials usage, design, and analysis*, 2002.

[57] E. M. Wu and R. Reuter Jr, “Crack extension in fiberglass reinforced plastics,” *T and M report, University of Illinois*, vol. 275, p. 0, 1965.

[58] M. Benzeggagh and M. Kenane, “Measurement of mixed-mode delamination fracture toughness of unidirectional glass/epoxy composites with mixed-mode bending apparatus,” *Composites science and technology*, vol. 56, no. 4, pp. 439–449, 1996.

[59] J. R. Reeder, “3-d mixed mode delamination fracture criteria-an experimentalist’s perspective,” in *American Society for composites 21st annual technical conference*, 2006.

[60] L. Tong, “An assessment of failure criteria to predict the strength of adhesively bonded composite double lap joints,” *Journal of Reinforced Plastics and Composites*, vol. 16, no. 8, pp. 698–713, 1997.

[61] J. D. Whitcomb, *Analysis of instability-related growth of a through-width delamination.* National Aeronautics and Space Administration, Langley Research Center, 1984, vol. 86301.

[62] X. Q. Van, S. Y. Du, and W. Duo, “An engineering method of determining the delamination fracture toughness of composite laminates,” *Engineering fracture mechanics*, vol. 39, no. 4, pp. 623–627, 1991.

[63] J. R. Reeder, “A bilinear failure criterion for mixed-mode delamination,” *ASTM special technical publication*, vol. 1206, pp. 303–303, 1993.

[64] P. P. Camanho and C. G. Dávila, “Mixed-mode decohesion finite elements for the simulation of delamination in composite materials,” Tech. Rep., 2002.

[65] C. G. Dávila and E. R. Johnson, “Analysis of delamination initiation in postbuckled dropped-ply laminates,” *AIAA journal*, vol. 31, no. 4, pp. 721–727, 1993.

[66] P. Camanho and F. Matthews, “Delamination onset prediction in mechanically fastened joints in composite laminates,” *Journal of Composite Materials*, vol. 33, no. 10, pp. 906–927, 1999.

[67] E. F. Rybicki and M. F. Kanninen, “A finite element calculation of stress intensity factors by a modified crack closure integral,” *Engineering fracture mechanics*, vol. 9, no. 4, pp. 931–938, 1977.

[68] S. Rinderknecht and B. Kröplin, “A computational method for the analysis of delamination growth in composite plates,” *Computers & Structures*, vol. 64, no. 1-4, pp. 359–374, 1997.

[69] D. S. Dugdale, “Yielding of steel sheets containing slits,” *Journal of the Mechanics and Physics of Solids*, vol. 8, no. 2, pp. 100–104, 1960.

[70] G. I. Barenblatt, “The mathematical theory of equilibrium cracks in brittle fracture,” *Advances in applied mechanics*, vol. 7, pp. 55–129, 1962.

[71] P. P. Camanho, *Numerical simulation of delamination growth in composite materials.* NASA Langley Research Center, 2001.

[72] M. Akterskaia, E. Jansen, S. R. Hallett, P. Weaver, and R. Rolfes, “Analysis of skin-stringer debonding in composite panels through a two-way global-local method,” *Composite Structures*, vol. 202, pp. 1280–1294, 2018.

[73] A. Brandt, “Multi-level adaptive solution technique (mlat) for fast numerical solution to boundary value problems,” *Lecture Notes in Physics*, vol. 18, p. 82,

[74] I. Parsons and J. Hall, “The multigrid method in solid mechanics: Part i—algorithm description and behaviour,” *International Journal for Numerical Methods in Engineering*, vol. 29, no. 4, pp. 719–737, 1990.

[75] L. Gendre, O. Allix, P. Gosselet, and F. Comte, “Non-intrusive and exact global/local techniques for structural problems with local plasticity,” *Computational Mechanics*, vol. 44, pp. 233–245, 2009.

[76] Y. Liu, Q. Sun, and X. Fan, “A non-intrusive global/local algorithm with non-matching interface: Derivation and numerical validation,” *Computer Methods in Applied Mechanics and Engineering*, vol. 277, pp. 81–103, 2014.

[77] S. Hühne, J. Reinoso, E. Jansen, and R. Rolfes, “A two-way loose coupling procedure for investigating the buckling and damage behaviour of stiffened composite panels,” *Composite Structures*, vol. 136, pp. 513–525, 2016.

[78] *ABAQUS/Standard User’s Manual*, English. United States: Dassault Systèmes Simulia Corp, 2022.

[79] R. Krueger and T. K. O’Brien, “A shell/3d modeling technique for the analysis of delaminated composite laminates,” *Composites Part A: applied science and manufacturing*, vol. 32, no. 1, pp. 25–44, 2001.

[80] E. Pietropaoli and A. Riccio, “A global/local finite element approach for predicting interlaminar and intralaminar damage evolution in composite stiffened panels under compressive load,” *Applied Composite Materials*, vol. 18, pp. 113–125, 2011.

[81] R. K. Kapania, S. G. Haryadi, and R. T. Haftka, “Global/local analysis of composite plates with cutouts,” *Computational Mechanics*, vol. 19, no. 5, pp. 386–396, 1997.

[82] S. G. Haryadi, R. K. Kapania, and R. T. Haftka, “Global/local analysis of stepped plates with cutouts,” in *Computational Mechanics’ 95: Theory and Applications*, Springer, 1995, pp. 1638–1643.

[83] J. B. Chang, V. K. Goyal, J. C. Klug, and J. I. Rome, “Composite structures damage tolerance analysis methodologies,” Tech. Rep., 2012.

[84] A. Soto Masip *et al.*, “Development of efficient numerical models for the simulation of low velocity impact and compression after impact on composite structures,” 2018.

[85] S. Abdel-Monsef, B. Tijs, J. Renart, and A. Turon, “Accurate simulation of delamination under mixed-mode loading using a multilinear cohesive law,” *Engineering Fracture Mechanics*, vol. 284, p. 109 233, 2023.

[86] C. Sarrado, A. Turon, J. Costa, and J. Renart, “An experimental analysis of the fracture behavior of composite bonded joints in terms of cohesive laws,” *Composites Part A: Applied Science and Manufacturing*, vol. 90, pp. 234–242, 2016.

[87] S. A. Monsef, A. Ortega, A. Turon, P. Maimí, and J. Renart, “An efficient method to extract a mode i cohesive law for bonded joints using the double cantilever beam test,” *Composites Part B: Engineering*, vol. 178, p. 107 424, 2019.

[88] S. A. Monsef, M. Pérez-Galmés, J. Renart, A. Turon, and P. Maimí, “The influence of mode ii test configuration on the cohesive law of bonded joints,” *Composite Structures*, vol. 234, p. 111 689, 2020.

[89] A. Airoldi and C. G. Dávila, “Identification of material parameters for modelling delamination in the presence of fibre bridging,” *Composite Structures*, vol. 94, no. 11, pp. 3240–3249, 2012.

[90] C. G. Dávila, C. A. Rose, and P. P. Camanho, “A procedure for superposing linear cohesive laws to represent multiple damage mechanisms in the fracture of composites,” *International Journal of Fracture*, vol. 158, pp. 211–223, 2009.

[91] B. Green, M. Wisnom, and S. Hallett, “An experimental investigation into the tensile strength scaling of notched composites,” *Composites Part A: Applied Science and Manufacturing*, vol. 38, no. 3, pp. 867–878, 2007.

[92] Z. Su, T. Tay, M. Ridha, and B. Chen, “Progressive damage modeling of open-hole composite laminates under compression,” *Composite Structures*, vol. 122, pp. 507–517, 2015.

[93] M. Laffan, S. Pinho, P. Robinson, L. Iannucci, and A. McMillan, “Measurement of the fracture toughness associated with the longitudinal fibre compressive failure mode of laminated composites,” *Composites Part A: Applied Science and Manufacturing*, vol. 43, no. 11, pp. 1930–1938, 2012.

[94] S. Hallett, B. G. Green, W. Jiang, and M. Wisnom, “An experimental and numerical investigation into the damage mechanisms in notched composites,” *Composites Part A: Applied Science and Manufacturing*, vol. 40, no. 5, pp. 613–624, 2009.

[95] A. Turon, P. P. Camanho, J. Costa, and C. Dávila, “A damage model for the simulation of delamination in advanced composites under variable-mode loading,” *Mechanics of materials*, vol. 38, no. 11, pp. 1072–1089, 2006.

[96] E. González, P. Maimí, A. Turon, P. Camanho, and J. Renart, “Simulation of delamination by means of cohesive elements using an explicit finite element code,” *Computers, Materials & Continua (CMC)*, vol. 9, no. 1, p. 51, 2009.

[97] J. Mazars, “Mechanical damage and fracture of concrete structures,” *Advances in fracture research*, vol. 4, pp. 1499–1506, 1981.

[98] J. C. Simo and J. Ju, “Strain-and stress-based continuum damage models—i. formulation,” *International journal of solids and structures*, vol. 23, no. 7, pp. 821–840, 1987.

[99] W.-G. Jiang, S. R. Hallett, B. G. Green, and M. R. Wisnom, “A concise interface constitutive law for analysis of delamination and splitting in composite materials and its application to scaled notched tensile specimens,” *International journal for numerical methods in engineering*, vol. 69, no. 9, pp. 1982–1995, 2007.

[100] C. Furtado, G. Catalanotti, A. Arteiro, P. Gray, B. Wardle, and P. Camanho, “Simulation of failure in laminated polymer composites: Building-block validation,” *Composite Structures*, vol. 226, p. 111 168, 2019.

[101] L. Hart-Smith, “New, and very different, linear strain-displacement relation for the in-plane shear strain in thin cylindrical shells,” in *13TH INTERNATIONAL CONFERENCE ON THE MECHANICAL BEHAVIOUR OF MATERIALS*, 2019, p. 543.

Appendix A

Wing-Box Global Model Results

A.1 Displacement Field, U

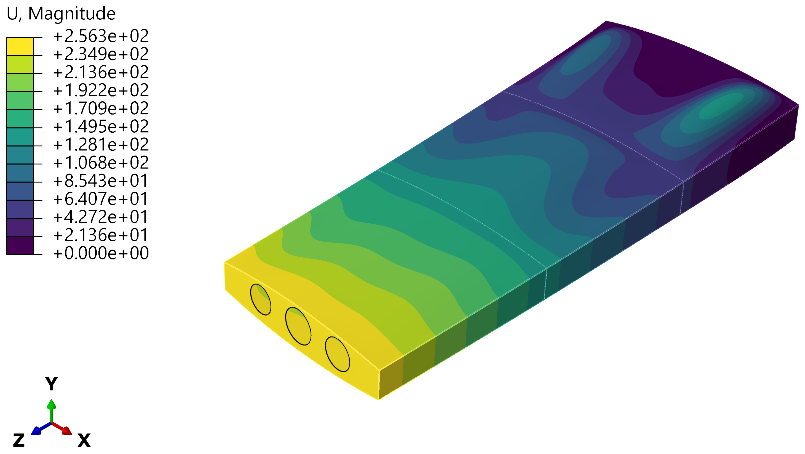
U, Magnitude
+2.563e+02
+2.349e+02
+2.136e+02
+1.922e+02
+1.709e+02
+1.495e+02
+1.281e+02
+1.068e+02
+8.543e+01
+6.407e+01
+4.272e+01
+2.136e+01
+0.000e+00
Y
Z
X

(a) Top view

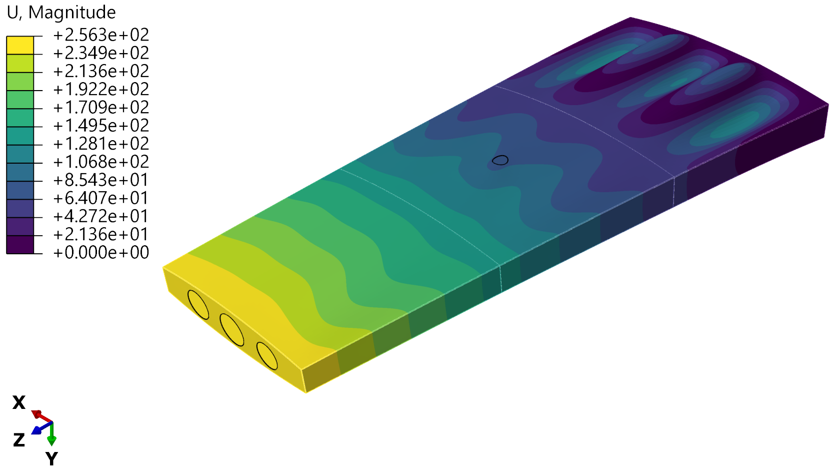
U, Magnitude
+2.563e+02
+2.349e+02
+2.136e+02
+1.922e+02
+1.709e+02
+1.495e+02
+1.281e+02
+1.068e+02
+8.543e+01
+6.407e+01
+4.272e+01
+2.136e+01
+0.000e+00
X
Z
Y

(b) Bottom view

Figure A.1: Wing-box displacement magnitude in [mm], scale factor of 1.

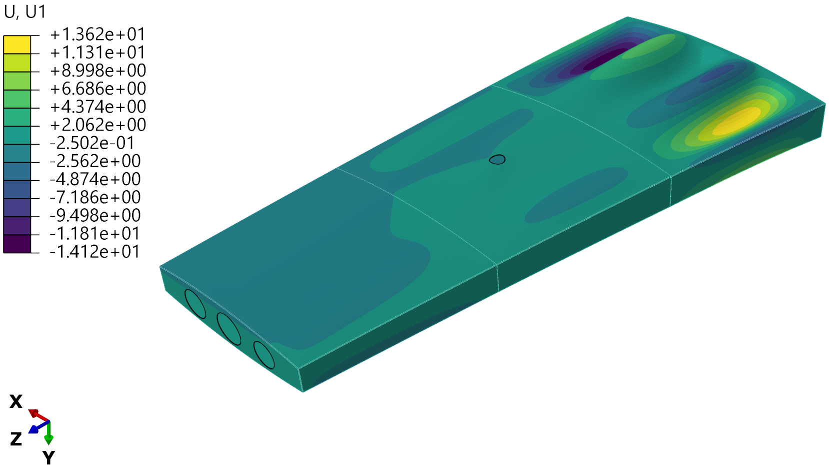
U, U1
+1.362e+01
+1.131e+01
+8.998e+00
+6.686e+00
+4.374e+00
+2.062e+00
-2.502e-01
-2.562e+00
-4.874e+00
-7.186e+00
-9.498e+00
-1.181e+01
-1.412e+01
X
Z
Y

(a) Top view

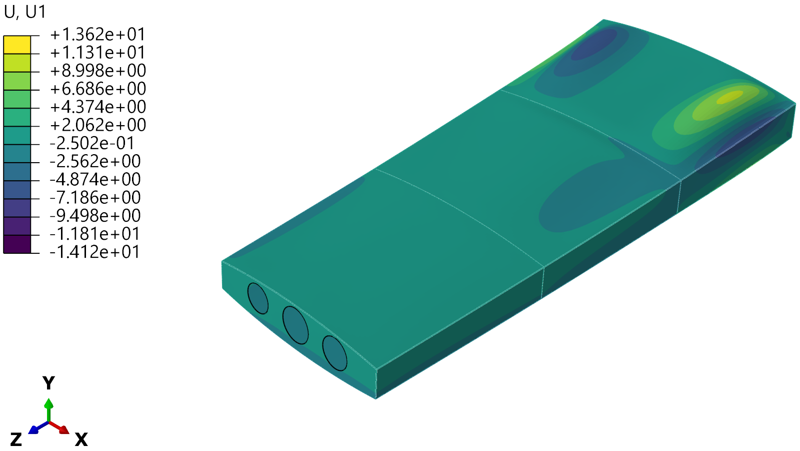
U, U1
+1.362e+01
+1.131e+01
+8.998e+00
+6.686e+00
+4.374e+00
+2.062e+00
-2.502e-01
-2.562e+00
-4.874e+00
-7.186e+00
-9.498e+00
-1.181e+01
-1.412e+01
Y
Z
X

(b) Bottom view

Figure A.2: Wing-box displacement in the x direction in [mm], scale factor of 1.

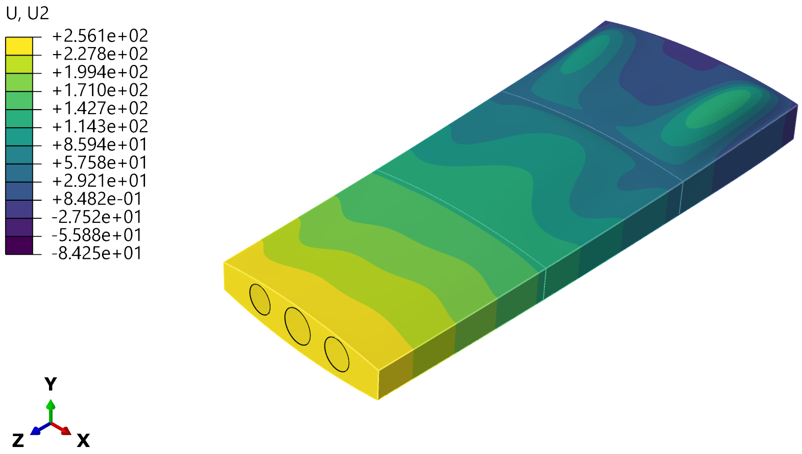

(a) Top view

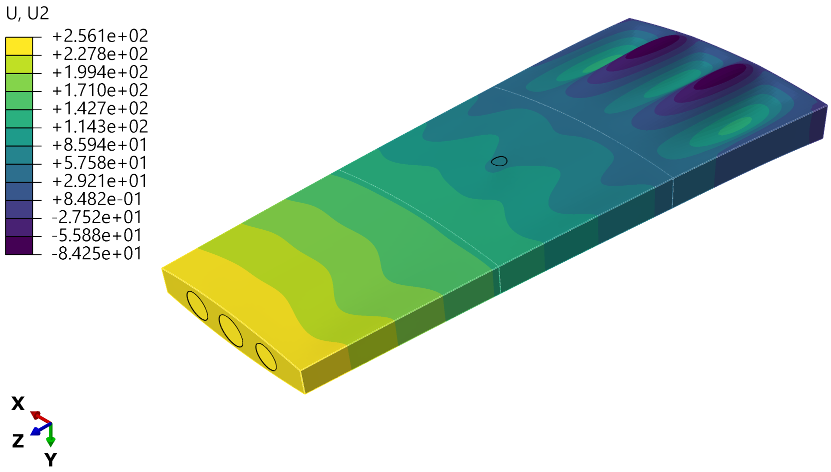

(b) Bottom view

Figure A.3: Wing-box displacement in the y direction in [mm], scale factor of 1.

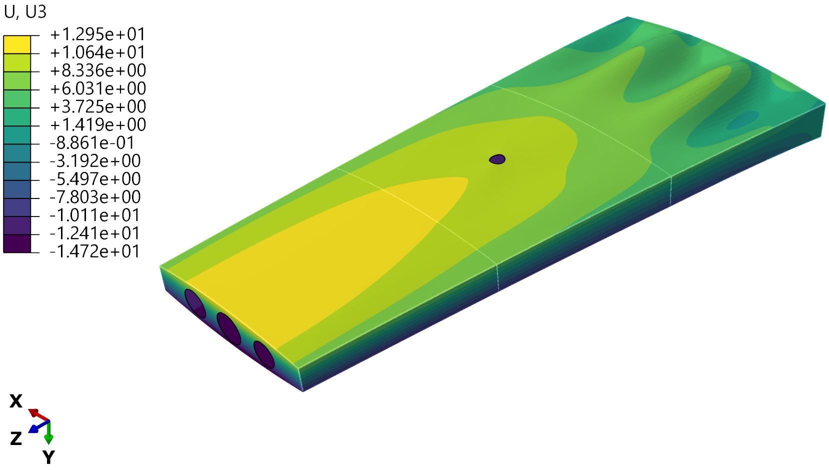
U, U3
+1.295e+01
+1.064e+01
+8.336e+00
+6.031e+00
+3.725e+00
+1.419e+00
-8.861e-01
-3.192e+00
-5.497e+00
-7.803e+00
-1.011e+01
-1.241e+01
-1.472e+01
X
Z
Y

(a) Top view

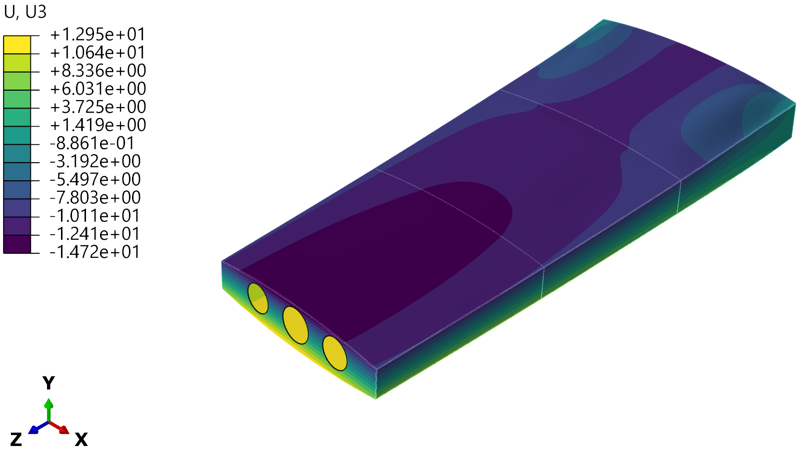
U, U3
+1.295e+01
+1.064e+01
+8.336e+00
+6.031e+00
+3.725e+00
+1.419e+00
-8.861e-01
-3.192e+00
-5.497e+00
-7.803e+00
-1.011e+01
-1.241e+01
-1.472e+01
Y
Z
X

(b) Bottom view

Figure A.4: Wing-box displacement in the z direction in [mm], scale factor of 1.